

# Environmental processing of galaxies in H I-rich groups

Robert Džudžar,<sup>1\*</sup> Virginia Kilborn,<sup>1,2</sup> Sarah M. Sweet,<sup>1,2,3</sup> Gerhard Meurer,<sup>4</sup>

T.H. Jarrett,<sup>5</sup> Dane Kleiner<sup>6</sup>

<sup>1</sup>Centre for Astrophysics and Supercomputing, Swinburne University of Technology, P.O. Box 218, Hawthorn, VIC 3122, Australia

<sup>2</sup>ARC Centre of Excellence for All Sky Astrophysics in 3 Dimensions (ASTRO 3D)

<sup>3</sup>School of Mathematics and Physics, University of Queensland, Brisbane, QLD 4072, Australia

<sup>4</sup>International Centre for Radio Astronomy Research, ICRAR M468, 35 Stirling Highway, Crawley, WA 6009, Australia

<sup>5</sup>Department of Astronomy, University of Cape Town, Rondebosch, South Africa

<sup>6</sup>INAF - Osservatorio Astronomico di Cagliari, Via della Scienza 5, I-09047 Selargius (CA), Italy

Accepted XXX. Received YYY; in original form ZZZ

## ABSTRACT

We present and explore the resolved atomic hydrogen (H I) content of 13 H I-rich and late-type dominated groups denoted ‘Choirs’. We quantify the H I content of the Choir galaxies with respect to the median of the H I-mass fraction ( $f_{\text{H I}}$ ) of their grandparent HIPASS sample. We find that the H I mass fraction of the Choir galaxies is dispersed around the HIPASS median in the range  $-1.4 \leq \Delta f_{\text{H I}} [\text{dex}] \leq 0.7$ , from H I-excess to H I-deficient galaxy regime. The H I-excess/H I-deficient galaxies contain more/less than 2.5 times their expected H I content with respect to the HIPASS median. We show and discuss that the environmental processing in Choirs occurs via tidal stripping and galaxy mergers. Our analysis suggests that tidal stripping contributes to the loss of the H I, while galaxy mergers contribute to the enhancement of the H I. Exploring the mid-infrared properties of Choir galaxies we find possible environmental processing in only nine Choir galaxies, which indicates that environmental processing is more perceptible in the H I content than the mid-infrared properties. Moreover, we find that environmental processing occurs in Choir groups regardless of their global environment, whether they are in isolation or in proximity to the denser structures, such as cosmic web filaments. We explore possible scenarios of the Choirs evolution, taking into account their H I content, velocity dispersion, crossing time and their global environment. We conclude that the most likely evolution for the majority of Choir groups is that they will become more compact as their members undergo multiple H I-rich mergers.

**Key words:** galaxies: general – galaxies: evolution – galaxies: groups – galaxies: ISM

## 1 INTRODUCTION

In the local Universe 50–60 percent of galaxies reside in groups (Yang et al. 2007; Freeland et al. 2009; Tempel et al. 2014) however, environment is not a simple categorical property, it is rather a continuous one.

Galaxy groups that have been studied in the literature have been classified as loose groups (van Driel et al. 2001; Pisano et al. 2007; Kilborn et al. 2009; Oosterloo et al. 2018), poor groups (Zabludoff & Mulchaey 1998; Tovmassian & Plionis 2009), compact groups (Hickson 1997; Coziol et al. 2000; Verdes-Montenegro et al. 2001), rich groups (Wojtak 2013), small groups (Barnes & Webster 2001), supergroups (Brough et al. 2006; Wolfinger et al. 2016), dwarf groups (Stierwalt et al. 2017) and fossil groups (Ponman et al. 1994; Jones et al. 2003). The common property of these groups

is that galaxies have relatively low velocity dispersion and thus tidal interactions and mergers are often observed (e.g. Yun et al. 1994; Rots et al. 1990; Sengupta et al. 2017). Therefore, groups are a suitable environment for galaxy environmental processing in the form of: (i) disturbing galaxy’s stellar content and morphology, (ii) exchanging gas content between galaxies (removing or accreting), which can lead to change of galaxy’s star formation properties.

### 1.1 H I gas

Hydrogen in its atomic form (H I) is the raw material for condensing into molecular Hydrogen (H<sub>2</sub>), the fuel for future star formation, thus it is an essential part of galaxies (Bigiel & Blitz 2012; Catinella et al. 2018). The H I content in galaxies is often analysed using various scaling relations utilizing galaxy properties such as stellar mass, color, mor-

\* E-mail: rdzudzar@swin.edu.au; robertdzudzar@gmail.com

phology, star formation rate, as well as tracing galaxy environment (Haynes & Giovanelli 1984; Giovanelli & Haynes 1985; Dénes et al. 2014; Catinella et al. 2018). Large surveys such as The H I Parkes All Sky Survey (HIPASS, Barnes et al. 2001) and the Arecibo Legacy Fast ALFA Survey (ALFALFA, Giovanelli et al. 2005) detected H I in more than 5000 and 30000 galaxies respectively, and have significantly improved these scaling relations.

Mapping the H I gas within and around the galaxies can show its distribution, be used to determine galaxy kinematics, and to study galaxy interactions. The H I features that reveal galaxy interactions, and are often found in galaxy groups, are in the form of tidal tails (Scott et al. 2012), bridges (Jones et al. 2019), rings (Malphrus et al. 1997) and clouds (Ryder et al. 2001), and more of such systems are described in the brief overview by Koribalski (2020). The abundance of such H I features points towards a complex history of galaxy evolution in the group environment.

## 1.2 H I in groups

It is known that in galaxy clusters, the most densest of environments, a galaxy’s evolution is influenced by its environment. Thus, we observe an increased fraction of early-type galaxies (Dressler 1980), decreased star formation rates (Lewis et al. 2002) and decreased gas content of galaxies (Haynes & Giovanelli 1984) in high density environments. On the other hand, the evolution of galaxies in the field is thought to be free from environmental effects. Naturally, galaxy groups are in between these extreme environments.

It has been shown that spiral galaxies are more H I deficient in higher density environments, for instance, near the galaxy cluster centre or in groups, than spiral galaxies in the field (Giovanelli & Haynes 1985; Chung et al. 2009; Solanes et al. 2001; Verdes-Montenegro et al. 2001; Kilborn et al. 2009; Dénes et al. 2014, 2016). The difference in H I content across different environments suggests that the higher density environment contributes to the exhaustion of the H I gas. The depletion of the H I content within clusters is most often connected to ram-pressure stripping (Gunn & Gott 1972; Chung et al. 2009; Cortese et al. 2011; Brown et al. 2017; Stevens & Brown 2017). On the other hand, the depletion of the H I content in groups is debated between ram-pressure stripping (Brown et al. 2017), tidal interactions (Yun et al. 1994), starvation (Larson et al. 1980) and viscous stripping (Nulsen 1982).

The most well-studied type of groups are Hickson Compact Groups (HCG), which are dense galaxy configurations that contain four to 10 galaxies with a projected distance between them on the order of a galaxy size (and smaller) and velocity dispersion of  $\sim 200 \text{ km s}^{-1}$  (Hickson 1997; Williams et al. 1990; Verdes-Montenegro et al. 2001; Borthakur et al. 2015; Coziol & Plauchu-Frayn 2007). From observations of the H I content in Hickson Compact Groups (Hickson 1982; Verdes-Montenegro et al. 2001; Borthakur et al. 2015) it has been found that gas removal is evident as the galaxies are often depleted of their H I content. Verdes-Montenegro et al. (2001) explains the evolutionary path of galaxy groups through a gradual removal of the H I gas from the galaxies. In contrast to HCGs, loose groups are sparse and have a typical galaxy separation of few hundred kpc (Sengupta & Balasubramanyam 2006; Pisano et al. 2011). Kilborn et al. (2009)

found that the H I deficient galaxies within loose groups tend to lie within the 1 Mpc in projected distance from the group centre. Utilizing over 740 galaxy groups from the ALFALFA survey, Hess & Wilcots (2013) found that the fraction of H I-rich galaxies decreases in the central regions of groups as the group optical membership increases. They also found that H I gas depletion starts first in the lowest H I mass galaxies.

It is common to make a distinction between the central galaxy which is most often the brightest (most massive) galaxy within a group (or a cluster) and satellite galaxies, being all other galaxies within the same group (e.g. White & Rees 1978; Skibba et al. 2011; Lacerna et al. 2014). The difference between the central galaxy and satellites is that the central galaxy is theoretically at rest with respect to its halo, while satellite galaxies are moving in the gravitational potential of a halo and can experience environmental effects (White & Rees 1978; Yang et al. 2007; Brown et al. 2017). Džudžar et al. (2019a) gives the example of a group with two centrals, both at rest within the halo. Recent studies of the H I content of central and satellite galaxies have shown significance of the group mass regime. Janowiecki et al. (2017) have shown that central galaxies within small groups are  $\sim 0.3$  dex more H I-rich than the central galaxies in isolation. Brown et al. (2017), utilizing the stacking technique, found that satellite galaxies in high mass haloes have a lower H I mass fraction with respect to those in low mass haloes.

An increasing number of observations of the H I gas content show evidence and importance of galaxy environmental processing in groups (Verdes-Montenegro et al. 2001; Kilborn et al. 2005; Pisano et al. 2011; Hess & Wilcots 2013; Catinella et al. 2013; Brown et al. 2017; Džudžar et al. 2019b). How much environmental processing is important, and to what extent it has progressed in the H I-rich and late-type dominated groups is still an open question.

## 1.3 From SINGG to Choirs

The Survey of Ionization in Neutral Gas Galaxies (SINGG) imaged a sample of 468 H I detections from the HIPASS survey in the R-band and H $\alpha$  narrow-band (Meurer et al. 2006). Inspecting SINGG fields<sup>1</sup> Sweet et al. (2013) discovered 15 fields that have 4+ emission line galaxies within the 15’ beam of the Parkes H I detections, catalogued them and denoted them ‘Choirs’. Such selection overcomes optical-selection biases, however it introduces selection effects on the distance and H I mass. Due to the field-of-view of the SINGG fields, selection of the Choir groups is prone towards H I-rich systems at distance  $\geq 30$  Mpc (Sweet et al. 2013).

Galaxies in the Choir groups have similar properties as the single galaxies in SINGG based on their R-band radius, R-band surface brightness, H $\alpha$  equivalent width and specific star formation rate (Sweet et al. 2013). The mean group projected size is around two times larger than that of Hickson Compact Groups and around 10 times smaller than Garcia (1993) groups. Based on the total group H I content, Sweet et al. (2013) found that Choir groups are in an early stage of a group assembly: they have an average star formation efficiency, and they are not significantly H I-deficient.

<sup>1</sup> Field-of-view  $\sim 15'$

Sweet et al. (2014) probed the gas-phase metallicity relation of galaxies within H I-rich Choir groups. They found two sub-populations of galaxies: metal-poor dwarfs and metal-rich giants in the metallicity-luminosity plane. Sweet et al. (2014) also found that the metallicity of the dwarf galaxies depends on the group membership and group H I gas content: i) dwarf galaxies in Choir groups have lower metallicity than those in isolation; ii) at low luminosity, metallicity has a higher dispersion which indicates difference in H I content and environment.

Choir groups were also used to find a population of galaxies that are formed from the tidal tail material of the interacting galaxies - tidal dwarf galaxies. Sweet et al. (2014) found three strong tidal dwarf galaxy candidates: J0205-55:S7, J0400-52:S8 and J0400-52:S9. Moreover, Sweet et al. (2016) observed 22 star-forming dwarf galaxies in four Choir groups with DEIMOS multi-object spectroscopy and analysed the galaxy kinematics, finding two new tidal dwarf galaxy candidates: J1051-17:g11 and J1403-06:g1. The rotation curves of the observed dwarf galaxies are disturbed due to recent interactions (Sweet et al. 2016). Moreover, they found that as much as half of the sample may be affected by the tidal interactions with neighbouring galaxies.

In Džudžar et al. (2019a) we analysed the integrated H I properties of 27 galaxies within nine Choir groups and compared them to a sample of isolated galaxies. We explored the H I mass fraction, specific star formation rate, star formation efficiency, H I deficiency, H I mass-size relation and stability parameter of the group galaxies with respect to the isolated galaxies. We found that the majority of central galaxies are within  $2\sigma$  scatter of the isolated galaxies, comparing H I mass fraction, the specific star formation and star formation efficiency. Satellite galaxies were shown to have lower H I mass fractions which is a possible indication that these galaxies experienced tidal stripping (Džudžar et al. 2019a). Furthermore, we determined that seven gas-rich Choir galaxies lie on the  $f_{\text{atm-q}}$  relation (Obreschkow et al. 2016) indicating that there are no strong environmental influences on these galaxies.

The motivation for this paper is to analyse the environmental processing in the H I-rich Choir groups, using the resolved H I content of member galaxies. For each group from our sample, we present the H I column density maps, kinematic maps and the global environment for each group. We present the sample in the context of the parent SINGG and grandparent HIPASS sample, and several galaxy samples from the literature. We discuss the properties of the H I in galaxies and in the tidal streams.

This paper is organised as follows: Section 2 describes our sample of Choir groups and their H I mapping, and auxiliary data used in this work. Section 3 presents our main results in this work: Choir galaxies and their H I-mass fraction in context, the H I distribution in Choir galaxies - highlighting H I-deficient and H I-excess galaxies. This section also presents the mid-infrared properties of Choir galaxies, as well as the Choir groups in context of Hickson compact groups and their evolution. Section 4 presents the global environment around Choir groups. Section 5 discusses our results and summarises our conclusions. Appendix B describes the Choir group properties, Appendix H describes our Choir groups individually. We present H I intensity maps, H I kinematics, H I spectra and

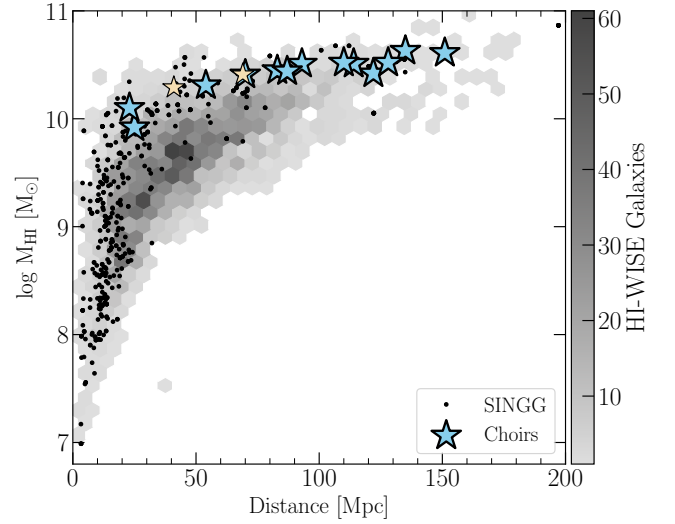


**Figure 1.** The H I mass versus distance. The stars show Choir groups, the blue stars are those that we have resolved H I data, and the yellow stars are those for which we do not have resolved H I data. The black points show galaxies from the parent SINGG sample. The hexbins in the background show the distribution of the parent HIPASS sample using the galaxies from the HI-WISE catalogue of Parkash et al. (2018).

global group environment for each Choir group in Appendix I.

Throughout this paper the adopted cosmology is  $H_0 = 70 \text{ km s}^{-1} \text{ Mpc}^{-1}$ ,  $\Omega_\Lambda = 0.7$  and  $\Omega_m = 0.3$ . Mid-infrared star-formation follows the Cluver et al. (2017) prescription. The WISE photometric calibration is described in Jarrett et al. (2011). Presented H I maps and spectra use velocities in the optical convention. The group distances are based on the multipole attractor model (Mould et al. 2000), as in (Meurer et al. 2006; Sweet et al. 2013 and Džudžar et al. 2019a).

## 2 SAMPLE AND DATA

We present H I content in a total of 13 Choir groups, we have mapped 11 Choir groups and we use previously published data for three Choir groups. Eight Choir groups were observed with the Australia Compact Telescope Array (ATCA, project C2440) using the CFB 64M-32k (34 kHz resolution) and CFB 1M-0.5k (0.5 kHz resolution) correlator configuration on the Compact Array Broadband Backend (CABB; Wilson et al. 2011). These groups are: HIPASS J0205-55, HIPASS J0258-74, HIPASS J0400-52, HIPASS J1051-17, HIPASS J1159-19, HIPASS J1250-20, HIPASS J1956-50 and HIPASS J2027-51. Whereas, three Choir groups were observed with the Karl G. Jansky Very Large Array (VLA, project 13A-207) in the hybrid DnC configuration, with a total bandwidth of 4 MHz (1024 channels of 3.906 kHz width). These groups are: HIPASS J1026-19, HIPASS J1059-09 and HIPASS J1408-21.

In addition to our observations (see Džudžar et al. (2019a), Table 1 and Table D1), we use previously published data for three Choir groups: HIPASS J0209-10 (Jones et al. 2019), HIPASS J1159-19 (Phookun et al. 1992) and HIPASS J2318-42a (Dahlem 2005) (see Table C1). We were unable to find H I data in the literature for two Choir groups: HIPASS J0443-

05 and HIPASS J1403-06. We show the Choir galaxy group sample on the total H I mass versus distance in Figure 1. Henceforth, we omit the HIPASS prefix for brevity.

## 2.1 H I data reduction

We processed the H I data on the Green II and OzSTAR Swinburne supercomputers. ATCA and VLA data were reduced with the standard procedures in MIRIAD - Multichannel Image Reconstruction, Image Analysis and Display (Sault et al. 1995) and CASA - Common Astronomy Software Applications (McMullin et al. 2007) software packages, and we summarise the procedures below. In Džudžar et al. (2019a) we presented the integrated properties obtained from our H I mapping. In this work we present the full maps of Choir groups including both: moment 0 - the H I total intensity maps; and moment 1 - the velocity field maps.

The ATCA data reduction was carried out as follows. Data were loaded with the task ATL0D. Raw data were flagged for radio interference using the tasks UVFLAG, BLFLAG and PGFLAG. After the flagging we performed bandpass, flux and phase calibrations using the following tasks: MFCAL, GPCAL, GPBOOT and MFBOOT. For bandpass and flux calibration we used the standard calibration source PKS 1934-638, while phase calibrators are given in Table 1 as well as in Table 1 in Džudžar et al. (2019a). After calibrations we performed continuum subtraction with UVLIN by fitting it to the line-free channels. This procedure was performed on each of the array configurations and then all visibilities from the same source were combined using INVERT to form a dirty cube (excluding antenna 6), using Briggs' robust parameter of 0.5 and a channel width of 5 km s<sup>-1</sup>. The obtained dirty data cubes were then cleaned using the task CLEAN, restored using the task RESTOR. The primary beam correction was done with the task LINMOS. We determined the RMS in the data cube with the tasks IMSTAT and IMHIST.

We measured the galaxy H I properties using MBSPECT and obtained the moment 0 and moment 1 maps with the task MOMENT, applying a 3 $\sigma$  clipping. We used KVIS from the Karma library (Gooch 1996) for initial visualization, while exported moment maps were visualized using python. We present the H I-intensity maps, H I velocity fields and spectra in Appendix I.

The VLA data reduction was carried out as follows. Data were cleaned from radio interference using task FLAGDATA. Bandpass, flux and phase calibration was performed using the following tasks: SETJU, GAINCAL, BANDPASS, and FLUXSCALE. We then split the data using task SPLIT and performed continuum subtraction using line-free channels with the task UVCONTSUB. We produced the H I data cubes with the task CLEAN, using natural weighting (for J1026-19 and J1059-09) and Briggs' robust parameter of 0 (for J1408-21) and a channel width of 5 km s<sup>-1</sup>. With the task IMPBCOR we corrected for the primary beam, and we created moment maps with the task IMMOMENTS. We used VIEWER for initial visualization, while exported moment maps were visualized using python and presented in Appendix I.

## 2.2 Auxiliary data

We make use of imaging from the Wide-field Infrared Survey Explorer (*WISE*; Wright et al. 2010) to obtain integrated mid-infrared photometry in the four *WISE* bands: W1 (3.4 $\mu$ m), W2 (4.6 $\mu$ m), W3 (12 $\mu$ m) and W4 (22 $\mu$ m). Sources are measured using the same procedure as detailed in Jarrett et al. (2013, 2019), and the resulting photometry used to derive stellar masses, star formation rates and mid-infrared colour properties of the Choir galaxies (see Section 3.4 for details).

We make use of the optical observations of Choir groups which were carried out with the Dark Energy Camera (DECam) on the CTIO Blanco 4-m telescope in the *g*, *r*, *i* and *z* bands obtained for program AAT/13A/02 (PI S. Sweet). In addition, we use optical imaging from Dark Energy Survey Data Release 1 (*g*, *r* and *i*-band) for two Choir groups: HIPASS J0205-55 (partially covered by DES) and HIPASS J0400-52 (as used in Džudžar et al. 2019b). We also make use of the Digitized Sky Survey (DSS) imaging.

## 2.3 Comparison samples

To place our sample of Choir groups in the wider context, we compare it to several galaxy samples from the literature:

- HICAT catalogue (Meyer et al. 2004; Zwaan et al. 2004) from the H I All Sky Survey (HIPASS Barnes et al. 2001), which is the parent sample of the SINGG survey. We are using HICAT+*WISE* catalogue (HI-WISE,  $\sim$ 2300 galaxies) with the updated *WISE* photometry from Parkash et al. (2018).
- SINGG – Survey of Ionization in Neutral Gas Galaxies (Meurer et al. 2006) comprised of 468 galaxies, and it is a parent sample of Choir groups.
- AMIGA – Analysis of the Interstellar Medium of Isolated Galaxies (Verdes-Montenegro et al. 2005). Data of the AMIGA sample is obtained combining two catalogues: H I masses from Jones et al. (2018) and stellar masses from Fernández Lorenzo et al. (2013) for a total of 342 galaxies.
- xGASS – The extended GALEX Arecibo SDSS Survey (Catinella et al. 2018), a gas fraction limited survey of  $\sim$ 1200 galaxies.
- HCG – Hickson Compact Groups (Hickson 1982). We use data of 72 HCGs (Verdes-Montenegro et al. 2001) and their H I properties.
- H I-deficient galaxies from Dénes et al. (2014) and Murgeshan et al. (2019).
- H I-excess galaxies from Lutz et al. (2018).

## 3 RESULTS

In order to assess environmental processing of galaxies in H I-rich groups, we analyse the H I properties, star formation and environment of Choir galaxies. We show the H I mass fraction of the Choir galaxies and compare them to the several other galaxy samples from the literature. We explore the mid-infrared properties of Choir galaxies. And finally, we analyse the Choir galaxies discussing their anomalous H I content, specific star formation rate and tidal interactions.

We use standard relation to derive the H I mass:

$$M_{\text{HI}} = 2.365 \times 10^5 D^2 F_{\text{HI}}, \quad (1)$$

**Table 1.** Summary of the ATCA H I observations that are used in this paper in addition to those in Table 1. from [Džudžar et al. \(2019a\)](#).

Group ID (1)	1.5/750/EW [h] (2)	Phase Calibrator (3)	$f_c$ [MHz] (4)	$\theta_{\min} \times \theta_{\text{maj}}$ ["] (5)	rms [mJy beam <sup>-1</sup> ] (6)
J0205-55 <sup>a</sup>	.../7.82/7.6	PKS 0302-623	1393	56.7 × 108.5	1.13
J1956-50	6.57/8.16/7.48	PKS 2052-474	1385	40.5 × 86.1	1
J1159-19	.../2.35/4.14	PKS 1245-197	1413	70.1 × 193.3	2

Columns: (1) Group name (HIPASS+ID); (2) Time on the source for the particular ATCA array configuration; (3) Phase calibrator for the source; (4) Central frequency of band in MHz. (5) Minor and major axis of the synthesized beam size, respectively; (6) Root-mean-square of the data cube.

<sup>a</sup> In [Džudžar et al. \(2019a\)](#) we used pre-CABB data for J0205-55, while in this work we use our observations of this group.

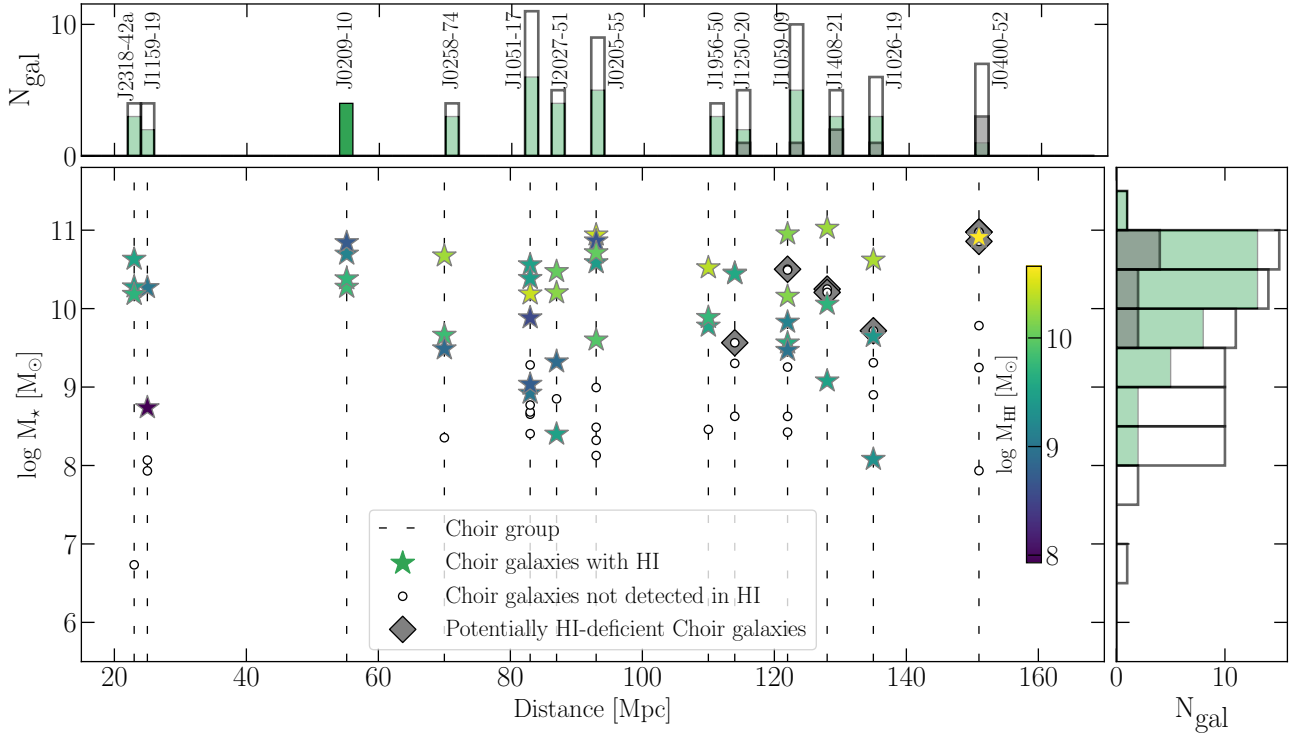


**Figure 2.** Stellar mass versus distance, and their histograms, for Choir galaxies. The coloured stars show Choir galaxies detected in H I, while the open circles show Choir galaxies without detected H I. The circles within the grey diamonds are potentially H I-deficient galaxies, as described in Appendix E. The green histograms show Choir galaxies with H I, the grey histograms show potentially H I-deficient galaxies and the white histograms show all Choir galaxies. The vertical dashed lines connect Choir galaxies within the same group, based on the adopted group distance - their names are shown in the upper histogram. The nearest three groups are those which H I data are obtained from the literature: J2318-42a ([Dahlem 2005](#)), J1159-19 ([Phookun et al. 1992](#)) and J0209-10 ([Jones et al. 2019](#)).

where  $F_{\text{HI}}$  is the integrated flux density in  $\text{Jy km s}^{-1}$ ,  $D$  is the distance to the galaxy in Mpc, and mass is obtained in  $M_{\odot}$ . The distances are adopted from [Sweet et al. \(2013\)](#). For the three Choir groups for which data are used from the literature, we re-derive their H I masses in order to be consistent with our distances and show results in Table C1. There is an excellent agreement between the literature and our derivation of the  $\log M_{\text{HI}}$  for J0209-10 ([Jones et al. 2019](#)) and J2318-42a ([Dahlem 2005](#)), with a mean difference of  $\sim 0.1$  dex, while galaxies within J1159-19 have a mean difference in  $\log M_{\text{HI}}$  of  $\sim 0.8$  dex. Such a large difference is due to the adapted distance: we use 25 Mpc (similar to the Hubble flow), while [Phookun et al. \(1992\)](#) used 10 Mpc.

### 3.1 H I detections vs H I non-detections

Within 13 Choir groups presented in this paper, [Sweet et al. \(2013\)](#) catalogued 80 galaxies. We have detected H I emission in 44 galaxies: nine of these are obtained from the literature and 35 with our observations, including seven new detections (hereafter, annotated with A) which are outside of the field of view in SINGG. Therefore, we obtained the H I emission in 50.6% of galaxies, and now we examine the H I non-detections.

In Figure 2 we show the stellar mass versus distance, for Choir galaxies. Choir galaxies detected in the H I are shown with the filled coloured stars (where colour denotes their H I mass), while open circles are Choirs not detected in H I. In the

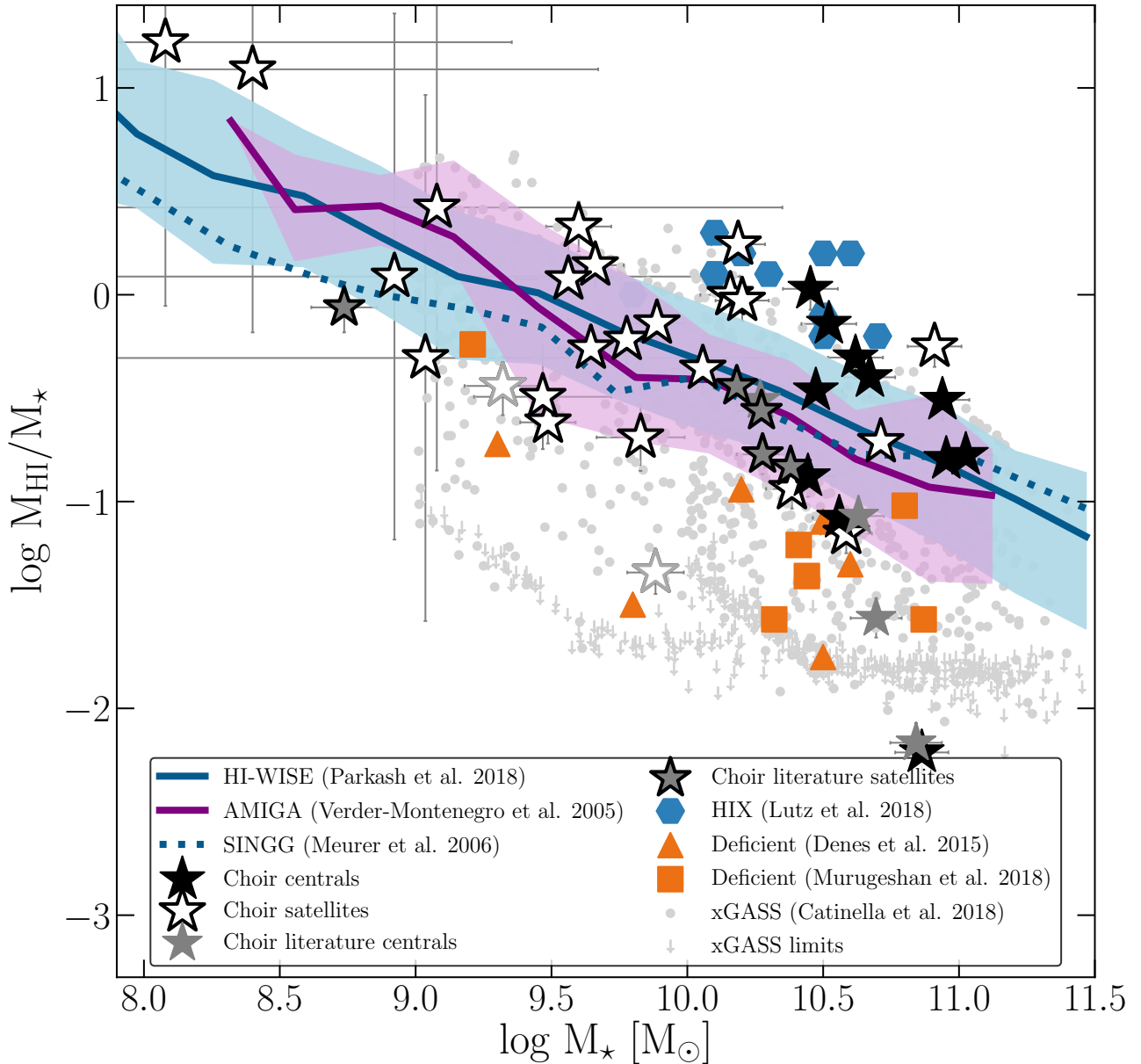


**Figure 3.** H I mass fraction versus stellar mass. Choirs galaxies are denoted as the star symbols, the solid black and white stars respectively correspond to central and satellite galaxies, as in [Džudžar et al. \(2019a\)](#). Two stars with the grey edge are Choir galaxies that are tentative detections, below  $3\sigma$ . The grey stars are Choir galaxies for which we found H I fluxes in the literature (J0209-10 group from [Jones et al. 2019](#), J1159-19 group from [Phookun et al. 1992](#), J2318-42a group from [Dahlem 2005](#)). The grey solid ones are centrals and the grey ones with black outlines are satellites. The orange triangles and rectangles are H I deficient galaxies, respectively from [Dénes et al. \(2016\)](#) and [Murugesan et al. \(2019\)](#). The blue hexagons are H I-excess galaxies from [Lutz et al. \(2018\)](#). The blue solid line is the running median of the HIPASS parent sample (using HI-WISE data obtained from [Parkash et al. 2018](#)) and the shaded region shows 16th and 84th percentile. The blue dotted line is the running median of the SINGG parent sample (SINGG sample is from [Meurer et al. \(2006\)](#), while the stellar masses are from [Parkash et al. 2018](#)). The purple solid line is the running median of isolated galaxies from the AMIGA sample [Verdes-Montenegro et al. \(2005\)](#), and the shaded region shows 16th and 84th percentile. The grey points and arrows in the background are galaxies and upper limits from the xGASS sample ([Catinella et al. 2018](#)).

mass regime  $M_* \leq 10^9 M_\odot$ , we detect four out of 23 galaxies in H I emission. This is not surprising as the majority of these non-detections are small compact dwarf galaxies. In [Figure 2](#) we also show that we have H I non-detections in the stellar mass range  $10^9$ – $10^{11} M_\odot$ , well within the range of the H I detected galaxies. These galaxies have a sufficiently high stellar mass, and angular size, to be above our H I detec-

tion threshold if they have normal amounts of H I, indicating that they are H I-deficient galaxies - they have on average eight times less H I than the average galaxy of the similar stellar mass (they are marked with the grey diamonds in [Figure 2](#), and see [Appendix E](#) for details). These galaxies are: J1250-20:S4 [Irrs], J1059-09:S4 [SB0], J1408-21:S2 [S]; J1408-21:S4 [S0], J1026-19:S6 [S0], J0400-52:S4 [Scd], J0400-52:S5

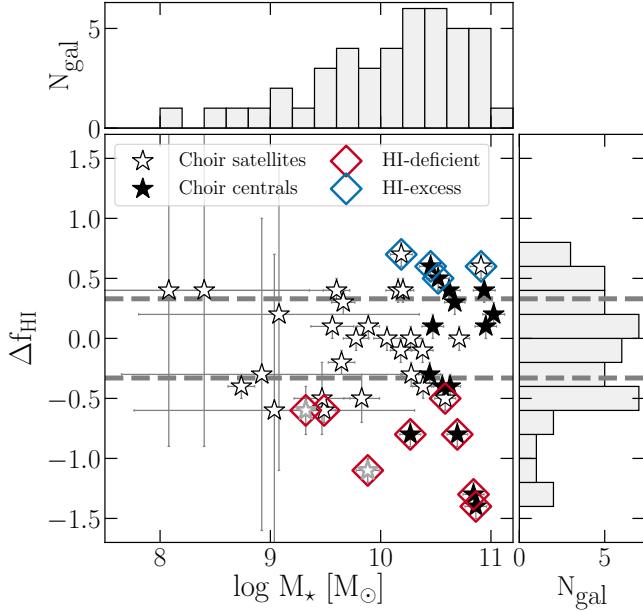


**Figure 4.** Distance of the H I mass fraction from the HIPASS running median line,  $\Delta f_{\text{HI}}$ , as a function of the stellar mass. The grey dashed horizontal lines show the mean scatter around the HIPASS running median line  $\pm 0.3$  dex. Choir galaxies are marked as stars, the solid black, outlined black, grey are respectively central galaxies, satellite galaxies and galaxies detected in H I below  $3\sigma$ . The red and blue diamonds show respectively the H I-deficient and H I-excess galaxies. The grey histograms include all Choir galaxies.

[SB pec] and J0400-52:S6 [SB pec], morphology adopted from Sweet et al. (2013). Choir J0400-52 has three galaxies that are H I-deficient; as this group is infalling into a cluster (Sweet et al. 2013; Džudžar et al. 2019a), a lower/deficient H I content in these galaxies is not surprising. See Table E1 for details on these H I-deficient galaxies.

### 3.2 Choir sample in context

The H I mass fraction versus stellar mass relation ( $M_{\text{HI}}/M_{\star}$  vs  $M_{\star}$ ) for Choir galaxies is shown in Figure 3. The H I mass fraction decreases with the stellar mass and has a sizeable scatter (Catinella et al. 2013, 2018). It is still an open question what drives the scatter in this relation, whether it is environment or internal galaxy properties, or a combination of both.

We show the H I-mass fraction of Choir galaxies in the wider context, comparing it to parent SINGG (Meurer et al. 2006), grandparent HIPASS sample using HI-WISE data from the (Parkash et al. 2018), AMIGA isolated galaxy sample (Verdes-Montenegro et al. 2005), xGASS sample (Catinella et al. 2018), and to H I-deficient (Dénes et al. 2014; Murugesan et al. 2019) and H I-excess (Lutz et al. 2018) galaxy samples.

#### 3.2.1 H I mass fraction of Choirs

In Figure 3 we show the comparison of the H I mass fraction of our Choir sample to its parent samples HIPASS and

SINGG. The parent HIPASS sample is shown with the running median of the H I mass fraction in the stellar mass bins of 0.3 dex, the solid blue line, and its 16th and 84th percentile (the blue shaded region). The parent SINGG sample is shown with the running median, the dotted blue line. We find that the H I mass fraction of the Choir galaxies is dispersed around the HIPASS median,  $\Delta f_{\text{HI}}$ , in the range  $-1.4 \leq \Delta f_{\text{HI}} [\text{dex}] \leq 0.7$ . Using the standard deviation from the HIPASS running median H I mass fraction, we find that 4 galaxies are H I-excess ( $\Delta f_{\text{HI}} > 0.4$  dex), 32 galaxies have an average H I content ( $-0.4 < \Delta f_{\text{HI}} [\text{dex}] < 0.4$ ) and 8 galaxies are H I-deficient ( $\Delta f_{\text{HI}} < -0.4$  dex). We show the distribution of the H I mass fraction around the HIPASS running median line,  $\Delta f_{\text{HI}}$ , in Figure 4, and their individual values in Table F1. In this Figure we outline the H I-excess and H I-deficient galaxies. Moreover, we show that the H I average class of galaxies represents a continuity of ‘H I-richness’ from H I-rich to H I-poor galaxies. The existence of galaxies spanning from H I-excess and H I-deficient galaxies may indicate the environmental processing in Choir groups. The two central galaxies with the lowest H I mass fraction are J0205-55:S3 and J0209-10:S4. J0205-55:S3 is presented in Figure 7 and discussed in Section 3.3. J0209-10:S4 is tidally interacting with its neighbour galaxy of similar stellar mass, J0209-10:S3 (Jones et al. 2019), which is most likely cause of its low H I mass fraction.

In Figure 3 we also show a comparison of Choir galaxies to several samples from the literature. Overall, we show that our sample has a wider stellar mass and H I mass fraction range as xGASS sample (Catinella et al. 2018). We find that a number of Choir galaxies, with high H I mass fractions, are similar to the H I-extreme galaxy sample (Lutz et al. 2018). In Džudžar et al. (2019a) we have shown that based on the specific angular momenta, gas-rich Choir galaxies are indeed comparable to the H I-extreme galaxies. In Section 3.3 we analyse the most H I-rich Choir galaxies, we show their physical sizes and the H I distribution (see Figure 8). From Figure 3 it is also evident that several Choir galaxies are H I-deficient and they are similar to samples of Dénes et al. (2016) and Murugesan et al. (2019). We describe the most H I-deficient Choirs in Section 3.3, and present them in Figure 7.

Figure 3 also shows the running median line and its 16th and 84th percentile of the isolated sample of galaxies (Analysis of the Interstellar Medium of Isolated Galaxies, AMIGA, Verdes-Montenegro et al. 2005; Fernández Lorenzo et al. 2013; Jones et al. 2018). There is no large difference between the AMIGA and the HIPASS sample as seen their median gas-mass fractions. As noted in Džudžar et al. (2019a), we find a number of galaxies with an elevated H I mass fraction with respect to galaxies in isolation. The existence of central group galaxies that are more H I-rich than the isolated central galaxies was shown by Janowiecki et al. (2017). They suggested that the group central galaxies have large H I reservoirs either due to gas accretion from cosmic web filaments or due to gas-rich mergers. We consider both scenarios: **i)** With respect to the global environment, we find Choirs both near and far away from the cosmic web filaments (see Section 4.2). **ii)** With respect to the local environment, several Choir central galaxies are experiencing interactions and exhibit signs of a merger events. Since our galaxy group sample is small we can not make a definite conclusion which effect makes a larger contribution to their H I gas content. Future large-scale

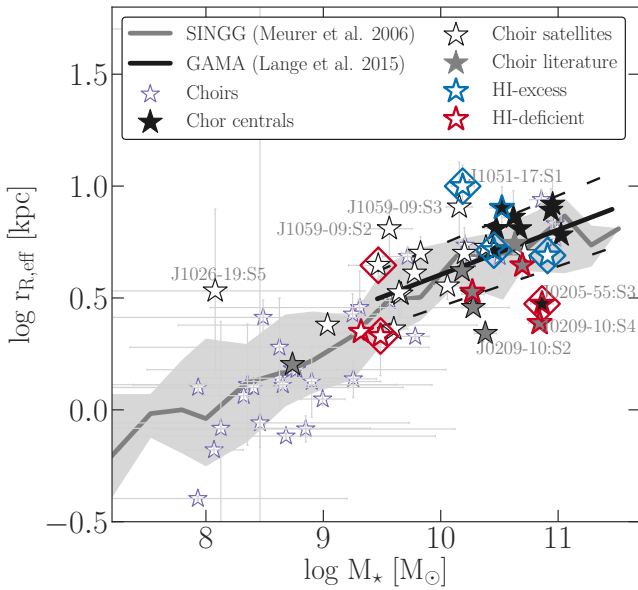


**Figure 5.** Relationship between galaxy R-band effective radii and the stellar mass. The solid markers show Choir central galaxies and the open markers show Choir satellite galaxies. The purple open stars show Choir galaxies without known HI content. The blue and red outlined stars show the Choir HI-excess and HI-deficient galaxies as discussed in Section 3.3, while diamonds denote extreme outliers from Figure 7 and 8. The solid grey line is the running median of the SINGG parent sample and the shaded regions show 16th and 84th percentile. The solid black line shows mass-size relation of late-type galaxies from the GAMA survey, while dashed lines denote  $1\sigma$  of the relation (Lange et al. 2015).

observations of the HI, with WALLABY survey (Koribalski 2012), and surveys with MeerKAT (Camilo et al. 2018) and Apertif (Oosterloo et al. 2010) will be help to discern between these scenarios.

### 3.3 HI distribution in galaxies

In this section we present and discuss the HI distribution in Choir group galaxies in order to determine whether environmental processing has an impact on it. We highlight six Choir galaxies which are respectively at the largest distance below (three most HI-deficient galaxies) and above (three most HI-excess galaxies) the running median line of the HIPASS galaxies, representing most extreme outliers (see Figure 3). We track these galaxies in the following analysis.

In Džudžar et al. (2019a) we have shown that Choir galaxies follow the established HI size-mass relation (e.g. Wang et al. 2016). We present the stellar size-mass relation in Figure 5. We show the median of the stellar mass-size relation of the Choir parent SINGG sample and its 16th and 84th percentile. Moreover, we compare SINGG size-mass relation to the relation for the late-type galaxies from the Galaxy And Mass Assembly (GAMA) survey, where they are overlapping at stellar masses above  $10^{9.5} M_{\odot}$  (Lange et al. 2015, relation for  $r$ -band). We find six (out of 69) Choir galaxies lie outside the SINGG percentiles and GAMA scatter. This infers a potential underlying morphological difference resulting in these outliers.

We compare the ratio of the HI to optical radii of Choir

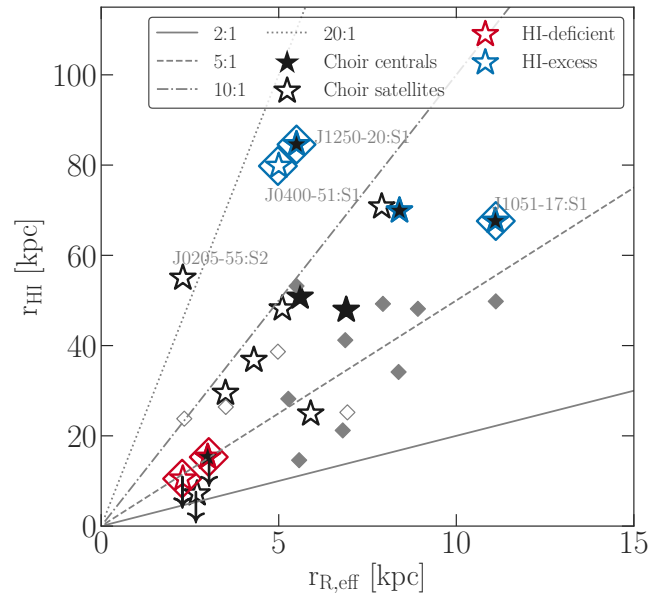


**Figure 6.** Relationship between galaxy HI radii measured at  $3 \times 10^{19} \text{cm}^{-2}$  and  $R_{\text{eff}}$  radii. The solid markers show Choir central galaxies and the open markers show Choir satellite galaxies. The blue and red outlined stars show the Choir HI-excess and HI-deficient galaxies as discussed in Section 3.3, while diamonds denote extreme outliers from Figure 7 and 8. The grey diamonds show Choir galaxies with the HI-radius measured at  $1 M_{\odot} \text{pc}^{-2}$  (Džudžar et al. 2019a).

galaxies to see if we can quantify the difference between the HI-excess and HI-deficient galaxies (see Figure 6). We use the effective R-band radii obtained from the SINGG survey (Meurer et al. 2006). The optical disc sizes are often compared to the HI disc sizes measured at  $1 M_{\odot} \text{pc}^{-2}$  (Wang et al. 2016), however, in our most HI-deficient galaxies the HI intensity does not reach this density, thus we use a column density of  $3 \times 10^{19} \text{cm}^{-2}$  and measure along the minor axis of the synthesised beam to avoid beam smearing effects (some of these measurements are upper limits, as indicated in Table F1, and they are in agreement with analytically derived HI sizes from the HI size-mass relation by Wang et al. 2016). With this approach, we are comparing the extent of the low HI column density in galaxies.

We find that 12 (out of 15) Choir galaxies have 2–10 times larger HI radii when compared to the  $r_{R,\text{eff}}$  (see Figure 6). J0205-55:S2, J0400-51:S1 and J1250-20:S1 have the largest ratio of HI radius to  $r_{R,\text{eff}}$ , of around 20 times, for HI radii measured  $3 \times 10^{19} \text{cm}^{-2}$  (corresponding to around 10 times for HI radii measured at  $1 M_{\odot} \text{pc}^{-2}$  from Džudžar et al. 2019a). The HI intensity distribution in these galaxies reaches densities larger than  $50 \times 10^{19} \text{cm}^{-2}$  as seen in Figure 8. Visually inspecting DECam optical images (Figure 8), we see that these galaxies have fainter stellar outer discs. Moreover, each of these galaxies have a peculiar morphology that can be connected with an interaction and possible accretion of the HI gas. J0400-51:S1 has visible faint stellar streams in the North, and we discussed in Džudžar et al. (2019b) how these may be related to a merger. J1250-20:S1 had clear ongoing multiple interactions and a stellar stream reaching out of a spiral arm (Džudžar et al. 2019a) and see Figure H4. Furthermore, we

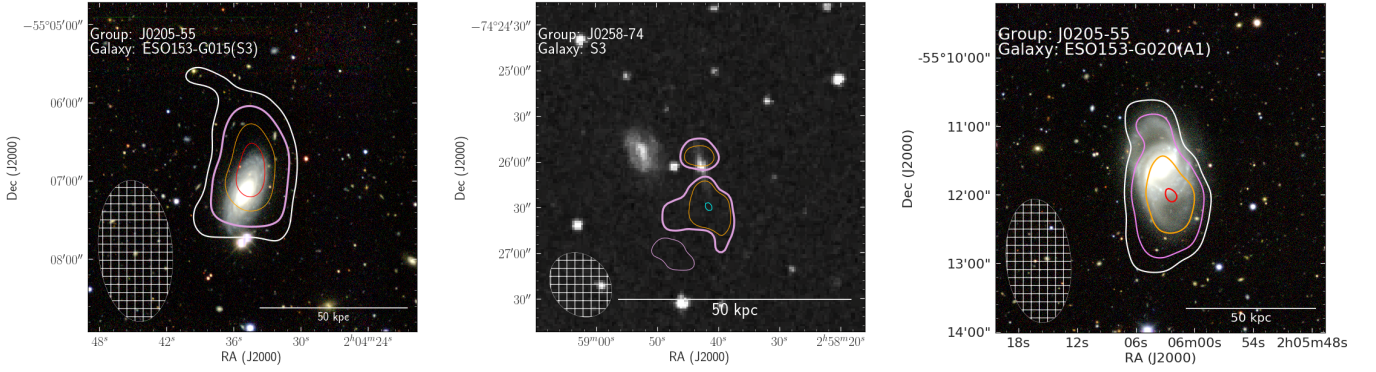


**Figure 7.** The H I intensity distribution overlaid on the DECcam  $g$ ,  $r$ ,  $i$  colour composite image (J0258-74:S3 is on the DSS2B-band image). Three H I-deficient galaxies are selected based on their distance below the  $\Delta f_{\text{H I}}$  of the HIPASS median line. The H I-density contours are as follows:  $1.5$ ,  $3$ ,  $6$  and  $9 \times 10^{19} \text{cm}^{-2}$ , respectively white, plum, orange and red. Galaxy name and its group are noted in the upper left corner in each panel. The synthesized beam is shown in the bottom left corner, and the scale bar in the bottom right corner shows 50 kpc at the group distance.

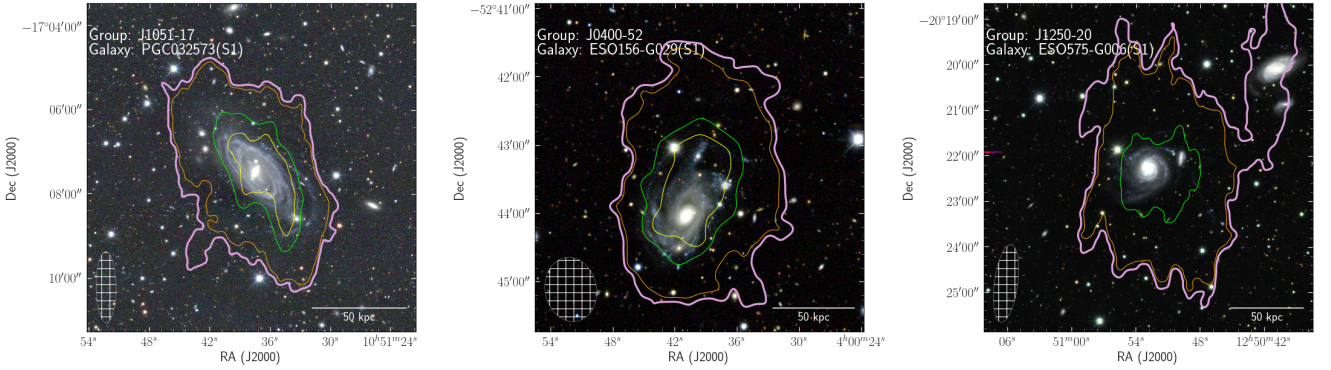


**Figure 8.** The H I intensity distribution overlaid on the DECcam  $g$ ,  $r$ ,  $i$  colour composite image. Three H I-excess galaxies are selected based on their distance above the  $\Delta f_{\text{H I}}$  of the HIPASS median line. The H I-density contours are as follows:  $1.5$ ,  $3$ ,  $6$ ,  $35$  and  $50 \times 10^{19} \text{cm}^{-2}$ , respectively white, plum, orange, green and yellow contour. Galaxy name and its group are noted in the upper left corner in each panel. The synthesized beam is shown in the bottom left corner, and the scale bar in the bottom right corner shows 50 kpc at the group distance.

find that three out of four H I-excess galaxies are interacting, or show signs of past interactions, thus it is possible that they acquired some of their H I content from mergers.

The most H I-deficient galaxies have small H I discs with respect to their optical discs (see Figure 7). Their H I size is comparable to the synthesized beam size, thus they are not fully resolved. The H I-deficient galaxies that we mapped in H I lack high H I-column densities, when compared to the H I-excess galaxies (Figure 8); their H I-column densities on average reach  $\sim 10 \times 10^{19} \text{cm}^{-2}$ . Six out of eight H I-deficient galaxies in our sample show irregular structure (optical or H I) which indicates that they most likely interacted (or currently interacting) with other galaxies within the group. This indicates that the tidal interaction is the primary cause of the H I-deficiency in Choir galaxies. In the next section we discuss individual H I-deficient and H I-excess galaxies.

### 3.3.1 Physical processes in the H I-deficient and H I-excess galaxies

The two most H I-deficient galaxies J0205-55:S3 and J0258-74:S3, with stellar masses of  $10^{10.8} M_{\odot}$  and  $10^{9.5} M_{\odot}$ , appear to have H I centres shifted from their optical centres. J0205-

55:S3 was classified as S0 galaxy (Sweet et al. 2013) however, inspecting our deep DECcam images we can re-classify it as a spiral galaxy. J0258-74:S3 is edge-on galaxy with a bright bulge, which is seen on the top right panel in Figure 7. J0258-74:S3 is in projection close to the larger J0258-74:S2 galaxy (to the east). We show J0258-74 group in Figure 12, and it is seen that the H I contours of J0258-74:S2 and J0258-74:S3 galaxy overlap. Being very close, it is likely that J0258-74:S2 and J0258-74:S3 are interacting. J0205-55:A1 (ESO153-G020) is an SBab galaxy with a stellar mass of  $10^{10.59} M_{\odot}$ . Schmitt et al. (2003) classifies ESO153-G020 as Seyfert 2 galaxy, and Soto-Pinto et al. (2019) finds indications for gas outflows at  $\sim 400 \text{km s}^{-2}$ .

Three most H I-excess galaxies in our sample are shown in the upper panel: J1051-17:S1 is a polar disc galaxy with extended low surface brightness disc, we discuss it in details in Kilborn et al. (in prep). J0400-50:S1 has highly asymmetric H I intensity distribution and disturbed gas kinematics. We presented this galaxy in Džudžar et al. (2019b) as an example of being shaped by the group environment as it is falling into a cluster. J1250-20:S1 is interacting with other galaxies in its group (with S2, S3) and it is connected to a stellar stream that contains S6 and S7. We presented this group in Džudžar

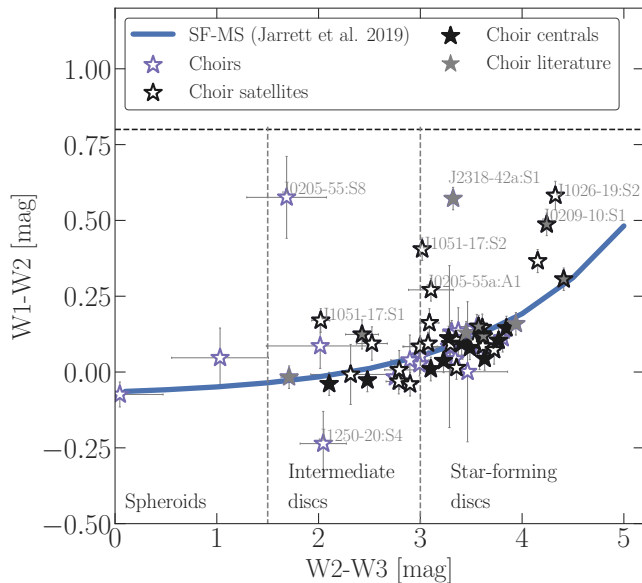


**Figure 9.** *WISE* color-color diagram of the Choir galaxies. The solid blue line shows the *WISE* colour-colour sequence (Jarrett et al. 2019). The horizontal dashed line denotes the border above which the AGN emission dominates over the host galaxy, whereas vertical dashed lines separate mid-infrared morphological classification based on colour. The solid black stars are Choir central galaxies and the open stars with the black outline are satellite galaxies for which we mapped H I content. The solid grey stars are Choir galaxies that we have H I mass from the literature. The purple open stars are all other Choir galaxies for which *WISE* bands could be measured.

et al. (2019a) and in Section H8, we also show the H I stream between S1 and S2 galaxy in Figure H4.

The presence of the interactions in H I-deficient and H I-excess galaxies indicates that the galaxy environmental processing happens through two channels: i) tidal stripping, which contributes to the loss of H I in galaxies and ii) mergers, which contributes to the enhancement of the H I in galaxies.

### 3.4 Chors in mid-infrared

We analyse the mid-infrared properties of Choir galaxies using “drizzled” *WISE* imaging Jarrett et al. (2012), in order to determine whether their star-formation activity is impacted by the group environment. The photometry was obtained from reconstructed images from *WISE* using the ICORE co-addition software Masci (2013). We show the *WISE* measurements for Choir galaxies in Table G1. For details on the *WISE* measurements see Jarrett et al. (2012) and Jarrett et al. (2013).

The flux of the W1 band traces the stellar light dominated by old stars, thus it is a good tracer of the galaxy’s stellar mass (Cluver et al. 2014). We obtain the W1 ‘in-band’ (relative to the Sun) luminosity from the W1-W2 colour, and derive the stellar mass based on the prescription of Cluver et al. (2014). The *WISE* W3 mid-infrared luminosity traces the dust-obscured star-formation activity (Cluver et al. 2017; Jarrett et al. 2019). We determine the star formation rate from the W3 band flux after removing the contribution

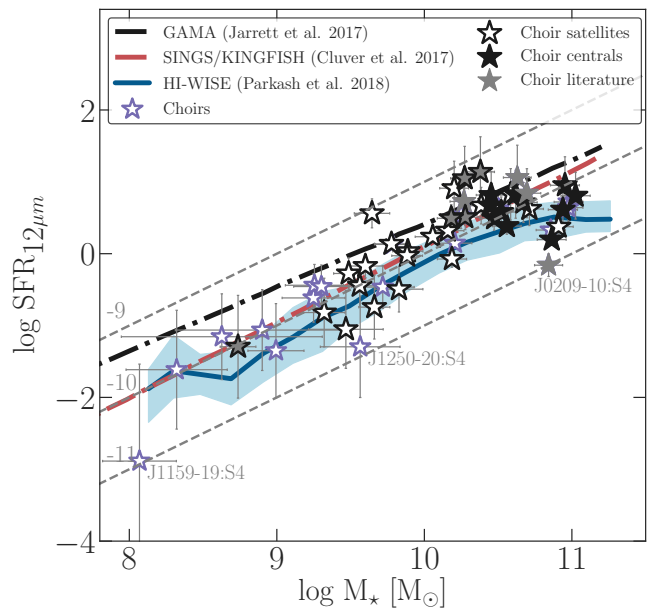


**Figure 10.** The *WISE* star formation versus stellar mass. The star symbol denote Choir galaxies as described in Figure 9. The horizontal dashed lines are denoting constant star-formation rates. The solid blue line is the running median of the star formation rate in bins of the stellar mass, obtained using galaxies from the HI-WISE data of Parkash et al. (2018). The dot-dashed red line shows the best fit line to the SINGS/KINGFISH sample, used for SFR calibration (Cluver et al. 2017). The dot-dashed black line shows the average ‘sequence’ of the equatorial GAMA G12 field (Jarrett et al. 2017).

from evolved stars, based on the prescription of Cluver et al. (2017).

We show the mid-infrared colour-colour (W1-W2 versus W2-W3) diagram of the Choir galaxies in Figure 9. It has been shown that the galaxy activity (e.g. star-forming or AGN) can be roughly determined based on galaxy’s mid-infrared colours (e.g. Jarrett et al. 2019). We see that the majority of Choir galaxies are scattered around the *WISE* colour-colour sequence (star-forming sequence) which was determined by Jarrett et al. (2019), who also show that W1-W2 colours well above the sequence have excess infrared emission due to host-dust-enshrouded AGN. The increase of the W1-W2 colour towards the right indicates the elevation of the W2 band emission by the hot dust from star-formation (Jarrett et al. 2019). We find several Choir galaxies with elevated W1-W2 colours with respect to the star-forming sequence which may be Seyfert galaxies with excess hot dust emission associated with the AGN torus (see annotations in Figure 9). However, none of them are within the AGN-dominated region (above the horizontal dashed line at W1-W2 ≈ 0.8). The most extreme outlier is J0205-55:S8, it is a small compact dwarf galaxy. J0209-10:S1 and J0205-55:A1 are classified as Seyfert 2 galaxies (de Carvalho & Coziol 1999; Schmitt et al. 2003), and J2318-42a:S1 as Seyfert 1 (Véron-Cetty & Véron 2006). J1026-19:S2 is an irregular galaxy which is tidally interacting with J1026-19:S1 (see Figure H2), and J1051-17:S2 is a high surface brightness spiral galaxy (Sweet et al. 2013).

Denotation of infrared morphological galaxy classification: spheroids, intermediate discs and star-forming discs are as-

sumed based on the colour, which was suggested in Jarrett et al. (2017). In the ‘Spheroids’ region are expected to reside galaxies with the prominent bulges, such as E or S0 galaxies, most often considered gas-depleted high mass galaxies or low burner dwarf spheroidal galaxies. Choir galaxies in this region are J1059-09:S10 ( $W2-W3 \sim 0$  mag) and J1159-19:S4 ( $W2-W3 \sim 1$  mag) and these are respectively classified as dwarf spheroidal [dS] and dwarf [D] galaxy by Sweet et al. (2013). The ‘Intermediate discs’ are described as Milky Way type galaxies, with prominent bulges and semi-quiescent discs ( $1.5 < W2-W3 < 3$ ). Galaxies in this region are possibly undergoing quenching of their star formation (Jarrett et al. 2019). The ‘Star-forming discs’ are galaxies with  $W2-W3 > 3$ , and these galaxies have ongoing active star-formation.

In Figure 10 we show the star-formation properties of the Choir galaxies. The dashed lines represent constant specific star-formation rates, and we see that the Choir galaxies are spread between  $10^{-9}$  and  $10^{-11}$   $\text{yr}^{-1}$ , thus we do not find them to be significantly quenched. We use the HI-WISE data from Parkash et al. (2018) and show the running median of the star formation rate in bins of the stellar mass. We show the running median line in Figure 10 with the blue solid line, while the shaded region shows the 16th and 84th percentile. For comparison we show the best fit line to the SINGS/KINGFISH sample, used for the calibration of the star formation rate from  $12\mu\text{m}$  (Cluver et al. 2017), and we also show the star-formation biased ‘sequence’ of the equatorial GAMA G12 field (Jarrett et al. 2017).

Three galaxies with a specific star formation rate of  $\sim 10^{-11}$   $\text{yr}^{-1}$  are: J1159-19:S4 a dwarf galaxy; J1250-20:S4 an Irr galaxy, and J0209-10:S4 an SApec galaxy. All three of these galaxies are experiencing tidal interactions, J1159-19:S4 – as seen in H I, while J1250-20:S4 and J0209-10:S4 as seen in H I and optical.

### 3.5 Choirs in context of Hickson compact groups and their evolution

Based on the group compactness, Choir groups are most similar to HCGs, as shown by the projected separation between the two most luminous galaxy members (Sweet et al. 2013). Therefore, in order to place the Choirs into the broader context of groups, we compare them to Hickson Compact Groups (HCG; Hickson 1982; Verdes-Montenegro et al. 2001). In Figure 11 we show group H I mass versus group deficiency of Choir groups and HCGs. For each Choir, the total group H I mass is taken from HIPASS, while the group H I deficiency is taken from Sweet et al. (2013). We find that Choir groups have a high mass and a low deficiency values, while HCGs are predominantly tailing towards lower group H I masses and a higher deficiency values. It is known that HCGs are comprised of galaxies with varying morphologies, and many of these galaxies are early-type galaxies. Based on the morphological type noted in (Hickson 1982) and available H I data from Verdes-Montenegro et al. (2001) we select HCGs that are comprised of only late-type galaxies: HCG2, HCG16, HCG31, HCG38, HCG80, HCG88, HCG89, HCG100 for comparison. We find that these late-type dominated HCGs are more similar to the Choir groups (see Figure 11).

In Džudžar et al. (2019a), we suggested that the Choir groups would fit into phase 1 and phase 2 of the proposed H I evolutionary scenario of HCGs (Verdes-Montenegro et al.

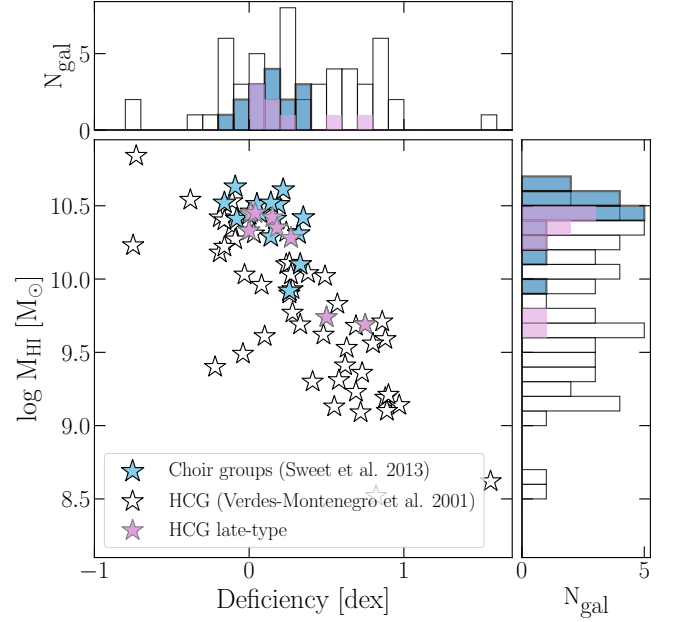


**Figure 11.** The H I mass versus deficiency for Choir groups with comparison to the Hickson compact groups. The blue stars show Choir groups. The white stars show HCGs from Verdes-Montenegro et al. (2001). The pink stars show the late-type dominated HCGs, based on the ‘MType’ from Hickson (1982) and H I properties from Verdes-Montenegro et al. (2001).

2001). We place the phase classification for each Choir group in Table H1. In summary the Verdes-Montenegro et al. (2001) evolutionary scenario of the gas content in HCGs is as follows: i) Groups in the phase 1 have an average gas content and a low level of galaxy interaction. ii) Groups in phase 2 contain H I tidal features. iii<sub>a</sub>) Groups in the phase 3a do not have H I within galaxies (it can be in the intragroup medium). iii<sub>b</sub>) Groups in the phase 3b contain the H I gas in the form of a cloud that envelopes entire group. Over time, it is likely that majority of galaxies in Choir groups will continue to deplete their gas content through star formation and interactions due to low velocity dispersion (tidal interactions, mergers), and they will become progressively more H I deficient.

Comparing gas depletion timescales from Džudžar et al. (2019a) and the crossing time for Choir groups (see Table B1), we find that the crossing time is on average shorter than the H I depletion time. Therefore, galaxy mergers that will happen in the future will most likely be gas-rich mergers<sup>2</sup>. To investigate which Choir group has conditions for galaxy mergers, we use approximated conditions from Pfister et al. (2020) for the galaxy pair mergers. Utilizing the Horizon-AGN simulation, Pfister et al. (2020) formulated a threshold on the projected distance  $d_{\text{th}}$  and redshift difference  $\Delta z_{\text{th}}$  below which galaxy pairs are likely to merge. To adapt the Pfister et al. (2020) relations for Choir groups, we use the group projected radius and radial velocity dispersion. Comparing the Choirs group velocity dispersion and the Pfister et al. (2020) criteria for optimal  $\Delta z_{\text{th}}$ , all Choir groups have optimal condition for galaxy mergers. Whereas, looking at

<sup>2</sup> Under assumptions that galaxies will go through the gravitational potential of the group.

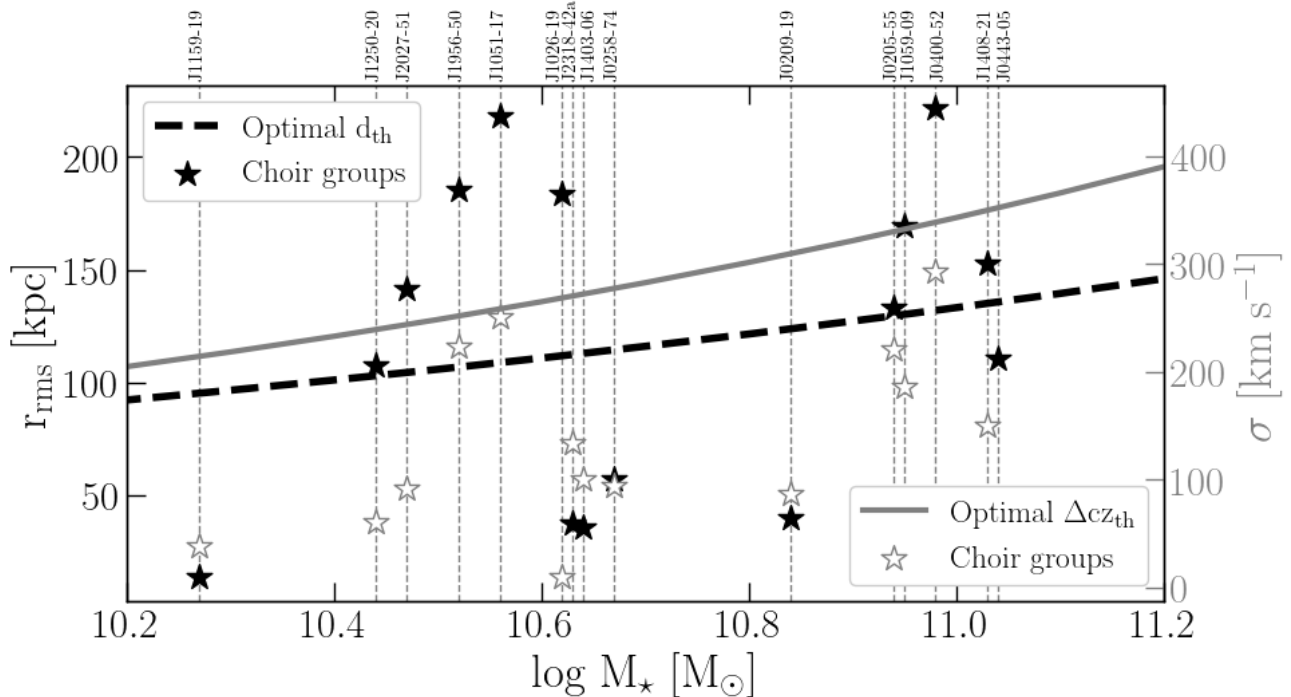


**Figure 12.** Evolution of the optimal velocity threshold  $\Delta cz_{\text{th}}$  (grey solid line) and projected distance  $d_{\text{th}}$  threshold (black dashed line) with the stellar mass of the central galaxy within given Choir group (theoretical lines are obtained from Pfister et al. (2020)). Each Choir group is represented with the solid black star in relation to the optimal  $d_{\text{th}}$  criteria, and with the open grey star in relation to the optimal  $\Delta cz_{\text{th}}$  criteria (respectively Choir groups are presented with their projected radius and radial velocity dispersion). The vertical dashed lines connect the same Choir groups in both criteria, and they are annotated at the top of the Figure.

the group projected radii, we find that seven groups do not satisfy imposed criteria, two are on the threshold and six satisfy imposed criteria. Even though this analysis is rough, since groups have more massive gravitational potential than galaxy pairs, with such approach we obtained lower limits on the given conditions for galaxy mergers. Choir groups J1026-19, J1059-09 and J1408-21 are above optimal  $d_{\text{th}}$  threshold, however, they contain galaxies that are already interacting, while J0400-52 is infalling into a cluster. To better constrain minimal galaxy separation for mergers, this work requires further studies of Choir group analogues in simulations.

Based on the mentioned parameters, we suggest that some of the Choir groups will go through a phase of compact groups or they will end up as an optical fossil group, depending on the global environment around them. A fossil group is usually defined as a galaxy group with a single dominant elliptical galaxy with an X-ray luminosity of  $L_{X,\text{bol}} \geq 10^{42} h_{50}^{-2} \text{ erg s}^{-1}$  and with at least 2.0 magnitude difference from the second brightest group galaxy (e.g. Jones et al. 2003). We define an optical fossil group, where the magnitude difference between the brightest galaxy and second brightest galaxy is larger than 2 magnitudes, but we do not impose that they are X-ray bright as in the definition of fossil groups by Ponman et al. (1994).

Nine of the Choir groups have galaxies in the neighbourhood and thus they have a possibility of forming a HCG like group in the future, assuming that these galaxies will ‘fall’ towards the same potential well (see Section 4 and Appendix I). These groups are: J0205-55, J0209-10, J0443-05, J1051-17, 1059-09, J1159-19, J1403-06, J2027-51 and J2318-42a.

Choir J1159-19 is a compact group which contains a one armed spiral galaxy and three dwarf galaxies. J1159-19 meets the criteria for an optical fossil group. All galaxies within this group are interacting, as seen in their H I distribution (see Figure I6) and they will most likely merge in the future. A further five Choirs lie in a fairly isolated environment are more likely to create an optical fossil group, similar to the current state of J1159-19. In these cases, there are fewer galaxies that can merge and thus they will not be able to satisfy criteria to be classified as HCGs. These groups are: J0258-74, J1026-19, J1250-20, J1408-21 and J1956-50.

One Choir group, J0400-51, is infalling into a cluster. Džudžar et al. (2019b) proposed that the gas-rich galaxy within this group (ESO156-G029) will be under the effects of ram-pressure once the galaxy approaches closer to the cluster centre. Moreover, we used this galaxy as an example to show that group pre-processing is important in its evolution.

#### 4 GLOBAL ENVIRONMENT AROUND THE CHOIR GROUPS

In this section we explore the wider environment of the Choir groups and its impact on their H I content. We present results from the local and global environment around Choir groups, the former corresponds to the neighbouring galaxies and the latter corresponds to the position of Choirs within cosmic web filaments.

#### 4.1 Wider environment of the Choir groups

We analyse the wider environment of the Choir groups to determine the environment outside the 15' of the SINGG field of view. We made a script in `python` to query for sources around the HIPASS detection in NASA/IPAC Extragalactic Database (NED). We use RA, Dec and the recessional velocity  $V_{\text{HI}}$  of Choir groups from Sweet et al. (2013), and make a query typically  $\sim 4$  degrees around each Choir group. The initial result is sub-sampled for only 'G' objects i.e. only galaxies, as there are sources which mark position of groups, triplets etc. The obtained catalogue is cross-matched with the 2MASS Extended Source Image Server to obtain the Ks-band total magnitude in order to make a magnitude limited sample.

We use galaxies with known Ks-magnitude, recessional velocity between  $\pm 1000 \text{ km s}^{-1}$  from the Choir group velocity, and  $< 0.5$  degree projected separation from the HIPASS centre, to compute the Ks weighted mean position of the group centroid. Using this sample of galaxies we re-compute the projected distances for each galaxy from the group centroid. We use this data to map the galaxies with their velocity difference (with respect to the Choir group) around all Choir groups (see panel c in Appendix I). We also use the projected angular separation versus the velocity difference of each galaxy from the group mean velocity to show Choir caustics curves in order to map the group potential and find potential galaxies that will merge with Choir groups (see panel d in Appendix I).

We find Choirs in low density environments (J0258-74, J1026-19, J1250-20, J1408-21 and J1956-50), Choirs with nearby, possible infalling galaxies (J0205-55, J1051-17) and Choirs which are potentially part of a larger structure (J0400-52, J1159-19 and J2027-51). We present results for each Choir group individually in Appendix H and Appendix I: panel c and d in Figures.

#### 4.2 Choirs position with respect to the filaments

We explore whether the Choir groups have a 'special' position in the cosmic web. Janowiecki et al. (2017) suggested that the HI-rich central galaxies in the group environment are HI-rich due to gas accretion from cosmic web filaments, as groups can be positioned in the intersection of those filaments. Kleiner et al. (2017) used the 6 degree Field Galaxy Survey (6dFGS) and the Discrete Persistent Structures Extractor (DisPerSe) to map the filaments in the local Universe. Furthermore, combining filaments and data from HIPASS, they found that galaxies near filaments, with  $M_{\star} \geq 10^{11} M_{\odot}$ , have higher HI mass fractions than the control sample. Utilizing catalogue of the filaments by Kleiner et al. (2017), we derive the distances to the nearest filament for Choir galaxy groups, see Table 2.

Exploring 14 Choir galaxy groups (J0400-52 is excluded as it is near galaxy cluster), we find that seven are within  $\leq 1$  Mpc, one is at  $\sim 2$  Mpc and six are at  $\geq 4$  Mpc from the nearest filament. We find only two Choir groups near the intersection of filaments: J1408-21 and J1059-09. Based on the HI-mass fraction, central galaxies in J1408-21 and J1059-09 have average gas content. Furthermore, we find two Choir groups that are more than 10 Mpc away from the nearest filament: J0258-74 and J1956-50. These groups can be classified as being in a void, as distances of  $\sim 10$  Mpc are considered as voids (Kuutma et al. 2017). The central galaxy in J0258-74 has an average HI-mass fraction, while central in J1956-50

**Table 2.** Distances to the nearest filaments

ID (1)	RA [deg] (2)	DEC [deg] (3)	z (4)	D [Mpc] (5)
Choirs				
J0205-55	31.272800	-55.111801	0.02172	4.29
J0209-10	32.427898	-10.183700	0.01261	1.06
J0258-74	44.527000	-74.456299	0.01634	11.90
J0400-52 <sup>a</sup>	60.170101	-52.734100	0.03526	...
J0443-05	70.932899	-5.319420	0.01611	0.22
J1026-19	156.669998	-19.051100	0.03152	1.67
J1051-17	162.906006	-17.124800	0.01938	0.11
J1059-09	164.817993	-9.793930	0.02849	0.16
J1159-19	179.876007	-19.265800	0.00584	0.62
J1250-20	192.720001	-20.371000	0.02662	4.18
J1403-06	210.854004	-6.069210	0.00957	6.61
J1408-21	212.175003	-21.597200	0.02989	0.87
J1956-50	299.190002	-50.055599	0.02568	13.70
J2027-51	307.027008	-51.691601	0.02031	3.86
2318-42a	349.597992	-42.369999	0.00537	0.61

<sup>a</sup> Excluded, because it is a part of a galaxy cluster.

(1) Group name: HIPASS+ID; (2) Right Ascension (J2000) from HIPASS; (3) Declination (J2000) from HIPASS; (4) Redshift, computed from the distances from Džudžar et al. (2019a) as  $z = (d \times H_0) / c$ , where  $d$  is the distance to the source in Mpc,  $H_0 = 70 \text{ km s}^{-1} \text{ Mpc}^{-1}$ ,  $c = 3 \times 10^5 \text{ km s}^{-1}$ ; (5) Distance to the nearest filament in Mpc, for details see Kleiner et al. (2017).

has a higher than average HI-mass fraction. We conclude that Choir groups span a range of global environments, from being in a void to being near an intersection of filaments, thus they are not within a unique position in the cosmic web. While gas accretion from the cosmic web may be occurring in some Choir groups, it is not shown to drastically enhance the HI content as the Choir groups with similar HI properties span all global environments.

#### 4.3 Global classification of Choir groups

In summary, the Choir groups whose HI content we mapped can be classify into several broad categories:

- **Isolated groups**, embedded in the low density global environment: J0258-74, J1026-19, J1250-20, J1408-21, J1956-50.
- **Cluster infalling group**: J0400-52.
- **Groups with tidal interactions**: J1159-19, J1059-09, J1026-19, J1408-21, J1250-20, J0400-52.
- **Merging subgroups**: J0205-55 (composed of J0205-55a and J0205-55b), J1051-17
- **Potentially part of the larger structure**: J2027-51, J1159-19.

## 5 SUMMARY AND CONCLUSIONS

In this paper we present and explore the resolved HI content of galaxies in HI-rich and late-type dominated groups named 'Choirs'. We present the Choir galaxy sample in context by comparing it to its parent sample Survey of Ionization in Neutral Gas Galaxies, SINGG (Meurer et al. 2006) and grandparent sample HI Parkes All Sky Survey, HIPASS (Barnes et al. 2001) as well as to several galaxy samples from the literature: Analysis of the Interstellar Medium of Isolated

Galaxies, AMIGA (Verdes-Montenegro et al. 2005), The extended GALEX Arcibo SDSS Survey, xGASS (Catinella et al. 2018), and Hickson Compact Groups, HCG (Hickson 1982; Verdes-Montenegro et al. 2001).

Within 13 Choir groups discussed in this paper, 44 galaxies, out of 78, are detected in H I emission, see Figure 2. Deriving the H I detection limits and the angular sizes of the galaxies (see Figure E1), we find that eight galaxies, out of 34, are not detected due to a potential H I deficiency, and the expected H I content of remaining galaxies lies below our detection limit.

We quantify the dispersion in the H I mass fraction ( $f_{\text{HI}}$ ) of the Choir galaxies with respect to their HIPASS grandparent sample, using HIPASS running median of the H I mass fraction in the stellar mass bins of 0.3 dex (see Figure 3). We find that the H I mass fraction of the Choir galaxies is dispersed around the median,  $\Delta f_{\text{HI}}$ , in the range  $-1.4 \leq \Delta f_{\text{HI}} [\text{dex}] \leq 0.7$  (see Figure 4). Using the standard deviation from the HIPASS running median of the H I mass fraction, we find that 4 galaxies are H I-excess ( $\Delta f_{\text{HI}} > 0.4$  dex), 32 galaxies have an average H I content ( $-0.4 < \Delta f_{\text{HI}} [\text{dex}] < 0.4$ ) and 8 galaxies are H I-deficient ( $\Delta f_{\text{HI}} < (-0.4$  dex)). The existence of the H I-excess and H I-deficient galaxies in Choir groups indicates the presence of the environmental processing (e.g. Chung et al. 2009; Dénes et al. 2016; Ellison et al. 2018), which we further explore.

We map the H I distribution in galaxies within the Choir groups, and highlight six with an extreme H I content, the three most H I-excess and the three most H I-deficient, in order to determine whether their H I content is a result of galaxy environmental processing. The most H I-excess galaxy is J1051-17:S1, with  $\log M_{\star} = 10.19 \pm 0.10$  and  $\log M_{\text{HI}} = 10.43 \pm 0.02$ . J1051-17:S1 has  $\sim 4.7$  times more H I than expected of a galaxy with a similar stellar mass. The most H I-deficient galaxy is J0205-55:S3, with  $\log M_{\star} = 10.86 \pm 0.10$  and  $\log M_{\text{HI}} = 8.65 \pm 0.13$ . J0205-55:S3 has  $\sim 23$  times less H I than expected of a galaxy with a similar stellar mass. We show that the H I-excess galaxies have a large H I-to-R-band radii ratio and exhibit signs of past or current galaxy-galaxy interactions (see Figure 8). On the other hand, the H I-deficient galaxies have a small H I-to-R-band radii ratio (see Figure 7) and their H I column densities do not reach high values (peak at  $\sim 10 \times 10^{19} \text{ cm}^{-2}$ ). Six out of eight H I deficient galaxies have irregular structure (optical or H I) which indicates that they most likely experienced H I stripping due to tidal interactions with the other galaxies within the group. The H I-excess galaxies show a range of peculiarities in their optical morphology, e.g. galaxy with a polar ring (J1051-17:S1), galaxy with asymmetric H I distribution (J0400-52:S1), and galaxy with stellar streams (J1250-20:S1). These peculiarities indicate past and/or current galaxy interactions which can lead to the enhancement of the H I content i.e. an environmental processing ‘boosts’ the H I content (e.g. Ellison et al. 2018). Another possibility of the acquiring of the H I is through cold gas accretion from cosmic web filaments (Kereš et al. 2005) however, our observations are not sensitive enough to detect it. The presence of the H I-deficient and H I-excess galaxies shows that the galaxy environmental processing happens through two channels: i) tidal stripping, which contributes to the loss of H I in galaxies and ii) mergers, which contributes to the enhancement of the H I in galaxies.

We explore the impact of the environmental processing on

the mid-infrared galaxy properties using the data from *WISE*. We show that all but three Choir galaxies have regular star formation rate. Three galaxies have a low specific star formation rate of  $\sim 10^{-11} \text{ yr}^{-1}$ , two are dwarf galaxies with low star formation and one is SApec galaxy which may be on a path to quenching (e.g. Jarrett et al. 2019), and all three of them are experiencing tidal interactions. Out of the 56 galaxies with obtained  $12\mu\text{m}$  we do not find any heavily dust-obscured, nor starburst-like star formation rates in Choir galaxies. We find that seven, out of 48, Choir galaxies have elevated W1-W2 colours with respect to the star-forming sequence thus they are potentially Seyfert galaxies (see Figure 9). This indicates that galaxy environmental processing is more perceptible in the H I content than in the mid-infrared properties of Choir galaxies.

We discuss Choir groups in the context of Hickson compact groups and explore their evolutionary scenarios. We discuss the possible future of Choir groups taking into consideration the H I depletion timescale, crossing time, velocity dispersion and the global environment around these groups. Since the crossing time is shorter than the depletion time, mergers that will happen in the future are likely to be gas-rich. This scenario points out that the H I from galaxies is potentially going to be stripped off during the galaxy interactions, forming tidal bridges and tails which will likely disperse into the intra-group medium. Exploring the global environment around Choir groups (see Appendix I), we find that nine Choir groups might go through a phase of being more compact, similar to HCGs: J0205-55, J0209-10, J0443-05, J1051-17, 1059-09, J1159-19, J1403-06, J2027-51 and J2318-42a. Such phase is possible due to the low velocity dispersion of Choirs and a number of nearby galaxies which are likely to merge with a group. Choir groups that are embedded in isolated environments may merge only with group members, possibly forming a HIPASS J1159-19 type of system (see Figure I6). These groups are: J0258-74, J1026-19, J1250-20, J1408-21 and J1956-50. The only exception to these scenarios is the J0400-52 group as it is infalling into a cluster Džudžar et al. (2019b). The rapid H I-removal process, ram-pressure, is expected in the S1 galaxy within J0400-52 once it approaches the cluster centre Džudžar et al. (2019b). J0400-52 already contains galaxies that are either group pre-processing, or it is possible that they are the ‘backslash’ galaxies i.e. already fell through the cluster potential well, as discussed in Section H3. In our future work we aim to further probe possible evolutionary pathways for Choir groups by tracing their analogues in simulations.

We present each Choir group individually showing its H I content and global environment. We explore the global environment around the Choir groups and their position in the cosmic web. We find that seven Choir groups are within  $\leq 1$  Mpc, one is at  $\sim 2$  Mpc and six are at  $\geq 4$  Mpc from the nearest cosmic web filament. We conclude that Choir groups do not have a unique position in the cosmic web. Our observations show that environmental processing in the Choir groups, in the form of tidal interaction and mergers, is present regardless of their global environment. We find galaxy interactions in the group that is in isolation (in void, J0258-74) and in the groups that are near the intersection of the cosmic web filaments, J1059-09 and J1408-21.

All our results indicate that the galaxy environmental pro-

cessing is already present in the H I-rich groups that are dominated by the late-type galaxies. With the upcoming H I WALLABY (Koribalski 2012) survey, and surveys with Apertif (Oosterloo et al. 2010) and MeerKAT (Camilo et al. 2018) we will obtain a large statistical sample of such H I-rich galaxy groups. Using those data we will be able to further probe the initial stages of galaxy environmental processing in groups.

## DATA AVAILABILITY

The data underlying this article are available in the article.

## ACKNOWLEDGEMENTS

We thank the anonymous referee for their comments and suggestions which improved this paper.

Robert Džudžar (RD) acknowledges support by a Swinburne University Postgraduate Research Awards (SUPRA) scholarship throughout major part of this work.

RD would like to thank Chandrashekar Murugesan and Michelle Cluver for insightful discussions. RD would also like to thank Fiona Audcent-Ross for help with the SINGG catalogue, thank you extends to the entire SINGG survey team. RD acknowledges financial support (Covid-19 fund) from the Astronomical Society of Australia that helped finishing this paper.

Parts of this research were conducted by the Australian Research Council Centre of Excellence for All Sky Astrophysics in 3 Dimensions (ASTRO 3D), through project number CE170100013.

Dane Kleiner acknowledges funding received from the European Research Council (ERC) under the European Union’s Horizon 2020 research and innovation programme (grant agreement no. 679627)

The Australia Telescope Compact Array is part of the Australia Telescope National Facility which is funded by the Australian Government for operation as a National Facility managed by CSIRO.

The National Radio Astronomy Observatory is a facility of the National Science Foundation operated under cooperative agreement by Associated Universities, Inc.

Based on observations at Cerro Tololo Inter-American Observatory, National Optical Astronomy Observatory (NOAO Prop. AAT/13A/02; PI: Sarah M. Sweet), which is operated by the Association of Universities for Research in Astronomy (AURA) under a cooperative agreement with the National Science Foundation.

This work was performed on the OzSTAR national facility at Swinburne University of Technology. OzSTAR is funded by Swinburne University of Technology and the National Collaborative Research Infrastructure Strategy (NCRIS).

This work was written on the collaborative Overleaf platform <https://www.overleaf.com>.

This publication makes use of data products from the Wide-field Infrared Survey Explorer, which is a joint project of the University of California, Los Angeles, and the Jet Propulsion Laboratory/California Institute of Technology, funded by the National Aeronautics and Space Administration.

This research has made use of the NASA/IPAC Extragalactic Database (NED), which is operated by the Jet Propulsion

Laboratory, California Institute of Technology, under contract with the National Aeronautics and Space Administration.

This publication makes use of data products from the Two Micron All Sky Survey, which is a joint project of the University of Massachusetts and the Infrared Processing and Analysis Center/California Institute of Technology, funded by the National Aeronautics and Space Administration and the National Science Foundation.

This research has made use of the VizieR catalogue access tool, CDS, Strasbourg, France. The original description of the VizieR service was published in A&AS 143, 23.

This project used public archival data from the Dark Energy Survey (DES). Funding for the DES Projects has been provided by the U.S. Department of Energy, the U.S. National Science Foundation, the Ministry of Science and Education of Spain, the Science and Technology Facilities Council of the United Kingdom, the Higher Education Funding Council for England, the National Center for Supercomputing Applications at the University of Illinois at Urbana-Champaign, the Kavli Institute of Cosmological Physics at the University of Chicago, the Center for Cosmology and Astro-Particle Physics at the Ohio State University, the Mitchell Institute for Fundamental Physics and Astronomy at Texas A&M University, Financiadora de Estudos e Projetos, Fundação Carlos Chagas Filho de Amparo à Pesquisa do Estado do Rio de Janeiro, Conselho Nacional de Desenvolvimento Científico e Tecnológico and the Ministério da Ciência, Tecnologia e Inovação, the Deutsche Forschungsgemeinschaft, and the Collaborating Institutions in the Dark Energy Survey. The Collaborating Institutions are Argonne National Laboratory, the University of California at Santa Cruz, the University of Cambridge, Centro de Investigaciones Energéticas, Medioambientales y Tecnológicas-Madrid, the University of Chicago, University College London, the DES-Brazil Consortium, the University of Edinburgh, the Eidgenössische Technische Hochschule (ETH) Zürich, Fermi National Accelerator Laboratory, the University of Illinois at Urbana-Champaign, the Institut de Ciències de l’Espai (IEEC/CSIC), the Institut de Física d’Altes Energies, Lawrence Berkeley National Laboratory, the Ludwig-Maximilians Universität München and the associated Excellence Cluster Universe, the University of Michigan, the National Optical Astronomy Observatory, the University of Nottingham, The Ohio State University, the OzDES Membership Consortium, the University of Pennsylvania, the University of Portsmouth, SLAC National Accelerator Laboratory, Stanford University, the University of Sussex, and Texas A&M University.

This research has made use of python <https://www.python.org> and python packages: astropy (Astropy Collaboration et al. 2013, 2018), matplotlib <http://matplotlib.org/> (Hunter 2007), APLpy <https://aplpy.github.io/>, pandas (McKinney 2010), Jupyter notebook <https://github.com/jupyter/notebook>, NumPy <http://www.numpy.org/> (van der Walt et al. 2011), SciPy <https://www.scipy.org/> (Jones et al. 2001) and CMasher <https://github.com/1313e/CMasher> (van der Velden 2020).

## REFERENCES

Astropy Collaboration et al., 2013, *A&A*, 558, A33

- Astropy Collaboration et al., 2018, *AJ*, **156**, 123
- Barnes D. G., Webster R. L., 2001, *MNRAS*, **324**, 859
- Barnes D. G., et al., 2001, *MNRAS*, **322**, 486
- Berlind A. A., et al., 2006, *ApJS*, **167**, 1
- Bigiel F., Blitz L., 2012, *ApJ*, **756**, 183
- Borthakur S., Yun M. S., Verdes-Montenegro L., Heckman T. M., Zhu G., Braatz J. A., 2015, *The Astrophysical Journal*, **812**, 78
- Brough S., Forbes D. A., Kilborn V. A., Couch W., Colless M., 2006, *Monthly Notices of the Royal Astronomical Society*, **369**, 1351
- Brown T., et al., 2017, *MNRAS*, **466**, 1275
- Camilo F., et al., 2018, *ApJ*, **856**, 180
- Catinella B., et al., 2013, *MNRAS*, **436**, 34
- Catinella B., et al., 2018, *MNRAS*, **476**, 875
- Chromey F. R., Elmegreen D. M., Mandell A., McDermott J., 1998, *The Astronomical Journal*, **115**, 2331
- Chung A., van Gorkom J. H., Kenney J. D. P., Crowl H., Vollmer B., 2009, *AJ*, **138**, 1741
- Cluver M. E., et al., 2014, *ApJ*, **782**, 90
- Cluver M. E., Jarrett T. H., Dale D. A., Smith J. D. T., August T., Brown M. J. I., 2017, *ApJ*, **850**, 68
- Cortese L., Catinella B., Boissier S., Boselli A., Heinis S., 2011, *MNRAS*, **415**, 1797
- Coziol R., Plauchu-Frayn I., 2007, *AJ*, **133**, 2630
- Coziol R., Iovino A., de Carvalho R. R., 2000, *AJ*, **120**, 47
- Crook A. C., Huchra J. P., Martimbeau N., Masters K. L., Jarrett T., Macri L. M., 2007, *ApJ*, **655**, 790
- Dahlem M., 2005, *A&A*, **429**, L5
- Dénes H., Kilborn V. A., Koribalski B. S., 2014, *MNRAS*, **444**, 667
- Dénes H., Kilborn V. A., Koribalski B. S., Wong O. I., 2016, *MNRAS*, **455**, 1294
- Dressler A., 1980, *ApJ*, **236**, 351
- Džudžar R., et al., 2019a, *MNRAS*, **483**, 5409
- Džudžar R., Kilborn V., Murugesan C., Meurer G., Sweet S. M., Putman M., 2019b, *MNRAS*, **490**, L6
- Ellison S. L., Catinella B., Cortese L., 2018, *MNRAS*, **478**, 3447
- Fernández Lorenzo M., Sulentic J., Verdes-Montenegro L., Argudo-Fernández M., 2013, *MNRAS*, **434**, 325
- Freeland E., Stilp A., Wilcots E., 2009, *AJ*, **138**, 295
- Garcia A. M., 1993, *A&AS*, **100**, 47
- Giovanelli R., Haynes M. P., 1985, *ApJ*, **292**, 404
- Giovanelli R., et al., 2005, *AJ*, **130**, 2598
- Gooch R., 1996, *Karma: a Visualization Test-Bed*. p. 80
- Gunn J. E., Gott III J. R., 1972, *ApJ*, **176**, 1
- Haynes M. P., Giovanelli R., 1984, *AJ*, **89**, 758
- Hess K. M., Wilcots E. M., 2013, *AJ*, **146**, 124
- Hickson P., 1982, *ApJ*, **255**, 382
- Hickson P., 1997, arXiv.org, pp 357–388
- Hunter J. D., 2007, *Computing In Science & Engineering*, **9**, 90
- Janowiecki S., Catinella B., Cortese L., Saintonge A., Brown T., Wang J., 2017, arXiv.org, p. stx046
- Jarrett T. H., et al., 2011, *ApJ*, **735**, 112
- Jarrett T. H., et al., 2012, *The Astronomical Journal*, **144**, 68
- Jarrett T. H., et al., 2013, *AJ*, **145**, 6
- Jarrett T. H., et al., 2017, *The Astrophysical Journal*, **836**, 182
- Jarrett T. H., Cluver M. E., Brown M. J. I., Dale D. A., Tsai C. W., Masci F., 2019, *ApJS*, **245**, 25
- Jones E., Oliphant T., Peterson P., et al., 2001, *SciPy: Open source scientific tools for Python*, <http://www.scipy.org/>
- Jones L. R., Ponman T. J., Horton A., Babul A., Ebeling H., Burke D. J., 2003, *MNRAS*, **343**, 627
- Jones M. G., et al., 2018, *A&A*, **609**, A17
- Jones M. G., et al., 2019, *A&A*, **632**, A78
- Kereš D., Katz N., Weinberg D. H., Davé R., 2005, *MNRAS*, **363**, 2
- Kilborn V. A., Koribalski B. S., Forbes D. A., Barnes D. G., Musgrave R. C., 2005, *MNRAS*, **356**, 77
- Kilborn V. A., Forbes D. A., Barnes D. G., Koribalski B. S., Brough S., Kern K., 2009, *MNRAS*, **400**, 1962
- Kim J., Chung A., Wong O. I., Lee B., Sung E.-C., Staveley-Smith L., 2017, *A&A*, **605**, A54
- Kleiner D., Pimblett K. A., Jones D. H., Koribalski B. S., Serra P., 2017, *MNRAS*, **466**, 4692
- Konstantopoulos I. S., et al., 2010, *ApJ*, **723**, 197
- Koribalski B. S., 2012, *Publ. Astron. Soc. Australia*, **29**, 359
- Koribalski B. S., 2020, arXiv e-prints, p. arXiv:2002.07312
- Kuutma T., Tamm A., Tempel E., 2017, *A&A*, **600**, L6
- Lacerna I., Rodríguez-Puebla A., Avila-Reese V., Hernández-Toledo H. M., 2014, *ApJ*, **788**, 29
- Lange R., et al., 2015, *Monthly Notices of the Royal Astronomical Society*, **447**, 2603
- Larson R. B., Tinsley B. M., Caldwell C. N., 1980, *ApJ*, **237**, 692
- Lewis I., et al., 2002, *MNRAS*, **334**, 673
- Lutz K. A., et al., 2018, preprint, (arXiv:1802.04043)
- Malphrus B. K., Simpson C. E., Gottesman S. T., Hawarden T. G., 1997, *AJ*, **114**, 1427
- Masci F., 2013, arXiv e-prints, p. arXiv:1301.2718
- Mathewson D. S., Ford V. L., Buchhorn M., 1992, *ApJS*, **81**, 413
- McKinney W., 2010, in van der Walt S., Millman J., eds, *Proceedings of the 9th Python in Science Conference*. pp 51 – 56
- McMullin J. P., Waters B., Schiebel D., Young W., Golap K., 2007, in Shaw R. A., Hill F., Bell D. J., eds, *Astronomical Society of the Pacific Conference Series Vol. 376, Astronomical Data Analysis Software and Systems XVI*. p. 127
- Meurer G. R., et al., 2006, *ApJS*, **165**, 307
- Meyer M. J., et al., 2004, *MNRAS*, **350**, 1195
- Mould J. R., et al., 2000, *ApJ*, **529**, 786
- Murugesan C., Kilborn V., Obreschkow D., Glazebrook K., Lutz K., Džudžar R., Dénes H., 2019, *MNRAS*, **483**, 2398
- Nulsen P. E. J., 1982, *MNRAS*, **198**, 1007
- Obreschkow D., Glazebrook K., Kilborn V., Lutz K., 2016, *ApJ*, **824**, L26
- Oosterloo T., et al., 2010, *MNRAS*, **409**, 500
- Oosterloo T. A., Zhang M.-L., Lucero D. M., Carignan C., 2018, preprint, (arXiv:1803.08263)
- Parkash V., Brown M. J. I., Jarrett T. H., Bonne N. J., 2018, *ApJ*, **864**, 40
- Pfister H., Dotti M., Laigle C., Dubois Y., Volonteri M., 2020, *MNRAS*, **493**, 922
- Phookun B., Mundy L. G., Teuben P. J., Wainscoat R. J., 1992, *ApJ*, **400**, 516
- Pisano D. J., Barnes D. G., Gibson B. K., Staveley-Smith L., Freeman K. C., Kilborn V. A., 2007, *Astrophysics and Space Science Proceedings*, **3**, 319
- Pisano D. J., Barnes D. G., Staveley-Smith L., Gibson B. K., Kilborn V. A., Freeman K. C., 2011, *ApJS*, **197**, 28
- Poggianti B. M., De Lucia G., Varela J., Aragon-Salamanca A., Finn R., Desai V., von der Linden A., White S. D. M., 2010, *MNRAS*, **405**, 995
- Ponman T. J., Allan D. J., Jones L. R., Merrifield M., McHardy I. M., Lehto H. J., Luppino G. A., 1994, *Nature*, **369**, 462
- Rots A. H., Bosma A., van der Hulst J. M., Athanassoula E., Crane P. C., 1990, *AJ*, **100**, 387
- Ryder S. D., et al., 2001, *ApJ*, **555**, 232
- Sardone A., Pisano D. J., Burke-Spolaor S., Mascoop J. L., Pol N., 2019, *ApJ*, **871**, L31
- Sault R. J., Teuben P. J., Wright M. C. H., 1995, in Shaw R. A., Payne H. E., Hayes J. J. E., eds, *Astronomical Society of the Pacific Conference Series Vol. 77, Astronomical Data Analysis Software and Systems IV*. p. 433 (arXiv:astro-ph/0612759)
- Schmitt H. R., Donley J. L., Antonucci R. R. J., Hutchings J. B., Kinney A. L., 2003, *ApJS*, **148**, 327
- Scott T. C., Cortese L., Brinks E., Bravo-Alfaro H., Auld R., Minchin R., 2012, *Monthly Notices of the Royal Astronomical Society: Letters*, **419**, L19

- Sengupta C., Balasubramanyam R., 2006, *MNRAS*, **369**, 360
- Sengupta C., Scott T. C., Paudel S., Dwarakanath K. S., Saikia D. J., Sohn B. W., 2017, *Monthly Notices of the Royal Astronomical Society*, 469, 3629
- Skibba R. A., van den Bosch F. C., Yang X., More S., Mo H., Fontanot F., 2011, *MNRAS*, **410**, 417
- Solanes J. M., Manrique A., García-Gómez C., González-Casado G., Giovanelli R., Haynes M. P., 2001, *The Astrophysical Journal*, 548, 97
- Soto-Pinto P., et al., 2019, *MNRAS*, **489**, 4111
- Stevens A. R. H., Brown T., 2017, *MNRAS*, **471**, 447
- Stierwalt S., Liss S. E., Johnson K. E., Patton D. R., Privon G. C., Besla G., Kallivayalil N., Putman M., 2017, *Nature Astronomy*, **1**, 0025
- Sweet S. M., et al., 2013, *MNRAS*, **433**, 543
- Sweet S. M., Drinkwater M. J., Meurer G., Bekki K., Dopita M. A., Kilborn V., Nicholls D. C., 2014, *ApJ*, **782**, 35
- Sweet S. M., Drinkwater M. J., Meurer G., Kilborn V., Audcent-Ross F., Baumgardt H., Bekki K., 2016, *MNRAS*, **455**, 2508
- Tempel E., et al., 2014, *A&A*, **566**, A1
- Tovmassian H. M., Plionis M., 2009, *ApJ*, **696**, 1441
- Tully R. B., 2015, *AJ*, **149**, 171
- Verdes-Montenegro L., Yun M. S., Williams B. A., Huchtmeier W. K., Del Olmo A., Perea J., 2001, *A&A*, **377**, 812
- Verdes-Montenegro L., Sulentic J., Lisenfeld U., Leon S., Espada D., Garcia E., Sabater J., Verley S., 2005, *A&A*, **436**, 443
- Véron-Cetty M. P., Véron P., 2006, *A&A*, **455**, 773
- Wang J., Koribalski B. S., Serra P., van der Hulst T., Roychowdhury S., Kamphuis P., Chengalur J. N., 2016, arXiv.org, pp 2143–2151
- White S. D. M., Rees M. J., 1978, *MNRAS*, **183**, 341
- Williams B. A., McMahon P. M., van Gorkom J. H., 1990, in Sulentic J. W., Keel W. C., Telesco C. M., eds, NASA Conference Publication Vol. 3098, NASA Conference Publication.
- Wilson W. E., et al., 2011, *MNRAS*, **416**, 832
- Wojtak R., 2013, *A&A*, **559**, A89
- Wolfinger K., Kilborn V. A., Ryan-Weber E. V., Koribalski B. S., 2016, *Publ. Astron. Soc. Australia*, **33**, e038
- Wright E. L., et al., 2010, *AJ*, **140**, 1868
- Yang X., Mo H. J., van den Bosch F. C., Pasquali A., Li C., Barden M., 2007, *ApJ*, **671**, 153
- Yoon H., Chung A., Smith R., Jaffé Y. L., 2017, *ApJ*, **838**, 81
- Yun M. S., Ho P. T. P., Lo K. Y., 1994, *Nature*, **372**, 530
- Zabludoff A. I., Mulchaey J. S., 1998, *ApJ*, **496**, 39
- Zwaan M. A., et al., 2004, *MNRAS*, **350**, 1210
- de Carvalho R. R., Coziol R., 1999, *The Astronomical Journal*, **117**, 1657
- van Driel W., Marcum P., Gallagher III J. S., Wilcots E., Guidoux C., Monnier Ragaigne D., 2001, *A&A*, **378**, 370
- van der Velden E., 2020, *The Journal of Open Source Software*, **5**, 2004
- van der Walt S., Colbert S. C., Varoquaux G., 2011, *Computing in Science and Engineering*, **13**, 22

## APPENDIX A: PROPERTIES OF CHOIR GALAXIES AND $\Delta f_{\text{HI}}$

Our analysis was carried out by making distinction between central and satellite galaxies, marking galaxies that are obtained from the literature, as well as those that are H I-excess and H I-deficient. Therefore, in this appendix we show Choir galaxy properties and the  $\Delta f_{\text{HI}}$  (the distance of the H I mass fraction from the HIPASS running median).

In Figure A1, the relationship between galaxy R-band effective radii and the stellar mass, we find that at fixed stellar

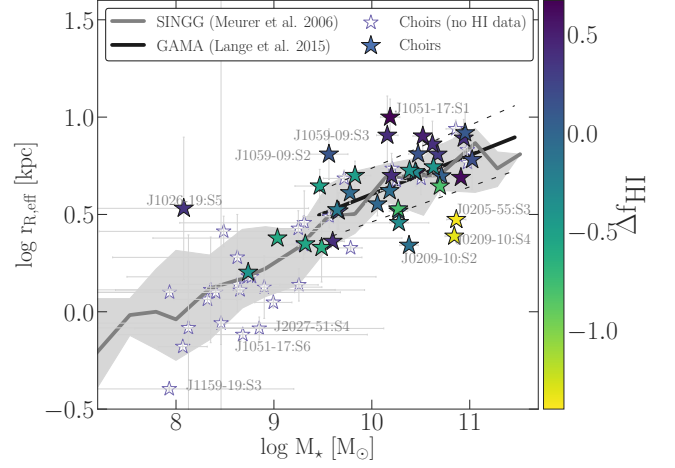


**Figure A1.** Reproduced Figure 5: Relationship between galaxy R-band effective radii and the stellar mass. Here we show  $\Delta f_{\text{HI}}$  on the colorbar.

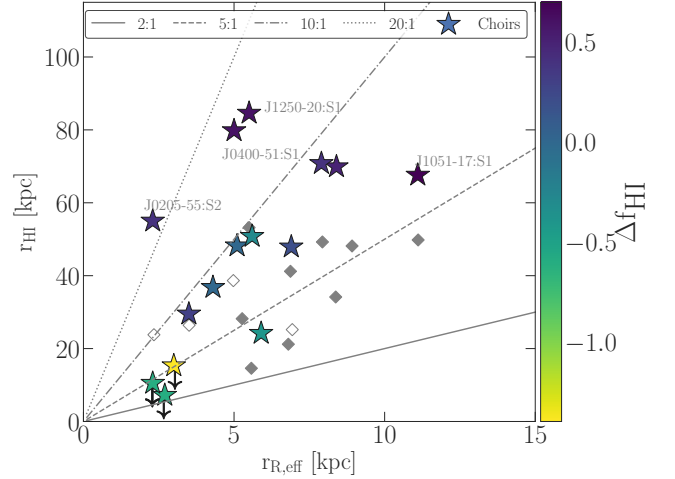


**Figure A2.** Reproduced Figure 6: Relationship between galaxy H I radii measured at  $3 \times 10^{19} \text{cm}^{-2}$  and  $R_{\text{eff}}$  radii. Here we show  $\Delta f_{\text{HI}}$  on the colorbar. The star markers show Choir galaxies. The grey diamonds show Choir galaxies with the H I-radius measured at  $1 M_{\odot} \text{pc}^{-2}$  (Džudžar et al. 2019a).

mass range  $10^{10} \leq M_{\star} M_{\odot} \leq 10^{11}$ , with the increase of the  $r_{R,\text{eff}}$  the galaxy is more H I-rich.

In Figure A2, the relationship between galaxy H I radii measured at  $3 \times 10^{19} \text{cm}^{-2}$  and  $R_{\text{eff}}$  radii, we find that the larger the  $\Delta f_{\text{HI}}$ , galaxy is more likely to have larger H I radius.

In Figure A3, *WISE* color-color diagram of the Choir galaxies, we do not find a clear relationship between *WISE* colours and  $\Delta f_{\text{HI}}$ . However, we find that galaxies with elevated W1-W2 colours with respect to the star-forming sequence have  $\Delta f_{\text{HI}} < 0$  dex.

In Figure A4, the *WISE* star formation versus stellar mass, we do not find a clear relationship with  $\Delta f_{\text{HI}}$ . J0209-10:S4 has lower specific star formation rate and its an H I-deficient, and interacting galaxy as seen in the H I and optical imaging (e.g. Jones et al. 2019).

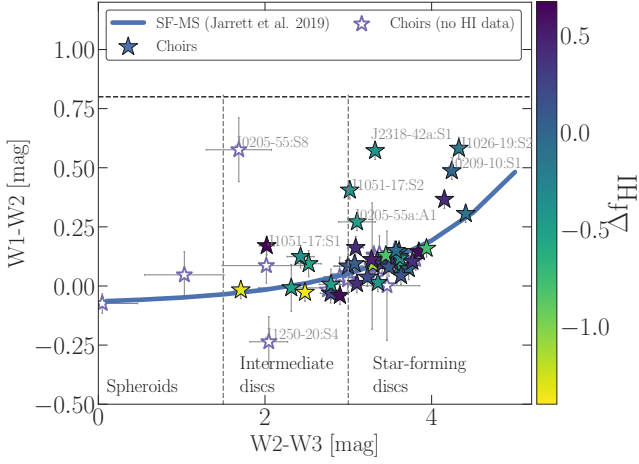


**Figure A3.** Reproduced Figure 9: *WISE* color-color diagram of the Choir galaxies. Here we show  $\Delta f_{\text{HI}}$  on the colorbar. The solid blue line shows the *WISE* colour-colour sequence (Jarrett et al. 2019).

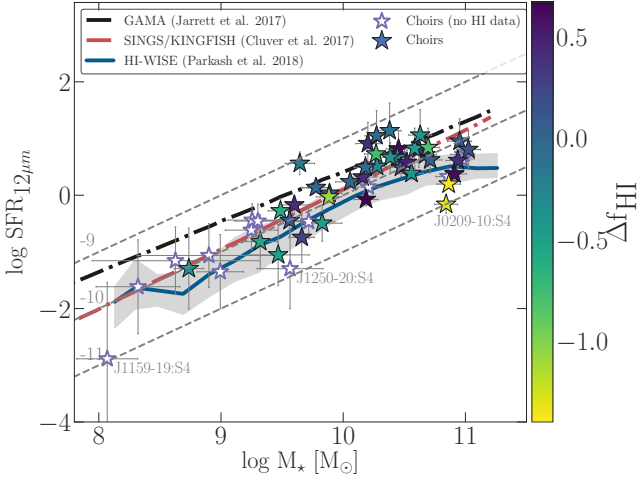


**Figure A4.** Reproduced Figure 9: The *WISE* star formation versus stellar mass. Here we show  $\Delta f_{\text{HI}}$  on the colorbar. The star markers show Choir galaxies. The horizontal dashed lines are denoting constant specific star-formation rates.

## APPENDIX B: TABLE OF GROUP PROPERTIES

We summarise properties of the Choir groups in Table B1 and here we describe how they were computed. The projected velocity dispersion of a group is derived from:

$$\sigma_{\text{group}} = \sqrt{\frac{1}{N} \sum_i^N (v_i - \langle v \rangle)^2}. \quad (\text{B1})$$

where  $N$  is number of galaxies in a group,  $v_i$  is a galaxy recessional velocity and  $\langle v_i \rangle$  is mean group velocity. Values of  $r_{200}$  and  $M_{200}$  are derived using equations from Poggianti et al. (2010):

$$r_{200} = 1.73 \frac{\sigma_{\text{group}}}{1000 \text{ km s}^{-1} \sqrt{\Omega_{\Lambda} + \Omega_0 (1+z)^3}} h_{100}^{-1} [\text{Mpc}] \quad (\text{B2})$$

and

$$M_{200} = 1.2 \left( \frac{\sigma_{\text{group}}}{1000 \text{ km s}^{-1}} \right)^3 \frac{1}{\sqrt{\Omega_{\Lambda} + \Omega_0 (1+z)^3}} h_{100}^{-1} [10^{15} M_{\odot}], \quad (\text{B3})$$

where  $\Omega_{\Lambda} = 0.7$ ;  $\Omega_0 = 0.3$ ;  $h = 0.7$ .

Crossing time is derived using equation from Konstantopoulos et al. (2010):

$$t_c = \frac{R_{\text{rms}}}{\sigma_{\text{group}}}, \quad (\text{B4})$$

where  $R_{\text{rms}}$  is the projected group radius which is derived using equation from Berlind et al. (2006):

$$R_{\text{rms}} = \sqrt{\frac{1}{N} \sum_i^N r_i^2}, \quad (\text{B5})$$

where  $r_i$  is a galaxy's projected distance from the group centroid. Due to the projected velocity dispersion (and not the three dimensional one) and the small number of galaxies, the crossing time could be a factor of two larger (Konstantopoulos et al. 2010).

Note of caution: these equations are under assumption of the virial equilibrium, which may not be established in Choir groups, thus the derived values are only approximation of these properties.

**Table B1.** Summary of the Choir groups

Group ID	RA <sub>cen</sub> J2000 [deg]	DEC <sub>cen</sub> J2000 [deg]	$\sigma_{\text{group}}$ [km s <sup>-1</sup> ]	r <sub>200</sub> [Mpc]	M <sub>200</sub> [M <sub>⊙</sub> ]	M <sub>H I</sub> [dex]	Scale [kpc/"]	R <sub>rms</sub> [kpc]	t <sub>cross</sub> [Gyr]	Comment
(1)	(2)	(3)	(4)	(5)	(6)	(7)	(8)	(9)	(10)	(11)
J0205-55	31.24005	-55.18582	221	0.54	1.83	10.51	0.439	133.2	0.60	Two subgroups merging
J0209-10	32.38124	-10.14940	86	0.21	0.11	10.31	0.258	39.7	0.46	H I mapped in Jones et al. (2019)
J0258-74	44.58151	-74.42768	94	0.23	0.14	10.41	0.333	56.7	0.60	Isolated group
J0400-52	60.22478	-52.75107	293	0.71	4.24	10.61	0.702	221.4	0.76	Cluster infalling group (Džudžar et al. 2019b)
J0443-05	70.99437	-5.35875	75*	0.18	0.07	10.41	0.328	110.5	1.47	Not mapped in H I
J1026-19	156.6397	-19.07035	9*	0.02	1.23×10 <sup>9</sup>	10.63	0.630	183.5	20.4	Tidal interactions
J1051-17	162.84646	-17.09431	250	0.61	2.66	10.45	0.393	218.3	0.87	Kilborn et al. in prep
J1059-09	164.78250	-9.81185	186	0.45	1.09	10.42	0.571	169.2	0.91	Tidal interactions
J1159-19	179.88779	-19.30826	38*	0.09	9.38×10 <sup>10</sup>	9.92	0.120	13.2	0.35	Tidal interactions; H I mapped in Phookun et al. (1992)
J1250-20	192.70101	-20.37571	60*	0.15	0.04	10.51	0.535	107.4	1.79	Isolated group; H I mapped in Džudžar et al. (2019a)
J1403-06	210.85138	-6.07759	100	0.25	0.17	10.29	0.196	35.6	0.36	H I mapped in Clemens M.S. 1998 Ph.D. Thesis
J1408-21	212.18354	-21.58828	150	0.37	0.57	10.52	0.599	152.7	1.02	Tidal interactions
J1956-50	299.02451	-50.00326	223	0.54	1.88	10.52	0.517	185.6	0.83	Isolated group
J2027-51	306.97329	-51.64226	92	0.23	0.13	10.44	0.411	141.4	1.54	Local group analogous
J2318-42a	349.71742	-42.30871	134	0.33	0.41	10.10	0.111	37.1	0.28	H I mapped in Dahlem (2005)

(1) Group name: HIPASS+Group ID; (2) Right Ascension (J2000) - for group centroid, derived as mass weighted average; (3) Declination (J2000) - for group centroid, derived as mass weighted average; (4)  $\sigma_{\text{group}}$  - Radial velocity dispersion of the group [km s<sup>-1</sup>]; (5) r<sub>200</sub> [Mpc] of the group; (6) M<sub>200</sub> × 10<sup>13</sup> [M<sub>⊙</sub>], if not otherwise specified, of the group. The r<sub>200</sub> and M<sub>200</sub> are based on equations from Poggianti et al. (2010), assuming virialized structures; (7) M<sub>H I</sub> - Logarithm of the group H I mass from Sweet et al. (2013); (8) Scale factor; (9) R<sub>rms</sub> - Projected group radius, based on Eq.8 from Berlind et al. (2006); (10) t<sub>cross</sub> - Group crossing time, based on Konstantopoulos et al. (2010); (11) A comment about group. Used equations are summarised in this Section B.

\* For J0443-05 and J1026-19 velocity dispersion is computed with three galaxies; J1159-19 and J1250-20 with two, thus they are highly uncertain.

## APPENDIX C: GALAXY PROPERTIES

In Table C1 we show Choirs which data we utilise from the literature, comparing literature values with ours. The largest difference is the distance to J1159-29 group, in which Phookun et al. (1992) adopted 10 Mpc, while our adopted distance is 25 Mpc (similar to Hubble flow).

## APPENDIX D: NEW OBSERVED CHOIRS AND DETECTIONS

Here we present the H I and stellar masses of the galaxies from new observed groups, in addition to those from our previous work in Džudžar et al. (2019a). We did not resolve individual galaxies in J1159-19, thus we are placing it in Table C1. J0205-55 in Džudžar et al. (2019a) has pre-CABB data, and here we present data with new correlator, we also have more H I detections in this group than in our previous work. J025-74:S3 galaxy is very near to S2 galaxy in this group, and in this work we have a better extraction of the H I content within this group. J2027-51:S3 and J1051-17:A3 are galaxies which H I was extracted below  $3\sigma$  level, thus we consider them only as tentative detections.

## APPENDIX E: H I DETECTION LIMIT

The H I mass limit was determined using standard relation for mass (see Equation 1) where the flux is based on the observed limit. The flux upper limit is based on the relation from Sardone et al. (2019):  $F_{\text{HI,lim}} = 3 \sigma_{\text{rms}} \sqrt{W} dv$ , where the rms is the measured noise in the data cube and  $W$  is the expected H I emission line width, we adopt it to be  $300 \text{ km s}^{-1}$ , and the  $dv$  is the velocity resolution, see Figure E1 and Figure 2 in Section 3.1. Using these data, we find the probable H I-deficient galaxy and show we them in Table E1.

## APPENDIX F: GALAXY RADII

In Table F1 we summarise the measurements of the galaxy radii from Section 3.3.

## APPENDIX G: WISE MEASUREMENTS

The mid-infrared properties of Choir galaxies are obtained using “drizzled” WISE imaging Jarrett et al. (2012). The photometry was obtained from reconstructed images from WISE using the ICORE co-addition software Masci (2013). We show the WISE measurements for Choir galaxies in Table G1. For details on the WISE measurements see Jarrett et al. (2012) and Jarrett et al. (2013).

The W3pah and W4dust are fluxes that are obtained after removing the expected (model) stellar continuum. If the continuum-subtraction from the W3 flux (measured at the  $2\sigma$  level) is below zero (or zero) we do not have measurements of the star formation rate.

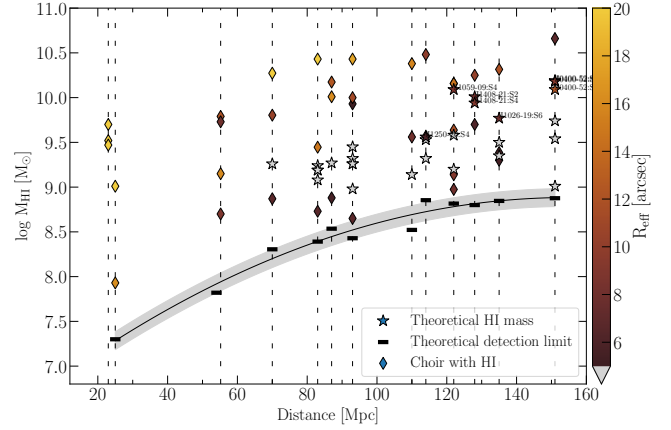


**Figure E1.** The H I mass versus the distance for Choir galaxies. The vertical dashed lines are connecting galaxies within the same Choir group. The diamonds are Choir galaxies detected in H I, and the colour shows their  $R_{\text{eff}}$  radius. The star symbols show the expected H I mass for Choir galaxies, based on the  $M_R$  to  $M_{\text{HI}}$  scaling relation (Sweet et al. 2013; Dénes et al. 2014). The grey stars are those whose  $R_{\text{eff}}$  radius is below 5 arcsec (as the smallest detected galaxy has 5.2 arcsec), and thus we consider them to be below our detection limit. The coloured stars are those that have high enough radius (and stellar mass from, see Figure 2) to be detected, thus we consider them to be H I-deficient galaxies. The black rectangles show the theoretical mass limit for each Choir group, while the curved line shows the polyfit line to those limits, with a standard deviation shown as grey shaded region.

**Table C1.** Summary of the Choir galaxies within groups that are obtained from the literature

ID	RA	DEC	D	$M_{\text{HI}}$	$D_{\text{our}}$	$M_{\text{HI,our}}$	$\Delta f_{\text{HI}} \pm \sigma$	Reference
(1)	[deg]	[deg]	[Mpc]	[dex]	[Mpc]	[dex]	[dex]	(9)
J0209-10:S1	32.4279	-10.1837	55.2	9.79	54	9.71	0.0±0.1	(Jones et al. 2019)
J0209-10:S2	32.4103	-10.1461	55.2	9.73	54	9.55	-0.1±0.1	"
J0209-10:S3	32.3518	-10.1363	55.2	9.15	54	9.13	-0.8±0.1	"
J0209-10:S4	32.3362	-10.1329	55.2	8.70	54	8.68	-1.3±0.1	"
J1159-19:S1	179.876	-19.2658	10	9.01	25	9.76	-0.8±0.1	(Phookun et al. 1992)
J1159-19:S2	179.873	-19.3332	10	7.93	25	8.68	-0.4±0.1	"
J1159-19:S3	179.899	-19.3174	10	...	25	...	...	...
J1159-19:S4	179.908	-19.3292	10	...	25	...	...	...
J2318-42a.S1	349.598	-42.3700	22	9.52	23	9.56	-0.4±0.1	(Dahlem 2005)
J2318-42a.S2	349.728	-42.2386	22	9.47	23	9.51	-0.3±0.1	"
J2318-42a.S3	349.823	-42.2620	22	9.70	23	9.74	-0.1±0.1	"
J2318-42a.S4	349.7098	-42.3968	22	...	23	...	...	...

(1) ID: Galaxy ID; (2) Right Ascension (J2000); (3) Declination (J2000); (4) Distance used in the literature; (5) Mass used in the literature; (6) Distance used in this work; (7) Mass used in this work; (8) Distance of the H I mass fraction from the HIPASS running median line; (9) Reference.

**Table D1.** Summary of the Choir galaxies from new observations and new detections

ID	RA	DEC	D	$M_{\text{HI}}$	$M_{\star}$	Comment
(1)	[deg]	[deg]	[Mpc]	[dex]	[dex]	(7)
J0205-55:S1	31.27286	-55.11182	93	10.43 ± 0.10	10.94 ± 0.10	Data from new CABB observations
J0205-55:S2	31.21211	-55.217130	93	9.93 ± 0.10	9.60 ± 0.12	"
J0205-55:S3	31.14558	-55.119310	93	8.65 ± 0.13	10.86 ± 0.10	"
J0205-55:S4	31.08276	-55.230710	93	10.0 ± 0.10	10.71 ± 0.10	"
J0205-55:A1	31.51224	-55.194627	93	9.43 ± 0.10	10.59 ± 0.10	"
J1956-50:S1	299.19006	-50.05563	110	10.38 ± 0.10	10.52 ± 0.10	"
J1956-50:S2	298.97214	-50.036330	110	9.56 ± 0.10	9.78 ± 0.12	"
J1956-50:A1	298.88959	-49.882370	110	9.75 ± 0.13	9.89 ± 0.10	"
J0258-74:S3	44.677720	-74.434310	70	8.87 ± 0.20	9.49± 0.10	New extraction of the H I
J2027-51:S3	306.952240	-51.738960	87	8.88 ± 0.13	9.32 ± 0.14	Tentative detection, below 3 $\sigma$
J1051-17:A3	162.632092	-17.064126	83	8.54 ± 0.10	9.88± 0.10	"

(1) ID: Galaxy ID; (2) Right Ascension (J2000); (3) Declination (J2000); (4) Group distance; (5) H I mass and its uncertainty; (6) Stellar mass from the *WISE*; (7) Comment about the galaxy.

**Table E1.** H I-deficient galaxies determined from our H I non-detection analysis

ID	RA	DEC	$M_{\text{HI,exp}}$	$M_{\text{lim}}$	Def
(1)	[deg]	[deg]	[dex]	[dex]	[dex]
J1026-19:S6	156.605	-19.17649	9.8	8.8	1
J1059-09:S4	164.69545	-9.84515	10.2	8.8	1.3
J1250-20:S4	192.66643	-20.34798	9.6	8.9	0.7
J1408-21:S2	212.24107	-21.64791	10	8.7	1.3
J1408-21:S4	212.17101	-21.628	9.9	8.7	1.2
J0400-52:S4	60.32599	-52.70749	10.2	8.9	1.3
J0400-52:S5	60.22048	-52.82712	10.2	8.9	1.3
J0400-52:S6	60.32479	-52.80079	10.1	8.9	1.2

(1) ID: Galaxy ID; (2) Right Ascension (J2000); (3) Declination (J2000); (4)  $M_{\text{HI,exp}}$  - The logarithm of galaxy's expected H I mass, based on the  $M_{\text{R}}$  to  $M_{\text{HI}}$  scaling relation (Sweet et al. 2013; Dénes et al. 2014); (5)  $M_{\text{HI,lim}}$  - The logarithm of the theoretical limit for the observed H I mass; (6) Def - The H I deficiency, obtained as the difference between the expected H I mass and the limit H I mass.

**Table F1.** Measurements of galaxy radii

Optical ID	Our ID	$\Delta f_{\text{HI}} \pm \sigma$	$r_{\text{HI}}$	$D_{\text{HI}}$	$r_{\text{R,eff}}^{\text{b}}$	H I content
(1)	(2)	[dex]	[kpc]	[kpc]	[kpc]	(9)
PGC032573	J1051-17:S1	0.7±0.1	67.6	99.6	11.1	H I-excess
ESO156-G029	J0400-52:S1	0.6±0.1	79.8	77.3	5.0	H I-excess
ESO575-G006	J1250-20:S1	0.6±0.1	84.6	106.4	5.5	H I-excess
IC4909	J1956-50:S1	0.5±0.1	69.9	68.3 <sup>a</sup>	8.4	H I-excess
GALEXASC J202808.43-512830.5	J2027-51:A1 <sup>d</sup>	0.4±1.3	...	25.9	...	H I-average
MCG-01-28-012	J1059-09:S3	0.4±0.1	...	...	8.7	"
ESO234-G032	J2027-51:S1	0.4±0.1	...	56.4	5.3	"
ESO 153-IG 016	J0205-55:S2	0.4±0.1	55.0	47.6	2.3	"
ESO568-G011	J1026-19:S1	0.4±0.1	...	...	7.8	"
ESO153-G017	J0205-55:S1	0.4±0.1	70.8	98.5	7.9	"
WISEA J102641.63-190742.0	J1026-19:S5 <sup>d</sup>	0.4±1.3	...	...	3.7	"
ESO031-G005	J0258-74:S1	0.3±0.1	47.9	82.4	6.9	"
GALEXASCJ025852.12-742554.8	J0258-74:S2	0.3±0.1	29.5	52.8	3.5	"
GALEXASCJ140846.58-212708.8	J1408-21:A1 <sup>d</sup>	0.2±1.3	...	...	...	"
ESO578-G026	J1408-21:S1	0.2±0.1	...	...	6.4	"
ESO234-G028	J2027-51:S2	0.1±0.1	...	42.4	6.8	"
GALEXASC J105906.72-094506.7	J1059-09:S2	0.1±0.1	...	50.4	6.9	"
ESO233-G007	J1956-50:A1	0.1±0.1	42.7	...	...	"
MCG-01-28-013	J1059-09:S1	0.1±0.1	...	96.3	8.9	"
ESO153-G013	J0205-55:S4	0.0±0.1	48.2	...	5.1	"
GALEXASCJ140841.07-213741.5	J1408-21:S3	0.0±0.1	...	...	3.8	"
2MASSX J19555339-5002124	J1956-50:S2	0.0±0.1	36.8	...	4.3	"
2MASX J10265008-1904310	J1026-19:S2	-0.2±0.1	...	...	3.6	"
WISEA J105049.71-171411.2	J1051-17:A2 <sup>d</sup>	-0.3±1.3	9.3 <sup>c</sup>	...	...	"
ESO575-G004	J1250-20:S2	-0.3±0.1	50.8	29.2	5.6	"
NGC3431	J1051-17:S2	-0.4±0.1	24.9	...	5.9	"
MGC-03-28-016	J1051-17:A1	-0.4±0.1	...	...	...	"
GALEXASC J105930.89-094425.7	J1059-09:S5	-0.5±0.2	...	...	5.4	"
GALEXASC J105908.60-094312.8	J1059-09:S6	-0.5±0.3	...	...	4.8	"
WISEA J105135.87-165919.3	J1051-17:S3 <sup>d</sup>	-0.6±1.3	7.2 <sup>c</sup>	...	2.7	"
ESO153-G020	J0205-55:A1	-0.5±0.1	29.3	...	...	H I-deficient
2MASS J20274857-5144205	J2027-51:S3 <sup>e</sup>	-0.6±0.1	...	...	2.3	H I-deficient
GALEXASCJ02584292-7426028	J0258-74:S3	-0.6±0.1	10.5 <sup>c</sup>	...	2.3	H I-deficient
MCG -03-28-013	J1051-17:A3 <sup>e</sup>	-1.1±0.1	...	...	...	H I-deficient
ESO153-G015	J0205-55:S3	-1.4±0.1	15.3 <sup>c</sup>	...	3.0	H I-deficient

(1) Optical ID: Galaxy ID from NED; (2) Our ID: HIPASS+Group+Galaxy identification; (3)  $\Delta f_{\text{HI}}$ : Distance of the H I mass fraction from the HIPASS running median line; (4)  $r_{\text{HI}}$ : H I radius measured at the H I column density of  $3 \times 10^{19} \text{ cm}^{-2}$ ; (5)  $D_{\text{HI}}$ : H I diameter, measured at at  $1 \text{ M}_{\odot} \text{ pc}^{-2}$  (Džudžar et al. 2019a); (6)  $r_{\text{R,eff}}$ : R-band effective radius from SINGG; (7) H I content: classification based on  $\Delta \log(f_{\text{HI}})$  into H I-excess, H I-average or H I-deficient galaxy.

<sup>a</sup> Measured in this work, following Džudžar et al. (2019a) procedure.

<sup>b</sup> From the SINGG survey (Meurer et al. 2006).

<sup>c</sup> Upper limits on the H I-radius, as described in Section 3.3.

<sup>d</sup> Has highly uncertain stellar mass ( $\sim 1.3$  dex).

<sup>e</sup> The H I emission in galaxies is detected below  $3\sigma$ .

**Comments:**

i) The first three galaxies are highlighted in Figure 8 as most H I-excess, while the bottom three are highlighted in Figure 7 as most H I-deficient; excluding J1051-17:A3 and J2027-51:S3 since their H I mass is measured at  $2\sigma$ . ii) We do not include  $r_{\text{HI}}$  for galaxies in the following groups because the lowest H I-column density is higher than the  $3 \times 10^{19} \text{ cm}^{-2}$ : J1026-19, J1059-09, J1408-21 and J2027-51.

**Table G1.** *WISE* measurements of Choir members and their H I mass

ID	RA	DEC	D	W1	W2	W3pah	W4dust	(W1-W2) $\pm \sigma$	(W2-W3) $\pm \sigma$	M $_{\star} \pm \sigma$	SFR $_{12} \pm \sigma$	M $_{\text{H I}} \pm \sigma$
(1)	[deg]	[deg]	[Mpc]	[mJy]	[mJy]	[mJy]	[mJy]	[mag]	[mag]	[dex]	[M $_{\odot} \text{ yr}^{-1}$ ]	[dex]
J0205-55:S1	31.27286	-55.11182	93	24.722	13.752	36.888	58.294	0.01 $\pm$ 0.039	3.103 $\pm$ 0.055	10.94 $\pm$ 0.10	4.10 $\pm$ 1.43	10.43 $\pm$ 0.10 <sup>a</sup>
J0205-55:S2	31.21211	-55.21713	93	2.753	1.761	4.723	11.720	0.162 $\pm$ 0.047	3.089 $\pm$ 0.094	9.60 $\pm$ 0.12	0.67 $\pm$ 0.24	9.93 $\pm$ 0.12 <sup>a</sup>
J0205-55:S3	31.14558	-55.11931	93	16.712	8.987	12.383	11.422	-0.027 $\pm$ 0.038	2.48 $\pm$ 0.055	10.86 $\pm$ 0.10	1.57 $\pm$ 0.55	8.65 $\pm$ 0.13 <sup>a</sup>
J0205-55:S4	31.08276	-55.23071	93	23.964	14.403	37.868	53.625	0.094 $\pm$ 0.037	3.076 $\pm$ 0.04	10.71 $\pm$ 0.10	4.20 $\pm$ 1.45	10.0 $\pm$ 0.1 <sup>a</sup>
J0205-55:S5	31.22966	-55.14355	93	0.093	0.057	...	...	0.11 $\pm$ 0.226	...	8.49 $\pm$ 1.27	...	...
J0205-55:S6	31.23776	-55.22611	93	0.438	0.261	0.216	...	0.086 $\pm$ 0.074	2.016 $\pm$ 0.529	8.99 $\pm$ 0.19	0.04 $\pm$ 0.02	...
J0205-55:S7	31.34851	-55.23729	93	0.041	0.034	...	...	0.47 $\pm$ 0.228	...	8.13 $\pm$ 1.27	...	...
J0205-55:S8	31.12363	-55.2156	93	0.181	0.170	0.108	...	0.576 $\pm$ 0.135	1.686 $\pm$ 0.392	8.32 $\pm$ 0.34	0.02 $\pm$ 0.01	...
J0205-55:A1	31.51664	-55.19627	93	33.180	23.475	64.485	159.368	0.271 $\pm$ 0.037	3.104 $\pm$ 0.22	10.59 $\pm$ 0.10	6.70 $\pm$ 2.60	9.43 $\pm$ 0.10 <sup>a</sup>
J0209-10:S1	32.42817	-10.18376	54	47.941	41.366	342.754	1805.609	0.487 $\pm$ 0.037	4.242 $\pm$ 0.038	10.27 $\pm$ 0.10	11.19 $\pm$ 3.88	9.71 <sup>b</sup>
J0209-10:S2	32.41058	-10.14634	54	61.337	44.820	432.838	1418.895	0.306 $\pm$ 0.037	4.409 $\pm$ 0.038	10.38 $\pm$ 0.10	13.74 $\pm$ 4.76	9.55 <sup>b</sup>
J0209-10:S3	32.35258	-10.13578	54	83.744	51.983	199.119	403.120	0.129 $\pm$ 0.037	3.45 $\pm$ 0.038	10.70 $\pm$ 0.09	6.94 $\pm$ 2.40	9.13 <sup>b</sup>
J0209-10:S4	32.33679	-10.13312	54	50.069	27.167	14.437	24.159	-0.017 $\pm$ 0.037	1.71 $\pm$ 0.079	10.84 $\pm$ 0.10	0.69 $\pm$ 0.24	8.68 <sup>b</sup>
J0258-74:S1	44.52795	-74.45632	70	38.541	23.165	84.705	122.573	0.094 $\pm$ 0.036	3.406 $\pm$ 0.038	10.67 $\pm$ 0.09	5.17 $\pm$ 1.79	10.27 $\pm$ 0.03 <sup>c</sup>
J0258-74:S2	44.71847	-74.43176	70	1.809	0.969	1.864	3.128	-0.031 $\pm$ 0.041	2.788 $\pm$ 0.125	9.66 $\pm$ 0.11	0.18 $\pm$ 0.06	9.8 $\pm$ 0.1 <sup>c</sup>
J0258-74:S3	44.67772	-74.43431	70	2.379	1.417	6.357	9.928	0.085 $\pm$ 0.04	3.614 $\pm$ 0.051	9.49 $\pm$ 0.10	0.53 $\pm$ 0.18	8.87 $\pm$ 0.2 <sup>a</sup>
J0258-74:S4	44.37181	-74.37624	70	0.121	0.097	...	...	0.406 $\pm$ 0.142	...	8.35 $\pm$ 1.27	...	...
J0400-52:S1	60.17053	-52.73405	151	6.546	3.478	7.514	8.362	-0.04 $\pm$ 0.039	2.899 $\pm$ 0.065	10.91 $\pm$ 0.10	2.37 $\pm$ 0.83	10.66 $\pm$ 0.09 <sup>c</sup>
J0400-52:S2	60.20074	-52.68383	151	0.010	0.009	...	...	0.485 $\pm$ 0.884	...	7.93 $\pm$ 1.28	...	...
J0400-52:S3	60.02511	-52.65909	151	1.188	0.726	3.937	4.324	0.112 $\pm$ 0.046	3.809 $\pm$ 0.064	9.78 $\pm$ 0.12	1.35 $\pm$ 0.47	...
J0400-52:S4	60.32599	-52.70749	151	13.128	7.591	18.515	25.185	0.052 $\pm$ 0.038	3.006 $\pm$ 0.045	10.98 $\pm$ 0.10	5.25 $\pm$ 1.82	...
J0400-52:S5	60.22048	-52.82712	151	11.142	6.288	15.075	23.084	0.026 $\pm$ 0.039	2.992 $\pm$ 0.042	10.98 $\pm$ 0.10	4.38 $\pm$ 1.52	...
J0400-52:S6	60.32479	-52.80079	151	6.622	3.592	6.654	9.859	-0.017 $\pm$ 0.039	2.75 $\pm$ 0.058	10.86 $\pm$ 0.10	2.13 $\pm$ 0.74	...
J0400-52:S7	60.28706	-52.82552	151	0.288	0.171	0.560	...	0.08 $\pm$ 0.084	3.296 $\pm$ 0.339	9.25 $\pm$ 0.21	0.24 $\pm$ 0.11	...
J1026-19:S1	156.67012	-19.05137	135	9.704	5.883	30.689	49.012	0.104 $\pm$ 0.039	3.769 $\pm$ 0.043	10.62 $\pm$ 0.10	6.72 $\pm$ 2.33	10.3 $\pm$ 0.1 <sup>c</sup>
J1026-19:S2	156.70862	-19.07548	135	1.807	1.702	15.305	60.496	0.582 $\pm$ 0.047	4.327 $\pm$ 0.057	9.65 $\pm$ 0.12	3.64 $\pm$ 1.27	9.4 $\pm$ 0.1 <sup>c</sup>
J1026-19:S3	156.57893	-18.96424	135	0.292	0.160	...	...	-0.007 $\pm$ 0.127	...	9.31 $\pm$ 1.27	...	...
J1026-19:S4	156.6017	-19.03421	135	0.102	0.056	0.217	...	0.001 $\pm$ 0.231	3.464 $\pm$ 0.393	8.90 $\pm$ 0.59	0.09 $\pm$ 0.04	...
J1026-19:S5	156.67381	-19.12782	135	0.017	0.014	...	...	0.399 $\pm$ 0.72	...	8.08 $\pm$ 1.28	...	9.3 $\pm$ 0.1 <sup>c</sup>
J1026-19:S6	156.605	-19.17649	135	0.836	0.478	1.040	3.031	0.039 $\pm$ 0.083	2.897 $\pm$ 0.187	9.72 $\pm$ 0.21	0.34 $\pm$ 0.13	...
J1051-17:S1	162.90611	-17.12477	83	13.983	9.013	7.660	13.094	0.17 $\pm$ 0.039	2.021 $\pm$ 0.089	10.19 $\pm$ 0.10	0.84 $\pm$ 0.30	10.43 $\pm$ 0.02 <sup>c</sup>
J1051-17:S2	162.81264	-17.00815	83	26.310	21.056	53.591	121.628	0.405 $\pm$ 0.037	3.018 $\pm$ 0.04	10.39 $\pm$ 0.10	4.66 $\pm$ 1.61	9.45 $\pm$ 0.05 <sup>c</sup>
J1051-17:S3	162.89915	-16.98857	83	0.412	0.244	...	...	0.08 $\pm$ 0.12	...	9.04 $\pm$ 1.27	...	8.73 $\pm$ 0.07 <sup>c</sup>
J1051-17:S4	162.85841	-17.08458	83	0.097	0.032	...	...	-0.554 $\pm$ 0.655	...	8.41 $\pm$ 1.27	...	...
J1051-17:S5	162.9621	-16.97549	83	0.171	0.101	...	...	0.078 $\pm$ 0.188	...	8.65 $\pm$ 1.27	...	...
J1051-17:S6	162.9283	-17.1096	83	0.183	0.093	...	...	-0.089 $\pm$ 0.196	...	8.68 $\pm$ 1.27	...	...
J1051-17:S7	162.88902	-17.14346	83	0.224	0.124	...	...	0.005 $\pm$ 0.152	...	8.77 $\pm$ 1.27	...	...
J1051-17:S8	162.85745	-17.13794	83	0.725	0.394	...	...	-0.016 $\pm$ 0.064	...	9.28 $\pm$ 1.27	...	...
J1051-17:A1	163.06651	-17.13014	83	13.189	7.360	25.448	32.342	0.014 $\pm$ 0.038	3.355 $\pm$ 0.058	10.56 $\pm$ 0.10	2.42 $\pm$ 0.84	9.48 $\pm$ 0.03 <sup>c</sup>
J1051-17:A2	162.70667	-17.23528	83	0.317	0.176	...	...	0.012 $\pm$ 0.13	...	8.92 $\pm$ 1.27	...	9.01 $\pm$ 0.03 <sup>c</sup>
J1051-17:A3	162.6321	-17.06358	83	4.392	2.633	8.635	19.437	0.092 $\pm$ 0.041	3.296 $\pm$ 0.059	9.88 $\pm$ 0.10	0.94 $\pm$ 0.33	8.54 $\pm$ 0.10 <sup>a</sup>

(1) ID: HIPASS+Group+Galaxy identification, S – within SINGG, A – additional galaxy, discovered in H I-emission; (2) Right Ascension (J2000); (3) Declination (J2000); (4) Distance; (5) and (6) are W1 and W2 fluxes; (7) and (8) W3pah and W4dust are fluxes of the ISM emission after removing the expected (model) stellar continuum; (9) The W1-W2 colour; (10) The W2-W3 colour; (11) Logarithm of the stellar mass; (12) 12 $\mu$ m star formation rate; (13) Logarithm of the H I mass.

<sup>a</sup> H I data from this work.

<sup>b</sup> H I data obtained from the literature: J2318-42a (Dahlem 2005), J1159-19 (Phookun et al. 1992) and J0209-10 (Jones et al. 2019).

<sup>c</sup> H I data obtained from our previous work, from Džudžar et al. (2019a).

**Table G1** – *continued WISE* measurements of Choir members

ID	RA	DEC	D	W1	W2	W3pah	W4dust	(W1-W2) $\pm\sigma$	(W2-W3) $\pm\sigma$	M $_{\star}\pm\sigma$	SFR $_{12}\pm\sigma$	M $_{\text{HI}}\pm\sigma$
(1)	[deg]	[deg]	[Mpc]	[mJy]	[mJy]	[mJy]	[mJy]	[mag]	[mag]	[dex]	[M $_{\odot}\text{yr}^{-1}$ ]	[dex]
(1)	(2)	(3)	(4)	(5)	(6)	(7)	(8)	(9)	(10)	(11)	(12)	(13)
J1059-09:S1	164.81769	-9.79417	122	22.226	13.180	52.149	77.593	0.08 $\pm$ 0.039	3.487 $\pm$ 0.044	10.95 $\pm$ 0.10	8.96 $\pm$ 3.11	10.16 $\pm$ 0.10 <sup>c</sup>
J1059-09:S2	164.77763	-9.75148	122	0.926	0.551	1.337	2.290	0.084 $\pm$ 0.076	2.997 $\pm$ 0.169	9.56 $\pm$ 0.19	0.36 $\pm$ 0.13	9.6 $\pm$ 0.1 <sup>c</sup>
J1059-09:S3	164.81587	-9.81705	122	3.973	2.397	9.955	17.688	0.098 $\pm$ 0.043	3.535 $\pm$ 0.065	10.16 $\pm$ 0.11	2.09 $\pm$ 0.73	10.2 $\pm$ 0.1 <sup>c</sup>
J1059-09:S4	164.69545	-9.84515	122	10.664	6.633	22.095	50.761	0.131 $\pm$ 0.039	3.309 $\pm$ 0.053	10.50 $\pm$ 0.10	4.21 $\pm$ 1.46	...
J1059-09:S5	164.87964	-9.74003	122	1.095	0.608	1.181	2.013	0.007 $\pm$ 0.064	2.792 $\pm$ 0.142	9.83 $\pm$ 0.16	0.32 $\pm$ 0.12	9.1 $\pm$ 0.1 <sup>c</sup>
J1059-09:S6	164.78612	-9.71987	122	0.435	0.238	0.273	-1.985	-0.008 $\pm$ 0.099	2.315 $\pm$ 0.392	9.47 $\pm$ 0.25	0.09 $\pm$ 0.04	8.9 $\pm$ 0.1 <sup>c</sup>
J1059-09:S7	164.83879	-9.79738	122	0.615	0.384	1.362	3.027	0.135 $\pm$ 0.077	3.373 $\pm$ 0.152	9.26 $\pm$ 0.20	0.36 $\pm$ 0.13	...
J1059-09:S8	164.7572	-9.87943	122	0.074	0.041	...	...	0.008 $\pm$ 0.437	...	8.63 $\pm$ 1.27	...	...
J1059-09:S9	164.6862	-9.89128	122	0.047	0.022	...	...	-0.18 $\pm$ 0.509	...	8.43 $\pm$ 1.27	...	...
J1059-09:S10	164.76097	-9.88889	122	3.606	1.856	...	...	-0.074 $\pm$ 0.041	0.047 $\pm$ 0.425	10.49 $\pm$ 0.11	...	...
J1159-19:S1	179.87596	-19.26519	25	174.993	111.692	687.798	1177.216	0.159 $\pm$ 0.037	3.939 $\pm$ 0.04	10.27 $\pm$ 0.10	5.33 $\pm$ 1.85	9.76 <sup>b</sup>
J1159-19:S2	179.87216	-19.331	25	4.178	2.580	3.445	5.929	0.124 $\pm$ 0.048	2.427 $\pm$ 0.162	8.74 $\pm$ 0.12	0.05 $\pm$ 0.02	8.68 <sup>b</sup>
J1159-19:S3	179.89937	-19.31749	25	0.357	0.171	...	...	-0.152 $\pm$ 0.174	...	7.93 $\pm$ 1.27	...	...
J1159-19:S4	179.90811	-19.32914	25	0.573	0.330	0.055	...	0.047 $\pm$ 0.098	1.032 $\pm$ 0.476	8.07 $\pm$ 0.25	0.0013 $\pm$ 0.001	...
J1250-20:S1	192.72018	-20.37128	114	11.791	7.423	41.787	64.010	0.145 $\pm$ 0.039	3.846 $\pm$ 0.046	10.45 $\pm$ 0.10	6.54 $\pm$ 2.27	10.48 $\pm$ 0.09 <sup>c</sup>
J1250-20:S2	192.67047	-20.33507	114	10.310	6.375	28.482	63.978	0.125 $\pm$ 0.039	3.608 $\pm$ 0.042	10.44 $\pm$ 0.10	4.67 $\pm$ 1.62	9.6 $\pm$ 0.1 <sup>c</sup>
J1250-20:S3	192.70738	-20.36734	114	0.577	0.343	1.489	5.659	0.082 $\pm$ 0.074	3.582 $\pm$ 0.14	9.30 $\pm$ 0.19	0.35 $\pm$ 0.13	...
J1250-20:S4	192.66643	-20.34798	114	0.489	0.217	0.165	...	-0.236 $\pm$ 0.106	2.046 $\pm$ 0.227	9.57 $\pm$ 0.27	0.05 $\pm$ 0.02	...
J1250-20:S5	192.74641	-20.47055	114	0.124	0.074	0.239	...	0.084 $\pm$ 0.267	3.286 $\pm$ 0.449	8.63 $\pm$ 0.68	0.07 $\pm$ 0.03	...
J1408-21:S1	212.17491	-21.59719	128	18.599	10.605	32.353	46.150	0.037 $\pm$ 0.039	3.228 $\pm$ 0.052	11.03 $\pm$ 0.10	6.41 $\pm$ 2.23	10.25 $\pm$ 0.22 <sup>c</sup>
J1408-21:S2	212.24107	-21.64791	128	5.974	3.773	16.022	25.289	0.148 $\pm$ 0.042	3.555 $\pm$ 0.048	10.25 $\pm$ 0.11	3.45 $\pm$ 1.20	9.7 $\pm$ 0.1 <sup>c</sup>
J1408-21:S3	212.17101	-21.628	128	2.467	1.454	7.254	5.565	0.073 $\pm$ 0.047	3.725 $\pm$ 0.06	10.06 $\pm$ 0.12	1.72 $\pm$ 0.60	...
J1408-21:S4	212.13867	-21.60202	128	2.925	1.677	5.741	6.087	0.043 $\pm$ 0.045	3.343 $\pm$ 0.075	10.21 $\pm$ 0.12	1.40 $\pm$ 0.49	...
J1408-21:A1	212.19417	-21.45222	128	0.191	0.104	...	...	-0.012 $\pm$ 0.157	...	9.08 $\pm$ 1.27	...	9.5 $\pm$ 0.2 <sup>c</sup>
J1956-50:S1	299.19006	-50.05563	110	12.247	7.484	24.142	44.917	0.112 $\pm$ 0.039	3.278 $\pm$ 0.05	10.52 $\pm$ 0.10	3.80 $\pm$ 1.32	10.38 $\pm$ 0.10 <sup>a</sup>
J1956-50:S2	298.97214	-50.03633	110	2.685	1.692	7.575	14.167	0.146 $\pm$ 0.045	3.609 $\pm$ 0.057	9.78 $\pm$ 0.12	1.37 $\pm$ 0.48	9.56 $\pm$ 0.10 <sup>a</sup>
J1956-50:S3	299.03409	-50.03929	110	0.062	0.033	...	2.498	-0.044 $\pm$ 0.303	...	8.46 $\pm$ 1.27	...	...
J1956-50:A1	298.88959	-49.88237	110	2.751	1.672	5.784	9.758	0.106 $\pm$ 0.04	3.349 $\pm$ 0.064	9.89 $\pm$ 0.10	1.08 $\pm$ 0.38	9.75 $\pm$ 0.13 <sup>a</sup>
J2027-51:S1	307.02701	-51.6916	87	15.698	12.118	92.091	374.980	0.366 $\pm$ 0.038	4.153 $\pm$ 0.039	10.20 $\pm$ 0.10	8.15 $\pm$ 2.82	10.2 $\pm$ 0.1 <sup>c</sup>
J2027-51:S2	306.88406	-51.65551	87	11.789	6.766	30.820	53.893	0.044 $\pm$ 0.038	3.632 $\pm$ 0.044	10.47 $\pm$ 0.10	3.11 $\pm$ 1.08	10.0 $\pm$ 0.1 <sup>c</sup>
J2027-51:S3	306.95224	-51.73896	87	1.115	0.671	0.991	...	0.094 $\pm$ 0.055	2.524 $\pm$ 0.152	9.32 $\pm$ 0.14	0.15 $\pm$ 0.06	8.88 $\pm$ 0.13 <sup>a</sup>
J2027-51:S4	306.97769	-51.6349	87	0.244	0.145	...	...	0.079 $\pm$ 0.108	...	8.85 $\pm$ 1.27	...	...
J2027-51:A1	307.03687	-51.47511	87	0.087	0.054	...	...	0.129 $\pm$ 0.118	...	8.40 $\pm$ 1.27	...	9.49 $\pm$ 0.13 <sup>c</sup>
J2318-42a.S1	349.59833	-42.3704	23	600.930	561.039	1941.192	6602.433	0.572 $\pm$ 0.037	3.322 $\pm$ 0.037	10.63 $\pm$ 0.09	11.47 $\pm$ 3.97	9.56 <sup>b</sup>
J2318-42a.S2	349.72839	-42.23901	23	164.991	101.376	458.249	725.787	0.118 $\pm$ 0.037	3.62 $\pm$ 0.038	10.28 $\pm$ 0.10	3.23 $\pm$ 1.12	9.51 <sup>b</sup>
J2318-42a.S3	349.83566	-42.25764	23	160.482	101.586	438.978	640.655	0.15 $\pm$ 0.037	3.572 $\pm$ 0.217	10.18 $\pm$ 0.09	3.11 $\pm$ 1.20	9.74 <sup>b</sup>
J2318-42a.S4	349.70981	-42.39675	23	0.027	0.016	...	...	0.08 $\pm$ 0.308	...	6.73 $\pm$ 1.27	...	...

(1) ID: HIPASS+Group+Galaxy identification, S – within SINGG, A – additional galaxy, discovered in H I-emission; (2) Right Ascension (J2000); (3) Declination (J2000); (4) Distance; (5) and (6) are W1 and W2 fluxes; (7) and (8) W3pah and W4dust are fluxes of the ISM emission after removing the expected (model) stellar continuum; (9) The W1-W2 colour; (10) The W2-W3 colour; (11) Logarithm of the stellar mass; (12) 12 $\mu$ m star formation rate; (13) Logarithm of the H I mass.

<sup>a</sup> H I data from this work.

<sup>b</sup> H I data obtained from the literature: J2318-42a (Dahlem 2005), J1159-19 (Phookun et al. 1992) and J0209-10 (Jones et al. 2019).

<sup>c</sup> H I data obtained from our previous work, from Džudžar et al. (2019a).

## APPENDIX H: NOTE ON INDIVIDUAL CHOIR GROUPS

This section and the next one are presented as supplementary online material in the accepted paper version. Here we present results of each Choir group individually whose H I content we mapped. Based on [Verdes-Montenegro et al. \(2001\)](#) classification, we place the H I phase class for each Choir group in Table H1. Moreover, we present our Figures of each group with their H I content and their environment.

### H1 HIPASS J0205-55

Group HIPASS J0205-55 is composed of two subgroups (HIPASS J0205-55a and HIPASS J0205-55b) and it is thought that they are merging based on their recessional velocities ([Sweet et al. 2013](#)). The SINGG survey covered nine galaxies within this field. These galaxies are in the velocity range between  $5758 \text{ km s}^{-1}$  and  $6490 \text{ km s}^{-1}$  and R-band absolute magnitudes between  $-15.37 \text{ mag}$  and  $-22.57 \text{ mag}$  ([Sweet et al. 2013, 2014](#)). With the ATCA we resolved the H I content of five galaxies: S1, S2, S3, S4 and one new galaxy (A1) which is not covered in the SINGG field of view. The H I emission, velocity field and the H I spectra are shown in Figure II. S5, a dwarf galaxy is embedded within the S1 H I envelope and it is not resolved individually in our observations. S6, a dwarf galaxy, is within the S2 H I envelope. Galaxies: S7, S8 and S9 are small compact dwarf galaxies are not detected in the H I emission.

We examined the local environment of J0205-55 field within the radius of  $100'$  centered on the S1 galaxy and in the velocity range between  $4600$  and  $7600 \text{ km s}^{-1}$ . J0205-55 appears to be within  $1\text{--}1.5 \text{ Mpc}$  in the projected distance from the Low-density-contrast group LDCE122 ([Crook et al. 2007](#)) and galaxy pair ESO153-IG004 ([Tully 2015](#)) towards south-west (see panel c and d in Figure II). The nearby group LDCE122 has the same recessional velocity as the J0205-55b group and it is positioned on the J0205-55 caustics curves (see Appendix I description). These lines are computed using  $M_{200}$ , where  $M_{200}$  is determined based on the radial velocity dispersion using equation of [Poggianti et al. \(2010\)](#) and it is  $1.8 \times 10^{13} M_{\odot}$  (see Appendix B).

### H2 HIPASS J0258-74

Group HIPASS J0258-74 (hereafter, J0258-74) contains four known galaxy members, three of which we detected in H I (see Figure I2). The galaxy without an H I detection is S4 and it is a small dwarf irregular galaxy. S3 galaxy is an edge-on galaxy and it is one of the most deficient galaxies in our sample. We have shown its H I distribution in Figure 7. The H I is offset from its optical centre and due to proximity to S2 galaxy, it is possible that they are interacting.

J0258-74 is the most isolated group of galaxies in our sample, it is considered being in a void (see Section 4.2). The closest known neighbouring galaxy to J0258-74 group is a small, edge-on, late-type galaxy 2MASX J02463321-7341405 with a projected separation of around  $66 \text{ arcmin}$  which corresponds to  $\sim 1.3 \text{ Mpc}$  at the group distance of  $70 \text{ Mpc}$ . The next closest galaxy in projected separation from S1 is ESO031-G013 ( $\sim 80 \text{ arcmin}$ ) however, this galaxy is at a much larger systemic velocity of  $\sim 6400 \text{ km s}^{-1}$  with respect to the groups systemic velocity of  $4805 \text{ km s}^{-1}$ .

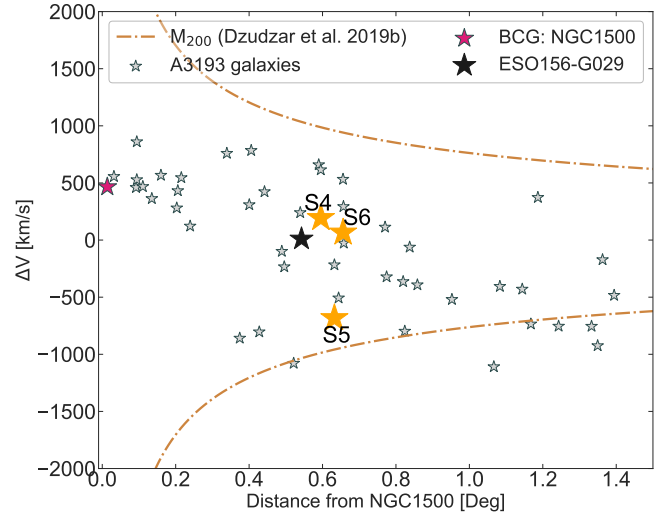


**Figure H1.** Projected angular separation of the galaxies within cluster A3193 versus recessional velocity difference between the cluster mean velocity and other galaxies. The caustics line show a potential of  $M = 2.7 \times 10^{14} M_{\odot}$  ([Džudžar et al. 2019b](#)). We highlight the position of S1, S4, S5 and S6 galaxies in J0400-52.

### H3 HIPASS J0400-52

Group HIPASS J0400-52 contains nine galaxies ([Sweet et al. 2013](#)) and it is embedded in a larger structure: it is at the virial radius of cluster Abell 3193. We detected the H I emission in only one galaxy (ESO156-G029). This galaxy was presented the detail in [Džudžar et al. \(2019b\)](#) as an example of galaxy being “pre-processed” - that is being shaped by the group environment as it falls into a cluster. In Section 3.1, we show that non-detected galaxies are typically dwarfs, particularly small compact dwarfs. However, there are three galaxies that are large enough, have a high stellar mass and large angular size, to be detected in this group: J0400-52:S4 [Scd], J0400-52:S5 [SB pec] and J0400-52:S6 [SB pec]. Our analysis show that these galaxies are H I deficient. The stellar masses of these galaxies are  $\sim 10^{11} M_{\odot}$ , and using  $M_R$  to  $M_{\text{HI}}$  scaling relation we were expecting  $M_{\text{HI}} \sim 10^{10.2} M_{\odot}$  ([Sweet et al. 2013](#); [Dénes et al. 2014](#)). The theoretical limit of our observations in this group is  $M_{\text{HI,lim}} = 10^{8.9} M_{\odot}$ , using this information we derive the lower limit of H I deficiency to be 1.3 dex. Such large deficiencies are typically found in a cluster environment e.g. [Chung et al. \(2009\)](#). The H I deficiency in these galaxies is due to either group pre-processing, or it is possible that they are the ‘backsplash’ galaxies i.e. already fell through the cluster potential well (e.g. [Yoon et al. 2017](#)). The backsplash scenario is most likely for S4 and S6, as the difference in their recessional velocity from the cluster mean velocity ( $\Delta V$ ) is around  $0 \text{ km s}^{-1}$  (see Figure H1).

### H4 HIPASS J1026-19

Group HIPASS J1026-19 contains six known member galaxies, three of which we detected in H I (S1, S2 and S5). The non-detected galaxies S3 and S4 are small dwarf galaxies, below our detection limit, while S6 is H I-deficient.

The largest member of J1026, S1, is connected to its smaller companion S2 (which is either a small edge-on disk or a

strongly barred-dwarf galaxy) by a tidal tail which is visible in optical, UV and H I imaging (see Figure H2). Tracing emission (optical and UV) from the S1 galaxy, we can see the faint stellar stream as a continuation of the spiral arm. This stellar stream broadens roughly at the midpoint between the S1 and S2 (looking at the projected distance between the S1 and S2) and the faint irregular structure resembles a tidal dwarf galaxy candidate. We examine the H I intensity map in the J1026-19 and see that low-density contours overlap S1 and S2 galaxies (see Figure I3). The H I contours in the north-west part of the J1026-19 group (S1 galaxy) are compressed with respect to those in the south-east. Moreover, the velocity map of the J1026-19 is being skewed towards the south-east at the roughly recessional velocity of the group. It is possible that a fly-by can explain such H I and stellar features (e.g. Kim et al. 2017). In a fly-by scenario, S2 galaxy passed near S1 galaxy (from the west to the east) which skew the gas in the direction of the motion of the S2 galaxy.

Examining the global environment we find that the J1026-19 is fairly isolated, having two nearest neighbouring galaxies at  $\sim 1.5$  Mpc in projected distance and velocity offset of  $\sim 250$  km s $^{-1}$ .

### H5 HIPASS J1051-17

Group HIPASS J1051-17 contains 20 known member galaxies, majority of them are small dwarf galaxies, within a velocity range between 5220 and 6243 km s $^{-1}$ . We detect six galaxies in H I emission within this group, which are potentially part of two sub-groups based on their recessional velocities. Out of six galaxies detected in H I emission, one is an H I-excess, polar ring galaxy J1051-17:S1 (see Figure 8), one has an average H I content four are H I-deficient galaxies which are a result of the environmental processing (see in depth analysis by Kilborn et al. in prep.).

### H6 HIPASS J1059-09

Group HIPASS J1059-09 contains 10 member galaxies, five of which we detected in H I. The non-detected galaxies S7, S8, S9, S10 are small dwarf galaxies, below our detection limit, while S4 is an SB0 type galaxy and based on its expected H I mass it is H I-deficient. We show our H I imaging of the entire group in Figure I5.

J1059-19 contains a strongly interacting galaxy pair S1 and S3 (MCG-01-28-013 and MCG-01-28-013, see Figure H3) which are connected by a tidal tail. The tidal tail between S1 and S3 galaxy is visible in multi-wavelength observations (optical, H $\alpha$ , UV, IR and H I). We note that the peak of H I emission is offset from the stellar centres of both galaxies, both in the direction of interaction. The H I peak of the H I emission that corresponds to the S3 galaxy is in the tidal tail between itself and S1 galaxy (see Figure H3). The obvious cause of the H I offsets is galaxy interaction, which is most likely triggering the star formation in the tidal tail region (e.g. Chromey et al. 1998).

Examining the global environment we find that the J1059-09 is possibly part of a larger structure, having a number of galaxies that are within a projected separation  $< 2$  Mpc and velocity offset of  $\sim 300$  km s $^{-1}$ . We also find another possible group to the east of J1059-09 at a velocity offset

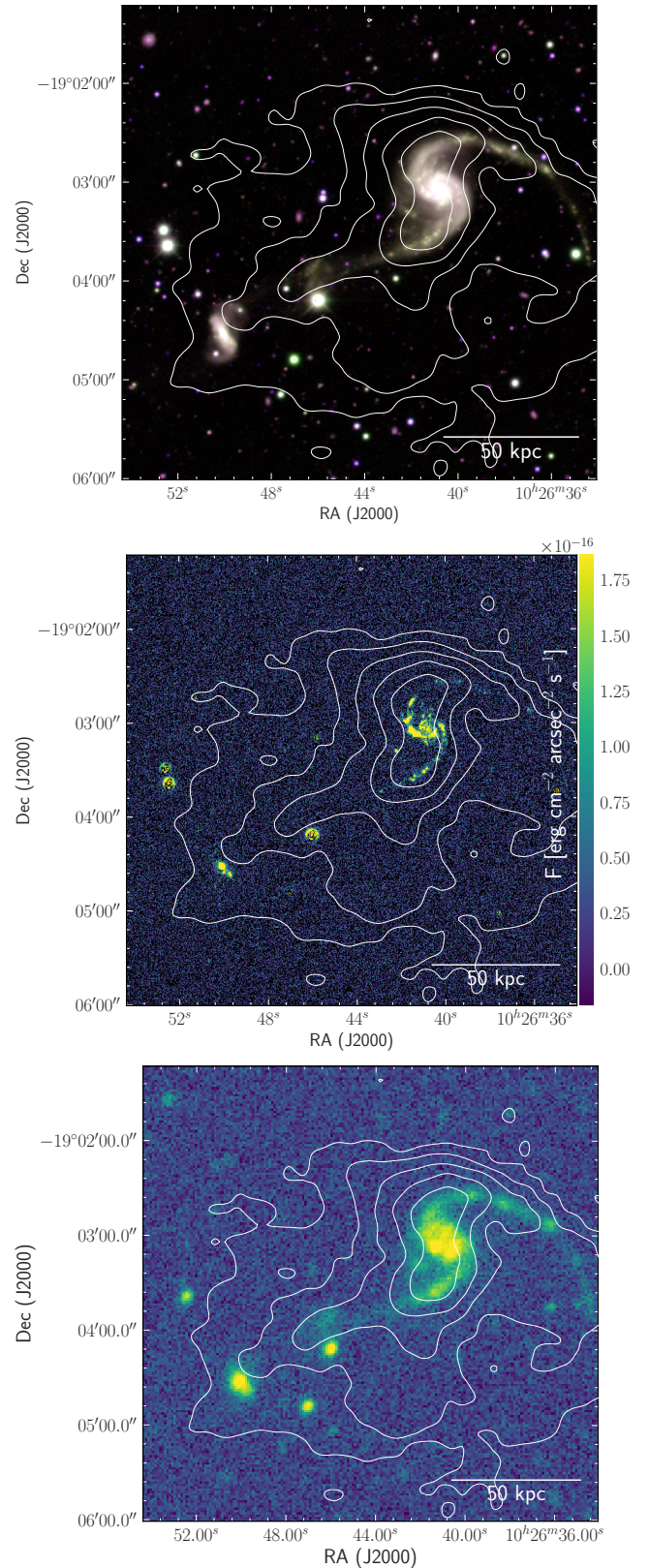


**Figure H2.** Multi-wavelength composites of the J1026-19 group. Panels with H I intensity distribution of J1026-19 overlaid on the multi-wavelength images. The H I column density contours: 5, 15, 30, 50 and  $70 \times 10^{19}$ . Upper: optical DECAM gri composition. Middle: H $\alpha$  imaging from SINGG narrow band image in the background, the colorbar shows surface brightness. Lower: GALEX near-uv image in the background.

from the J1059-09 of  $400\text{--}500\text{ km s}^{-1}$  and projected distance of  $\sim 3$  Mpc. J1059-09 is considered to be a group near of the intersection of the cosmic web filaments (see Section 4.2).

### H7 HIPASS J1159-19

The HIPASS J1159-19 group is a compact galaxy group with four known galaxy members (Sweet et al. 2013). Previous studies analysed resolved H I imaging of this system and found an interaction between NGC4027 (S1) and NGC4027A (S2) Phookun et al. (1992). Moreover, Phookun et al. (1992) found that NGC4027 has a ring of H I which is most likely thrown out from the NGC4027A galaxy in a flyby. With the SINGG survey two more dwarf galaxies were found in the projected proximity of S2 (Meurer et al. 2006). With our ATCA imaging we can not separate the H I from the individual galaxies (see Figure I6). However, we do find that the H I gas in NGC4027 has two components and we can see disturbed kinematics of this group. There is a large magnitude offset between the two brightest galaxies (in R-band:  $\sim 3.5$  mag), thus we classified this group as an optical fossil group.

Our analysis shows that group belongs to a larger structure as we find a large number of galaxies within projected separation of 0.5 Mpc around this group (see c and d panels in Figure I6). At the north-east from the J1159-19 there is Antennae group (Arp 244) and at the south-west there are several galaxies. We find that there are three HIPASS detection around J1159-19 group: Arp 244, HIPASS J1159-19a and HIPASS J1154-20.

### H8 HIPASS J1250-20

Group HIPASS J1250-20 has seven known members, five of these are spectroscopically confirmed, others are thought to be the group members, as stated in (Sweet et al. 2013; Džudžar et al. 2019a). We detect the H I emission which we associated with S1 and S2 galaxies. The non-detected galaxies are small compact dwarfs and we show that one galaxy, S4, is an H I deficient galaxy. The likely reason for H I-deficiency in S4 is the tidal interaction with S2, see Figure H4.

The two most luminous galaxies in J1250-20, S1 and S2 are interacting, see Figure H4. These galaxies have a comparable stellar masses however, they have vastly different H I mass. The H I contours that we associate with S2 galaxies overlap also on top of its smaller companion with which its interacting, S4. In this work we associate H I emission to S2, as S4 is physically smaller, has stellar mass  $\sim 0.9$  dex smaller, and has a lower specific star-formation.

The H I mass extracted from the region between the S1 and S2 galaxies is  $10^{8.9} M_{\odot}$ . This is a lower limit of the H I mass between galaxies as there is uncertainty where to place galaxy ‘borders’. The H I velocity of the extracted region corresponds to the recessional group velocity (in velocity space between S1 and S2), and in this region we do not detect faint stellar streams.

### H9 HIPASS J1408-21

Group HIPASS J1408-21 was reported to have six member galaxies (Sweet et al. 2013), with our ATCA imaging we detect two galaxies and find one new member, denoted as

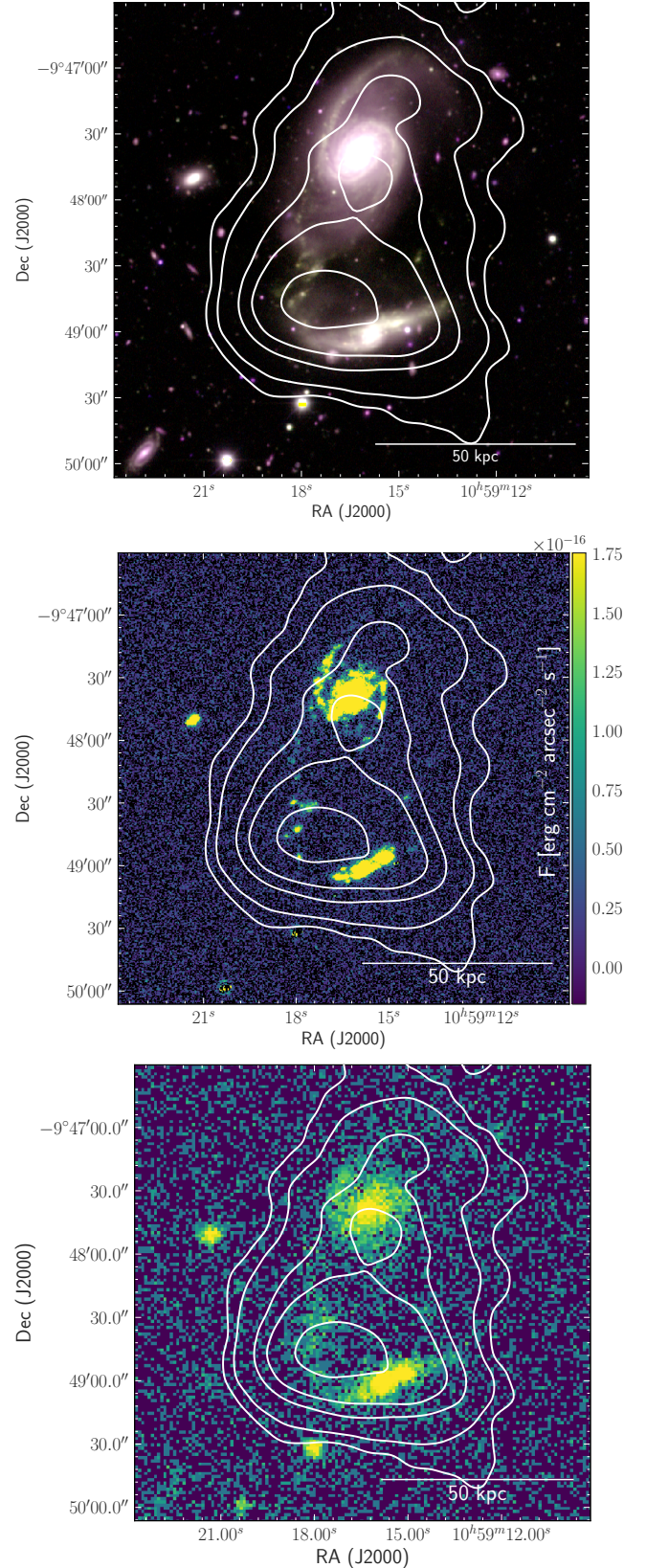


**Figure H3.** Multi-wavelength composites of the J1059-09 group. Panels with H I intensity distribution of J1059-09 overlaid on the multi-wavelength images. The H I column density contours: 12, 20, 40, 54 and  $78 \times 10^{19}$ . Upper: optical DECAM gri composition. Middle: H $\alpha$  imaging from SINGG narrow band image in the background, the colorbar shows surface brightness. Lower: GALEX near-uv image in the background.

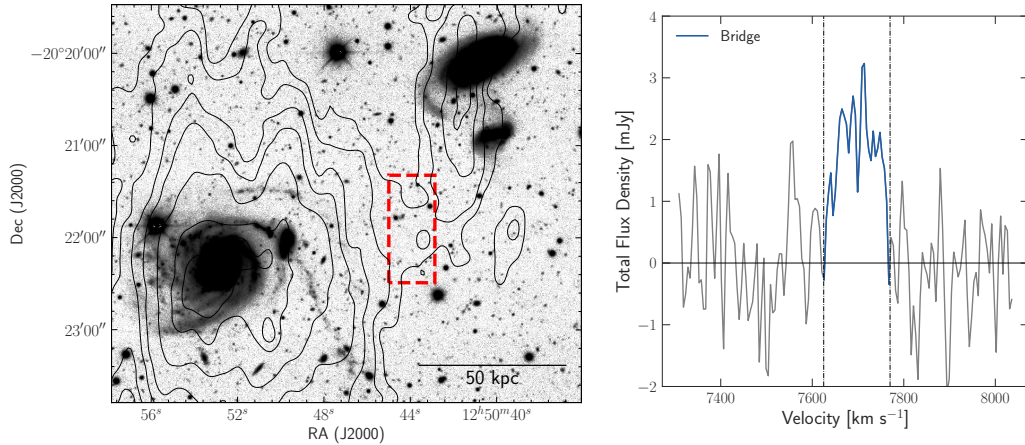


**Figure H4.** **Left:** Optical DECam  $g'$  band image overlaid with H I density contours and rectangle region showing the H I bridge between galaxies. The H I column density contours: 3.5, 7, 14, 20, 30, 40 and  $45 \times 10^{19}$ . **Right:** The H I spectrum extracted from the rectangular region on the right.

A1. The non-detected galaxies are two small compact dwarfs, which are below our detection limit, while two galaxies are (S2 and S4) are H I deficient.

Sweet et al. (2013) noted a possible tidal distortion of S1 galaxy towards S3 in  $H\alpha$ , and now with the H I imaging we can clearly see that they are interacting (see Figure I8). Examining the global environment we find that the J1408-21 near of the intersection of the cosmic web filaments (see Section 4.2).

#### H10 HIPASS J1956-50

Group HIPASS J1956-50 was reported to have four possible member galaxies (Sweet et al. 2013), however, the velocity of S3 galaxy is quite offset from the rest of the group members (Sweet et al. 2014) thus it is less likely to be a group member. We mapped the H I content with the ATCA and we detected three galaxies in H I, one of which is a new A1 group member, as previously was outside the angular SINGG field-of-view and thus was not detected (see Figure I9). One non-detected galaxy is a compact dwarf, and it is below our detection limit.

Examining the global environment we find that the J1956-50 is isolated (see panel c and d in Figure I9) and it is considered to be a group within a void (see Section 4.2). One neighbouring galaxy to J1956-50 is a faint compact dwarf galaxy south of S2 (Sweet et al. 2013) with  $\sim 1000 \text{ km s}^{-1}$  offset from the group velocity. Moreover, there are two galaxies with the velocity offset of  $\sim 500 \text{ km s}^{-1}$  albeit at  $\sim 2 \text{ Mpc}$  in projected distance from the group.

#### H11 HIPASS J2027-51

Group HIPASS J2027-51 has five known members, four of these were noted by Sweet et al. (2013) and one is a newly discovered member (Džudžar et al. 2019a). S1 and S2 are large spiral galaxies and we resolve the H I within them. S3 is a dwarf irregular galaxy and we only have a tentative H I detection, as it is below  $3\sigma$ . We do not detect H I in S4 which is a compact dwarf galaxy and it is below our detection limit. New detected galaxy is an irregular galaxy, marked A1 in Figure I10, and it is  $\sim 200 \text{ kpc}$  north from S4 galaxy.

**Table H1.** The phase classification based on the H I evolutionary scenario by Verdes-Montenegro et al. (2001).

ID (1)	Phase class (2)
J0205-55	Phase 1
J0209-10	Phase 2
J0258-74	Phase 1
J0400-52	Phase 1
J0443-05	...
J1026-19	Phase 2
J1051-17	Phase 1
J1059-09	Phase 2
J1159-19	Phase 2
J1250-20	Phase 2
J1403-06	...
J1408-21	Phase 1
J1956-50	Phase 1
J2027-51	Phase 1
2318-42a	Phase 2

(1) Group name:  
HIPASS+ID; (2) H I  
Phase classification.

Examining the global environment we note that J2027-51 belongs to a larger structure. We find several galaxies west from the S2 galaxy with the similar recessional velocity. ESO234-G024 located  $\sim 0.5 \text{ Mpc}$  west from S2, Mathewson et al. (1992) observed H I flux of  $9.42 \text{ Jy km s}^{-1}$ , which corresponds to  $M_{\text{H I}} = 10^{10.23} M_{\odot}$  adopting the group distance.

## APPENDIX I: INDIVIDUAL GROUPS

In Figures I1 to I10 we illustrate H I observations of the groups and their environment for which include the following:

a) The group H I intensity distribution (left) and the H I velocity field of the group (right). We specify in each figure description what is the lowest column density and the H I group velocity range. The detected galaxies in H I are marked with names that are used throughout this work.

**b)** In each sub-panel we show the H I spectra of the detected galaxies in the group. We show with the highlighted colour range where spectra was integrated to get the H I properties.

**c)** The position (Right Ascension and Declination) of the galaxies around each group. The colourbar shows the velocity difference of each galaxy from the group mean velocity. In Figure we also show the circles of the constant projected separation from the group centre, which are 0.5, 1 and 2 Mpc, if not otherwise specified in the Figure description.

**d)** The projected angular separation versus the velocity difference of each galaxy from the group mean velocity. The coloured points are showing galaxies above the adopted Ks magnitude limit of  $\sim 13.5$  mag, while the grey points show galaxies that are below the Ks magnitude limit. The grey lines show the simple caustics curves that are calculated with:  $v = \sqrt{\frac{GM_{200}}{2r}}$ , assuming that all galaxies are at the group distance.

\* Each Figure contains its own description with properties for the shown group.

\* Process of obtaining environment around Choirs is explained in Section 4.1.

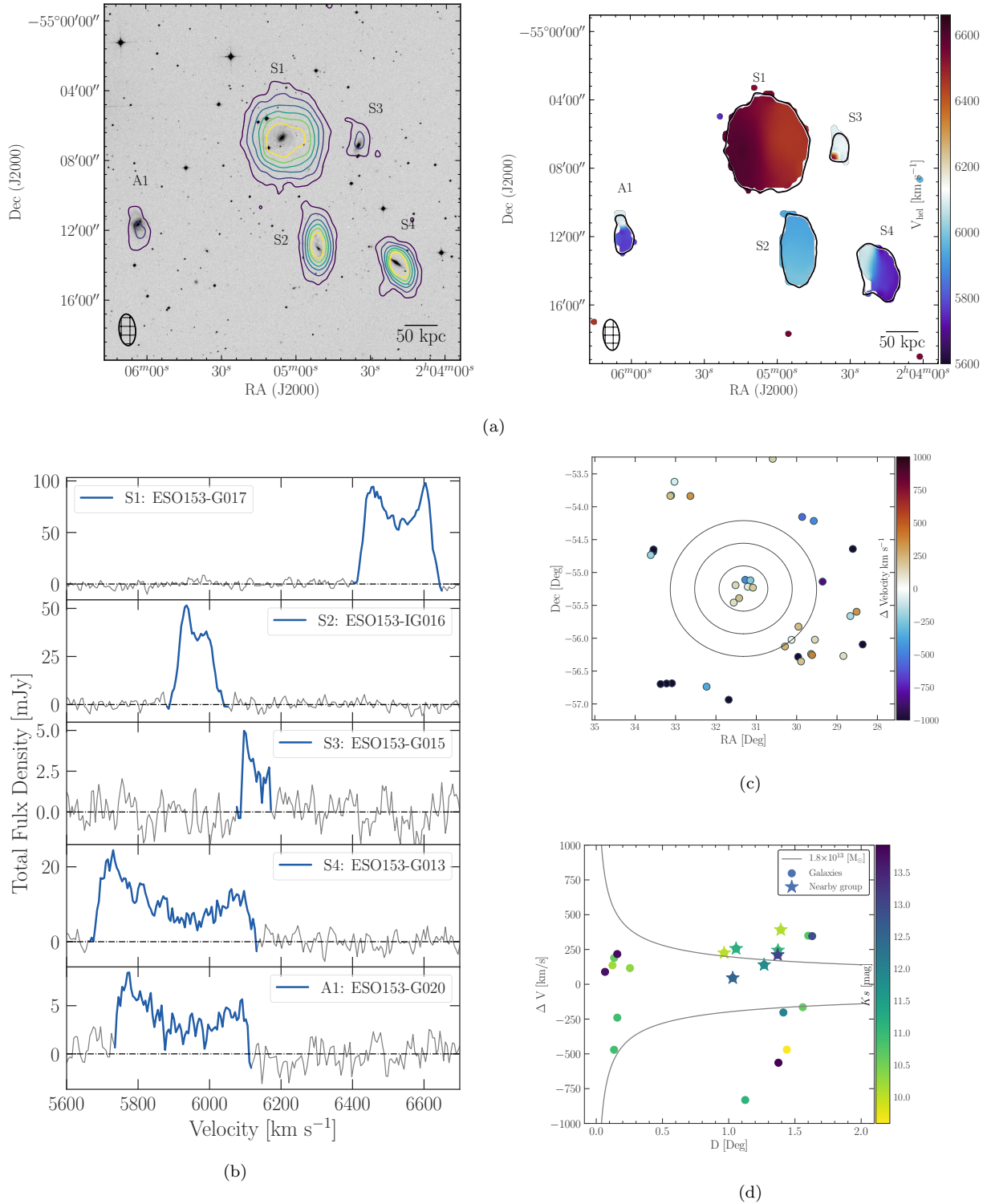


**Figure 11.** **a) Left:** The H I emission in the J0205-55 group. The H I emission is shown by the contours overlaid on the optical DSS2Red image. The lowest shown H I column density is a  $3\sigma$  detection over a velocity width of  $15 \text{ km s}^{-1}$  and corresponds to  $1.5 \times 10^{19} \text{ cm}^{-2}$ . The other H I column density contours are: 7, 14, 21, 28 and  $35 \times 10^{19} \text{ cm}^{-2}$ . **Right:** The velocity field of the J0205-55 group in the limit from 5600 to  $6660 \text{ km s}^{-1}$ . In the Figure map are marked group members as well as the lowest H I column density ( $2 \times 10^{19} \text{ cm}^{-2}$ ). The synthesized beam is shown in the bottom left corner, and the scale bar in the bottom right corner shows 50 kpc at the group distance. **b)** Panels of the H I spectra for each detected galaxy in the J0205-55 group. The enhanced colour shows where the spectrum was integrated. **c)** Environment around J0205-55, centred on the weighted mean of the group. The black circles are having radii of 0.5, 1, and 1.5 respectively. We show the velocity difference between weighted mean group velocity ( $6053 \text{ km s}^{-1}$ ) and the other nearby galaxies with magnitudes brighter than 13.5 mag, in the velocity range between  $4600$  and  $7600 \text{ km s}^{-1}$  and radius of  $100'$  from weighted mean of the group. **d)** Projected angular separation of the galaxies within J0205-55 region versus recessional velocity difference between weighted mean group velocity and other nearby galaxies. Galaxies associated with the group are within 0.5 deg, while galaxies associated with the south-west group (in panel c) are shown as stars. Grey solid curved line show simple caustics curves for a potential of  $M = 1.8 \times 10^{13}$ , assuming that all sources are at the J0205-55 distance of 93 Mpc. *MNRAS* **000**, 1–?? (2020)

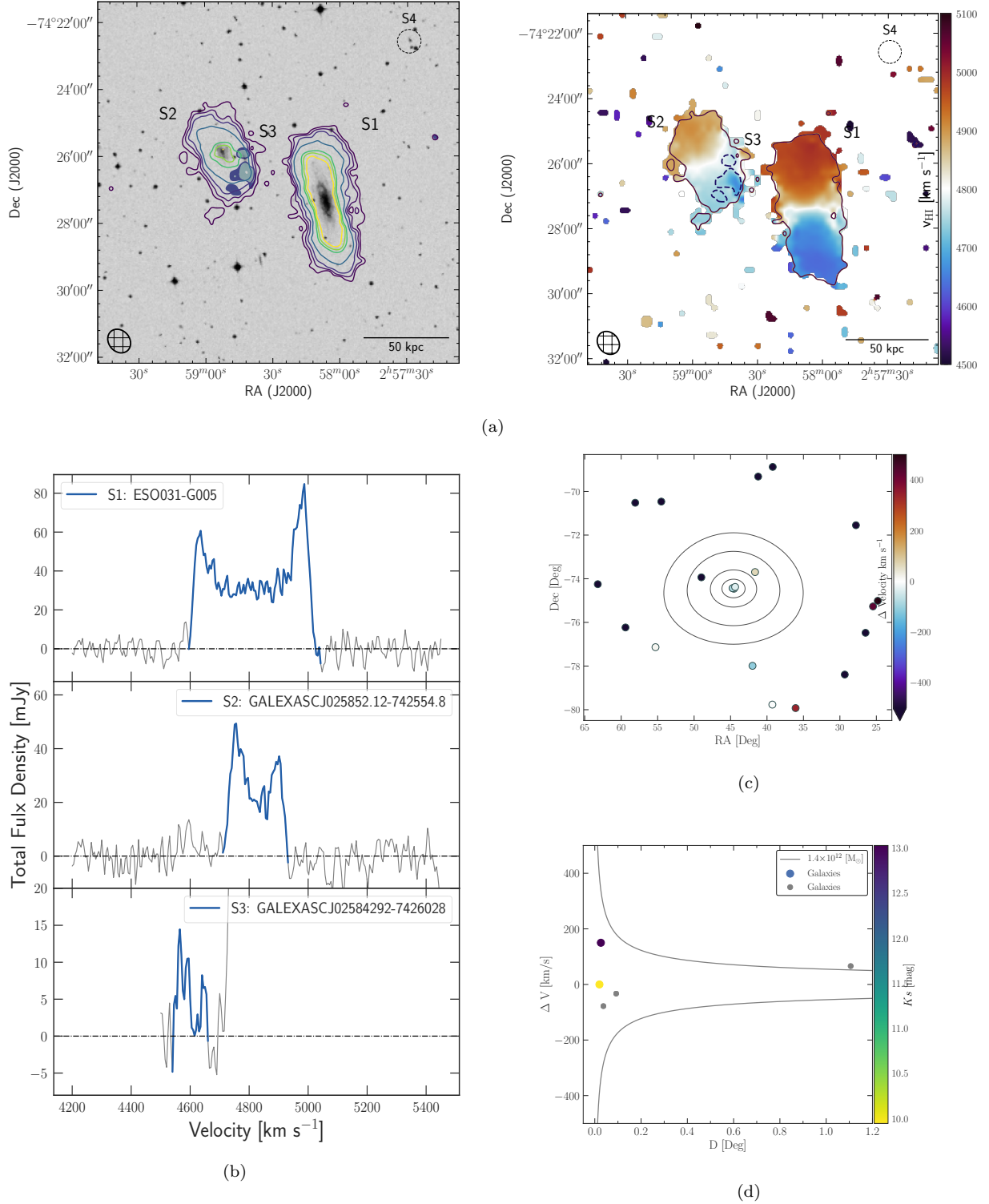


**Figure 12.** **a) Left:** The H I emission in the J0258-74 group. The H I emission is shown by the contours overlaid on the optical DSS B-band image. The lowest shown H I column density  $3 \times 10^{19} \text{ cm}^{-2}$ . The other H I column density contours are: 8, 16, 32 and 64, 75 and  $90 \times 10^{19} \text{ cm}^{-2}$ . The S3 galaxy is shown as shaded contours (between  $3$  and  $6 \times 10^{19} \text{ cm}^{-2}$ ) to enhance its visibility. The S4 galaxy is not detected in H I. **Right:** The velocity field of the J0258-74 group in the limit from 4500 to 5100 km s<sup>-1</sup>. The group members are marked (S1-S4) as well as the lowest H I column density ( $3 \times 10^{19} \text{ cm}^{-2}$ ). The dashed line shows the position of the S3 galaxy to enhance its visibility. The synthesized beam is shown in the bottom left corner, and the scale bar in the bottom right corner shows 50 kpc at the group distance. **b)** Panels of the H I spectra for each detected galaxy in the J0258-74 group. The enhanced colour shows where the spectrum was integrated. **c)** The global environment around J0258-74, centred on the weighted mean of the group (all four group galaxies are overlapping in the centre of the Figure). The black circles are denoting radii of 0.5, 1, 2 and 3 Mpc, respectively. We show the velocity difference between the S1 galaxy (HIPASS source) and the other nearby galaxies. **d)** Projected angular separation of the galaxies within J0258-74 region versus recessional velocity difference between S1 galaxy (HIPASS source) and other nearby galaxies. Galaxies associated with the group are within 0.2 deg. Grey solid curved lines show simple caustic curves for a potential of  $M = 1.4 \times 10^{12}$ , assuming that all sources are at the J0258-74 distance of 70 Mpc.

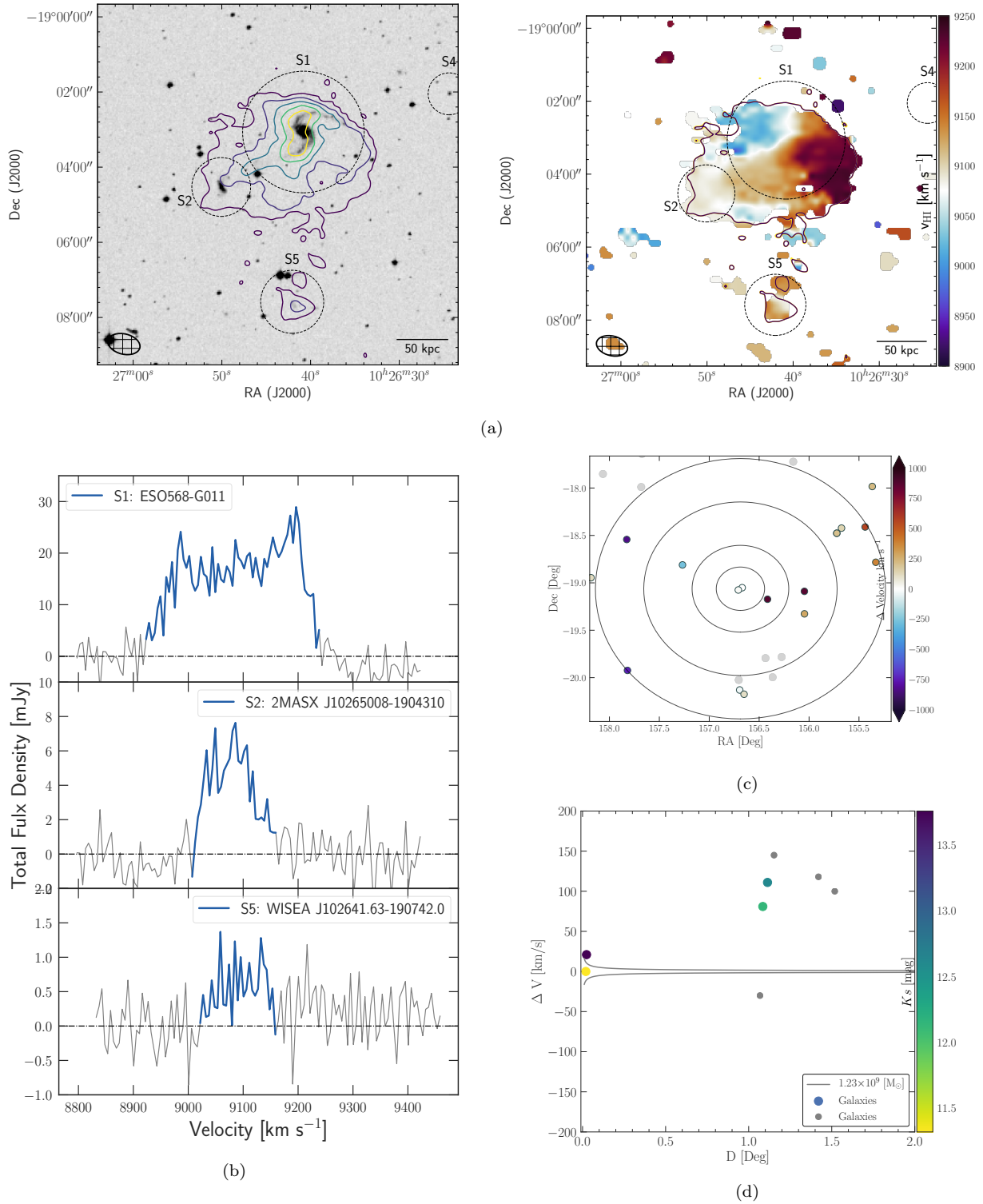


**Figure 13.** **a) Left:** The H I emission in the J1026-19 group, zoomed in into the central region. The H I emission is shown by the contours overlaid on the optical DSS B-band image. The lowest shown H I column density  $5 \times 10^{19} \text{ cm}^{-2}$ . The other H I column density contours are: 15, 30, 50, and  $70 \times 10^{19} \text{ cm}^{-2}$ . The S3, S4 and S6 galaxy are not detected in the H I. **Right:** The velocity field of the J1026-19 group in the limit from 8900 to 9250  $\text{km s}^{-1}$ . The group members that are within the field of view are marked (S1, S2, S4 and S5), and we show the lowest H I column density ( $5 \times 10^{19} \text{ cm}^{-2}$ ). The synthesized beam is shown in the bottom left corner, and the scale bar in the bottom right corner shows 50 kpc at the group distance. **b)** Panels of the H I spectra for each detected galaxy in the J1026-19 group. The enhanced colour shows where the spectrum was integrated. **c)** The global environment around J1026-19, centred on the weighted mean of the group. The black circles are denoting radii of 0.5, 1, 2 and 3 Mpc, respectively. We show the velocity difference between the S1 galaxy (HIPASS source) and the other nearby galaxies. **d)** Projected angular separation of the galaxies within J1026-19 region versus recessional velocity difference between S1 galaxy (HIPASS source) and other nearby galaxies. Galaxies associated with the group are within 0.1 deg. Grey solid curved lines show simple caustics curves for a potential of  $1.23 \times 10^9 M_{\odot}$ , assuming that all sources are at the J1026-19 distance of 135 Mpc.

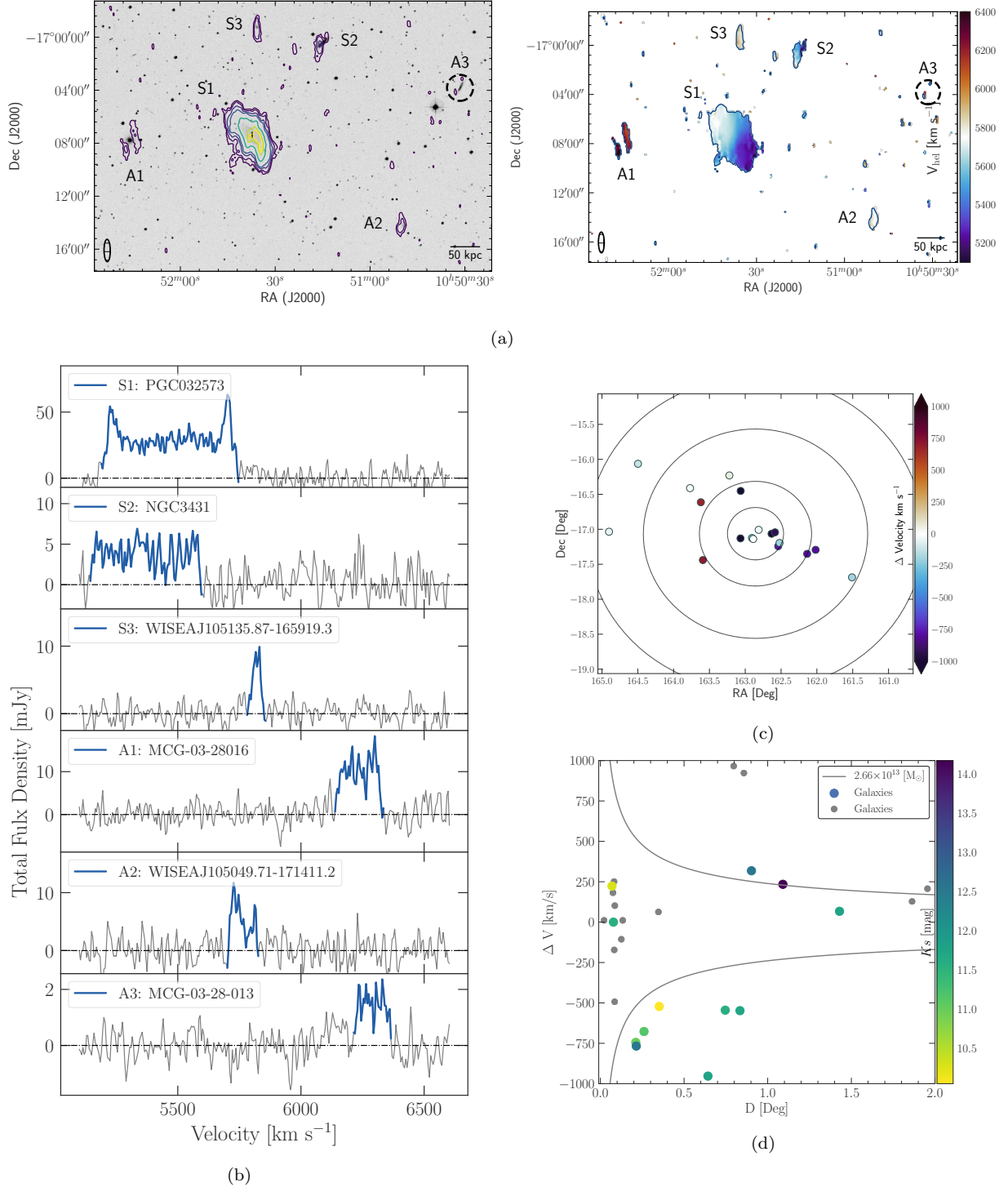


**Figure I4.** **a) Left:** The H I emission in the J1051-17 group. The H I emission is shown by the contours overlaid on the optical DSS B-band image. The lowest shown H I column density  $3 \times 10^{19} \text{ cm}^{-2}$ . The other H I column density contours are: 6, 12, 18, 36, 54, and  $60 \times 10^{19} \text{ cm}^{-2}$ . **Right:** The velocity field of the J1051-17 group in the limit from 5100 to 6400  $\text{km s}^{-1}$ . The group members that are detected in H I are marked (S1, S2, S3, A1, A2 and A3), and we show the lowest H I column density ( $3 \times 10^{19} \text{ cm}^{-2}$ ). The synthesized beam is shown in the bottom left corner, and the scale bar in the bottom right corner shows 50 kpc at the group distance. **b)** Panels of the H I spectra for each detected galaxy in the J1051-17 group. The enhanced colour shows where the spectrum was integrated. **c)** The global environment around J1051-17, centred on the weighted mean of the group. The black circles are denoting radii of 0.5, 1, 2 and 3 Mpc, respectively. We show the velocity difference between the S1 galaxy (HIPASS source) and the other nearby galaxies. **d)** Projected angular separation of the galaxies within J1051-17 region versus recessional velocity difference between S1 galaxy (HIPASS source) and other nearby galaxies. Galaxies associated with the group are within 0.2 deg. Grey solid curved lines show simple caustic curves for a potential of  $2.66 \times 10^{13} M_{\odot}$ , assuming that all sources are at the J1051-17 distance of 83 Mpc.

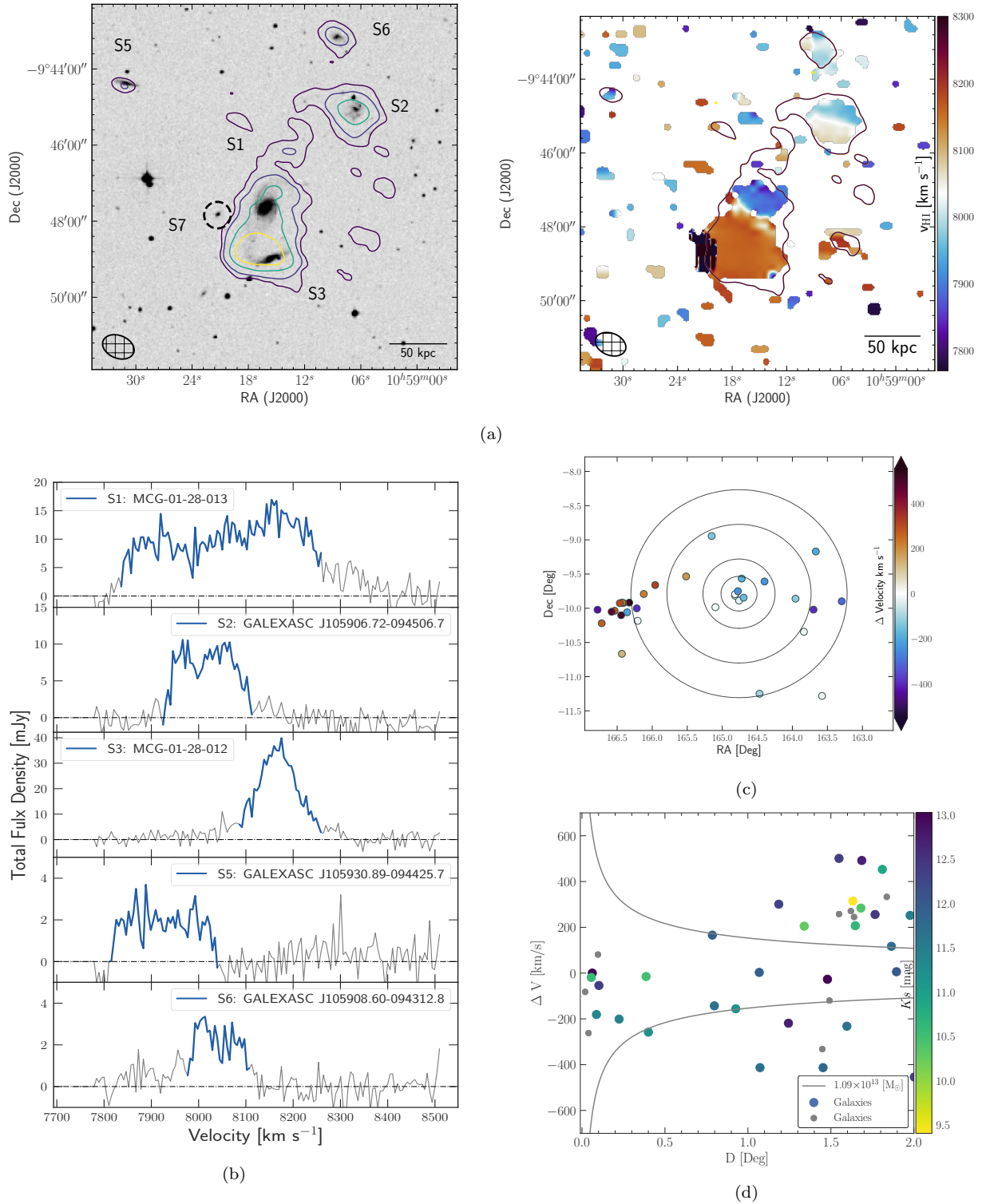


**Figure 15.** **a) Left:** The H I emission in the J1059-09 group, zoomed in into the central region. The H I emission is shown by the contours overlaid on the optical DSS B-band image. The lowest shown H I column density  $12 \times 10^{29} \text{ cm}^{-2}$ . The other H I column density contours are: 20, 40, and  $60 \times 10^{29} \text{ cm}^{-2}$ . **Right:** The velocity field of the J1059-09 group in the limit from 7770 to  $8300 \text{ km s}^{-1}$ . The group members are marked (S1-S4) as well as the lowest H I column density ( $12 \times 10^{29} \text{ cm}^{-2}$ ). The synthesized beam is shown in the bottom left corner, and the scale bar in the bottom right corner shows 50 kpc at the group distance. **b)** The H I spectrum of the J1059-09 group obtained with ATCA. The enhanced colour shows where the spectrum was integrated. **c)** The global environment around J1059-09, centred on the weighted mean of the group. The black circles are denoting radii of 0.5, 1, 2 and 3 Mpc, respectively. We show the velocity difference between the S1 galaxy (HIPASS source) and the other nearby galaxies. **d)** Projected angular separation of the galaxies within J1059-09 region versus recessional velocity difference between S1 galaxy (HIPASS source) and other nearby galaxies. Grey solid curved lines show simple caustics curves for a potential of  $1.09 \times 10^{13} M_{\odot}$ , assuming that all sources are at the J1059-09 distance of 122 Mpc.

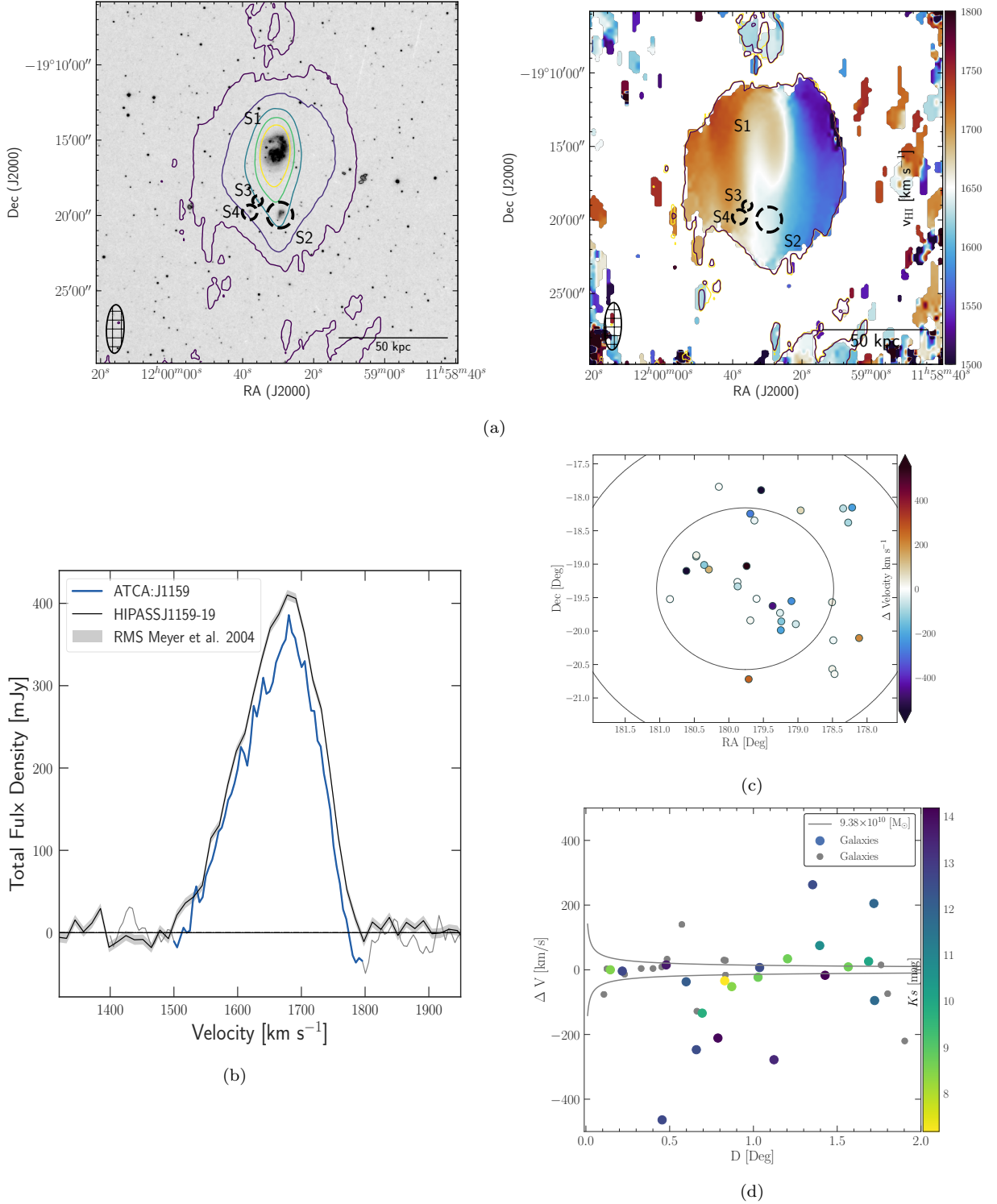


**Figure I6.** **a) Left:** The H I emission in the J1159-19 group. The H I emission is shown by the contours overlaid on the optical DSS B-band image. The lowest shown H I column density  $1 \times 10^{19} \text{ cm}^{-2}$ . The other H I column density contours are: 10, 30, 50, and  $70 \times 10^{19} \text{ cm}^{-2}$ . **Right:** The velocity field of the J1159-19 group in the limit from 1500 to 1800  $\text{km s}^{-1}$ . The group members are marked (S1-S4) as well as the lowest H I column density ( $1 \times 10^{19} \text{ cm}^{-2}$ ). The synthesized beam is shown in the bottom left corner, and the scale bar in the bottom right corner shows 50 kpc at the group distance. **b)** The H I spectrum of the J1159-19 group obtained with ATCA and HIPASS. The enhanced colour shows where the spectrum was integrated. **c)** The global environment around J1159-19, centred on the weighted mean of the group. The black circles are denoting radii of 0.5 and 1 Mpc, respectively. We show the velocity difference between the S1 galaxy (HIPASS source) and the other nearby galaxies. **d)** Projected angular separation of the galaxies within J1159-19 region versus recessional velocity difference between S1 galaxy (HIPASS source) and other nearby galaxies. Grey solid curved lines show simple caustics curves for a potential of  $M = 9.38 \times 10^{10}$ , assuming that all sources are at the J1159-19 distance of 25 Mpc.

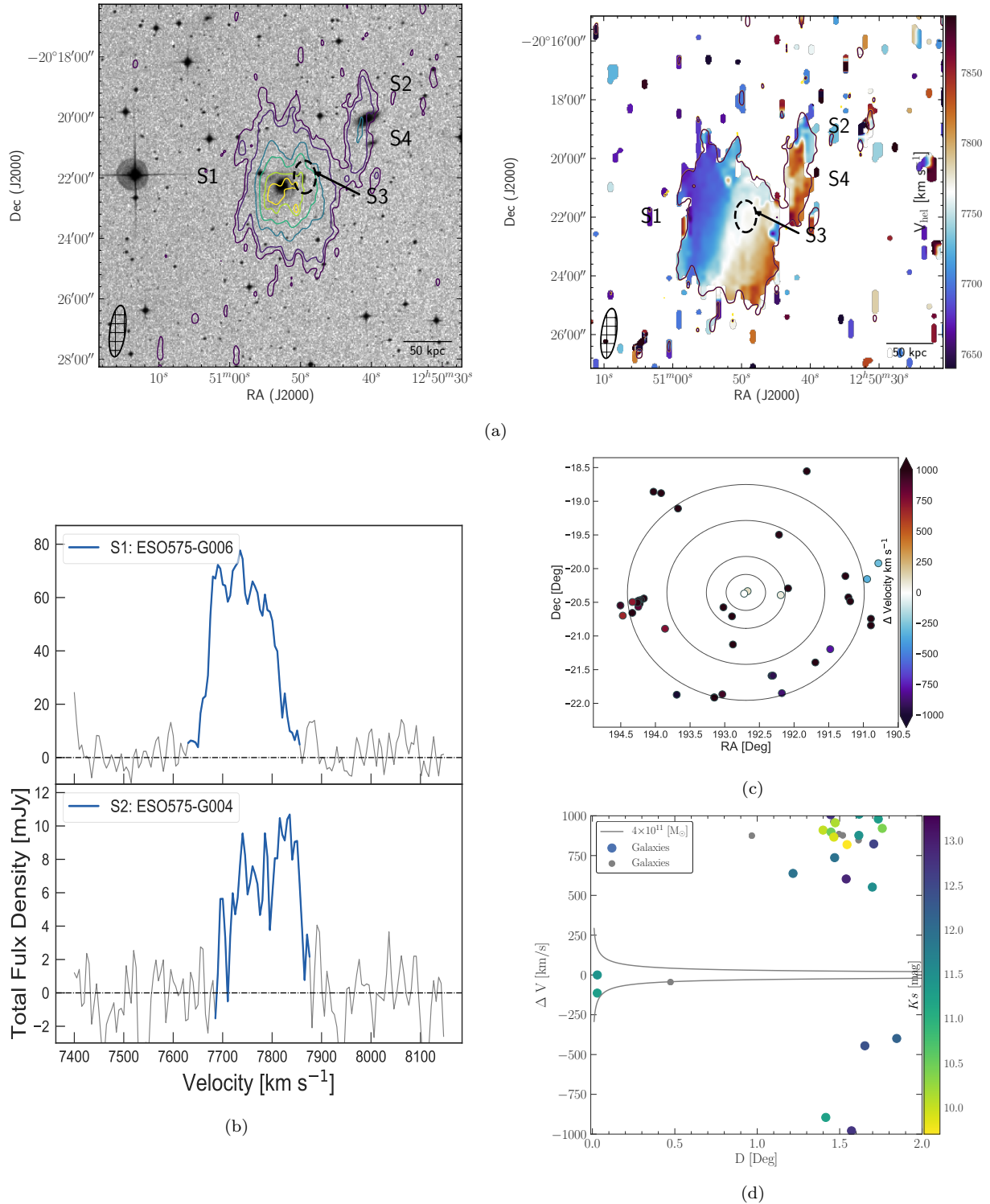


**Figure 17.** **a) Left:** The H I emission in the J1250-20 group. The H I emission is shown by the contours overlaid on the optical DSS-B band image. The lowest shown H I column density  $3.5 \times 10^{19} \text{ cm}^{-2}$ . The other H I column density contours are: 7, 20, 30, 40, and  $45 \times 10^{19} \text{ cm}^{-2}$ . **Right:** The velocity field of the J1250-20 group in the limit from 7640 to 7890  $\text{km s}^{-1}$ . The group members that are within the field of view and detected in H I are marked as S1, S2, S3 and S4, and we show the lowest H I column density ( $3.5 \times 10^{19} \text{ cm}^{-2}$ ). **b)** Panels of the H I spectra for each detected galaxy in the J1250-20 group. The enhanced colour shows where the spectrum was integrated. **c)** The global environment around J1250-20, centred on the weighted mean of the group. The black circles are denoting radii of 0.5, 1, 2 and 3 Mpc, respectively. We show the velocity difference between the S1 galaxy (HIPASS source) and the other nearby galaxies. **d)** Projected angular separation of the galaxies within J1250-20 region versus recessional velocity difference between S1 galaxy (HIPASS source) and other nearby galaxies. Grey solid curved lines show simple caustics curves for a potential of  $4 \times 10^{11} M_{\odot}$ , assuming that all sources are at the J1250-20 distance of 114 Mpc.

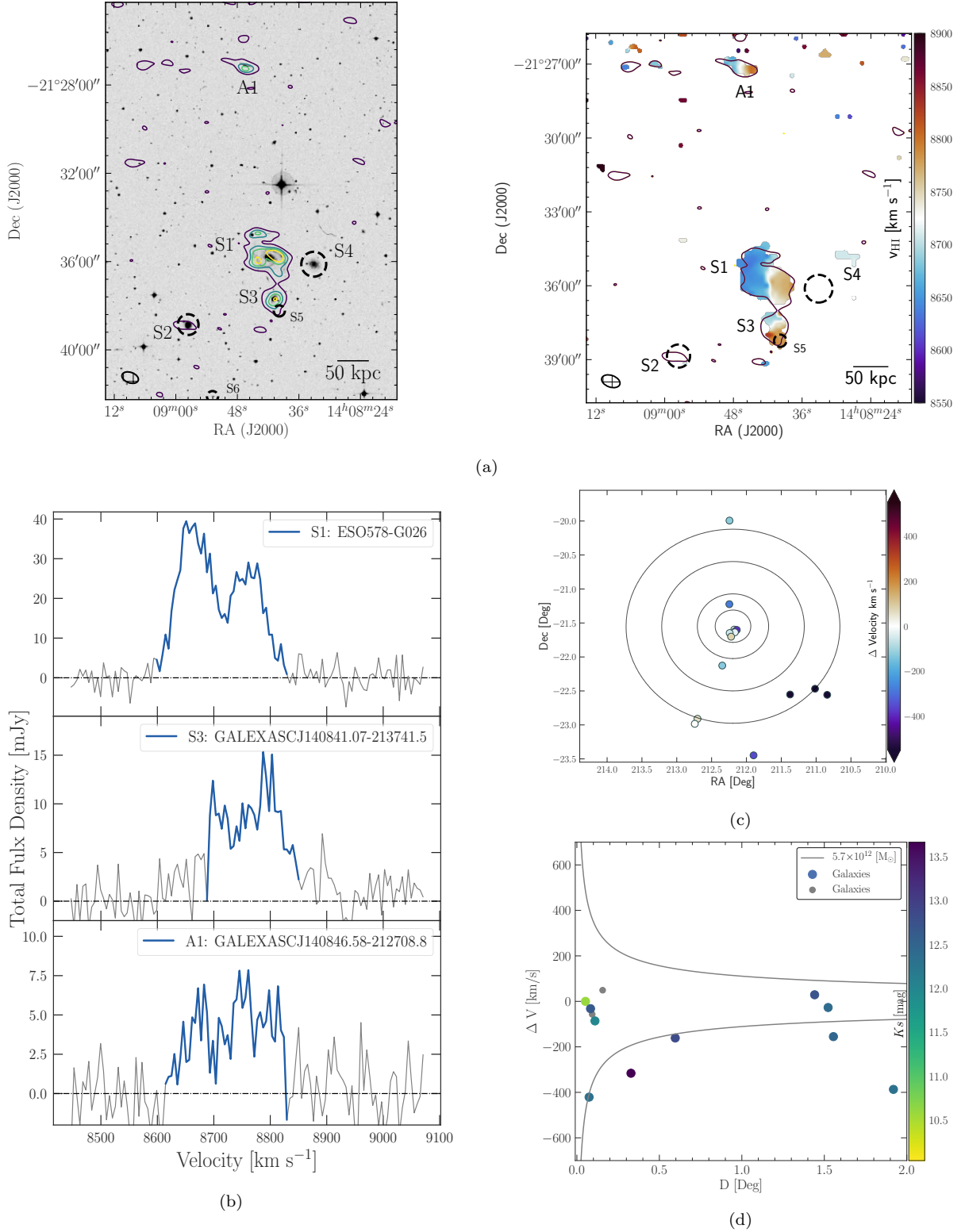


**Figure 18.** **a) Left:** The H I emission in the J408-21 group. The H I emission is shown by the contours overlaid on the optical DSS image. The lowest shown H I column density  $24 \times 10^{19} \text{ cm}^{-2}$ . The other H I column density contours are: 40, 50, and  $60 \times 10^{19} \text{ cm}^{-2}$ . **Right:** The velocity field of the J408-21 group in the limit from 8550 to  $8900 \text{ km s}^{-1}$ . The group members that are within the field of view and detected in H I are marked as S1, S3 and A1, and we show the lowest H I column density ( $24 \times 10^{19} \text{ cm}^{-2}$ ). **b)** Panels of the H I spectra for each detected galaxy in the J1408-21 group. The enhanced colour shows where the spectrum was integrated. **c)** The global environment around J1408-21, centred on the weighted mean of the group. The black circles are denoting radii of 0.5, 1, 2 and 3 Mpc, respectively. We show the velocity difference between the S1 galaxy (HIPASS source) and the other nearby galaxies. **d)** Projected angular separation of the galaxies within J1408-21 region versus recessional velocity difference between S1 galaxy (HIPASS source) and other nearby galaxies. Grey solid curved lines show simple caustic curves for a potential of  $5.7 \times 10^{12} M_{\odot}$ , assuming that all sources are at the J1408-21 distance of 128 Mpc.

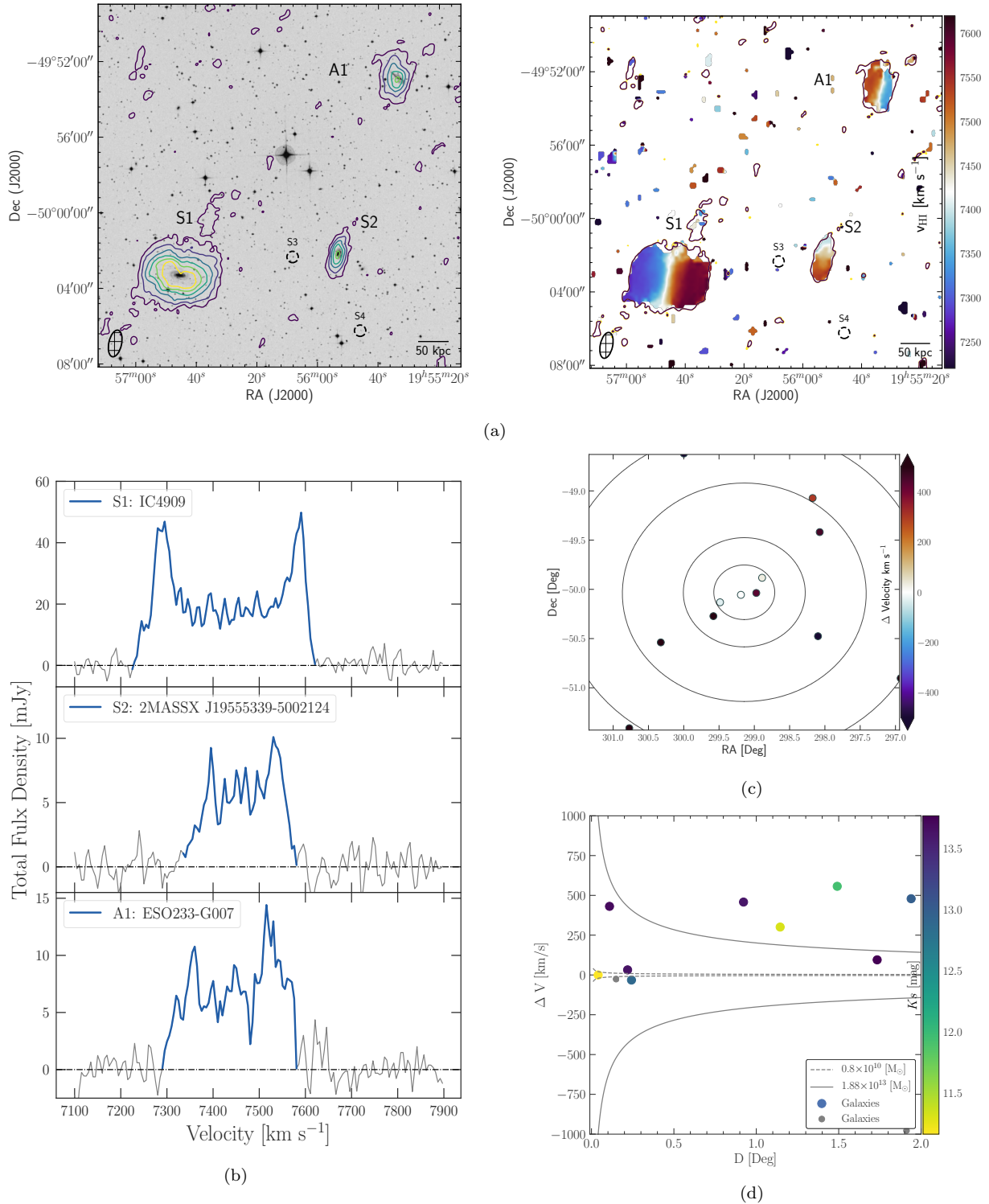


**Figure 19.** **a) Left:** The H I emission in the J1956-50 group. The H I emission is shown by the contours overlaid on the optical DSS image. The lowest shown H I column density  $1.8 \times 10^{19} \text{ cm}^{-2}$ . The other H I column density contours are: 7, 14, 21, 28 and  $35 \times 10^{19} \text{ cm}^{-2}$ . **Right:** The velocity field of the J1956-50 group in the limit from 7220 to 7620  $\text{km s}^{-1}$ . The group members that are within the field of view and detected in H I are marked as S1, S2 and A1, and we show the lowest H I column density ( $1.8 \times 10^{19} \text{ cm}^{-2}$ ). The synthesized beam is shown in the bottom left corner, and the scale bar in the bottom right corner shows 50 kpc at the group distance. **b)** Panels of the H I spectra for each detected galaxy in the J1956-50 group. The enhanced colour shows where the spectrum was integrated. **c)** The global environment around J1956-50, centred on the weighted mean of the group. The black circles are denoting radii of 0.5, 1, 2 and 3 Mpc, respectively. We show the velocity difference between the S1 galaxy (HIPASS source) and the other nearby galaxies. **d)** Projected angular separation of the galaxies around J1956-50 region versus the recessional velocity difference between S1 galaxy (HIPASS source) and other nearby galaxies. Grey solid (including galaxy at  $\Delta v \sim 500 \text{ km s}^{-1}$ ) and dashed (excluding galaxy at  $\Delta v \sim 500 \text{ km s}^{-1}$ ) curved lines show simple caustic curves for a potential of  $M = 1.89 \times 10^{13}$  and  $0.8 \times 10^{10} M_{\odot}$  respectively, assuming that all sources are at the J1956-50 distance of 110 Mpc.

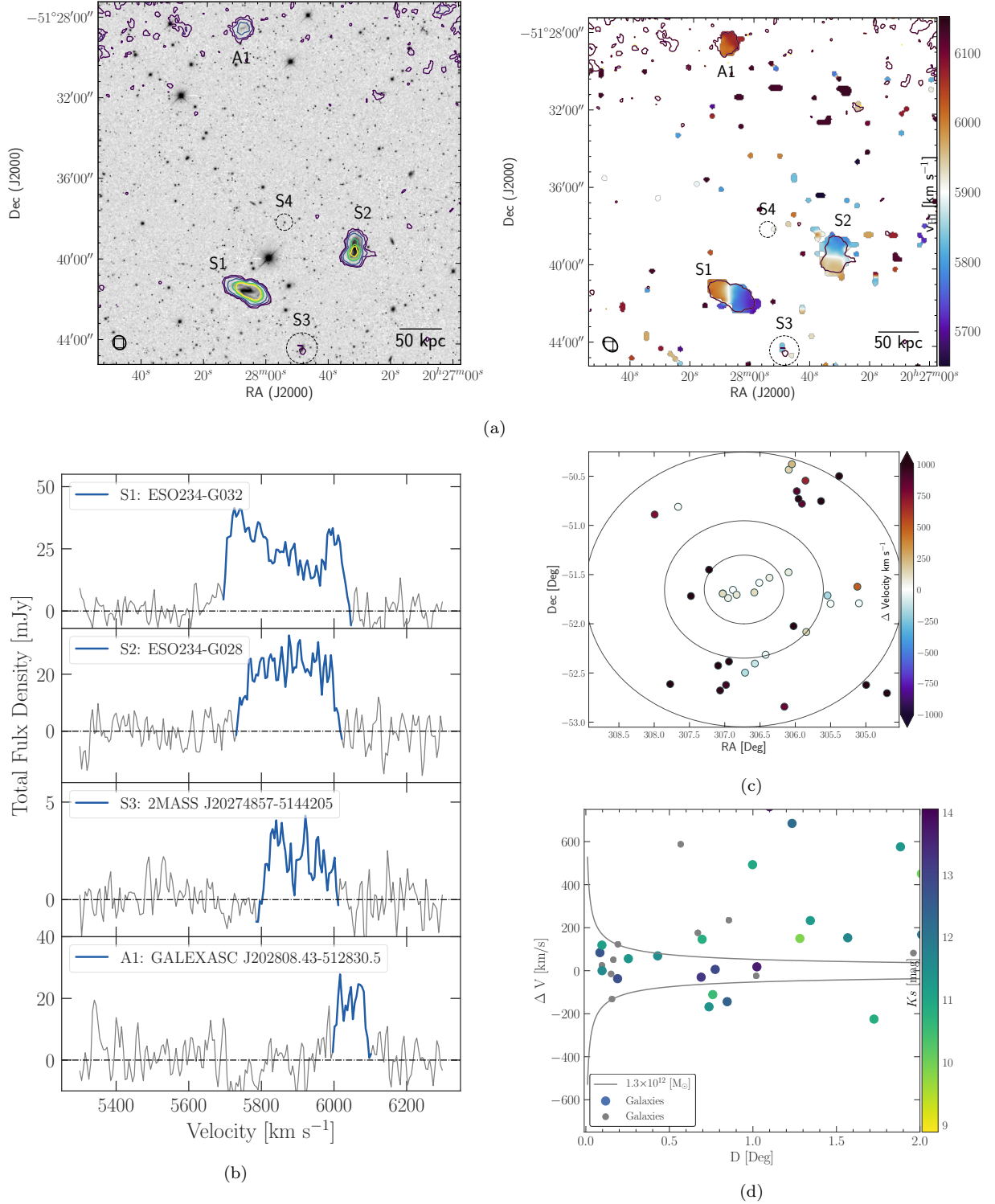


**Figure 10.** **a) Left:** The H I emission in the J2027-51 group, zoomed in into the central region. The H I emission is shown by the contours overlaid on the optical DECAM  $r$ -band image. The lowest shown H I column density  $8 \times 10^{19} \text{ cm}^{-2}$ . The other H I column density contours are: 16, 32, 64, 75 and  $90 \times 10^{19} \text{ cm}^{-2}$ . The S3 galaxy has a weak possible detection (see S3 spectrum in panel b), while the S4 galaxy is not detected in H I. At the North we detected new galaxy, labelled A1. **Right:** The velocity field of the J2027-51 group in the limit from 5650 to 6150  $\text{km s}^{-1}$ . The group members that are within the field of view are marked (S1, S2, S4 and A1), and we show the lowest H I column density ( $8 \times 10^{19} \text{ cm}^{-2}$ ). The synthesized beam is shown in the bottom left corner, and the scale bar in the bottom right corner shows 50 kpc at the group distance. **b)** Panels of the H I spectra for each detected galaxy in the J2027-51 group. The enhanced colour shows where the spectrum was integrated. **c)** The global environment around J2027-51, centred on the weighted mean of the group. The black circles are denoting radii of 0.5, 1, and 2 Mpc, respectively. We show the velocity difference between the S1 galaxy (HIPASS source) and the other nearby galaxies. **d)** Projected angular separation of the galaxies within J2027-51 region versus recessional velocity difference between S1 galaxy (HIPASS source) and other nearby galaxies. Grey solid curved lines show simple caustic curves for a potential of  $1.3 \times 10^{12} M_{\odot}$ , assuming that all sources are at the J2027 distance of 87 Mpc.